THE PENNSYLVANIA STATE UNIVERSITY

TURBULENT BOUNDARY-LAYER CHARACTERISTICS ON A ROTATING HELICAL BLADE

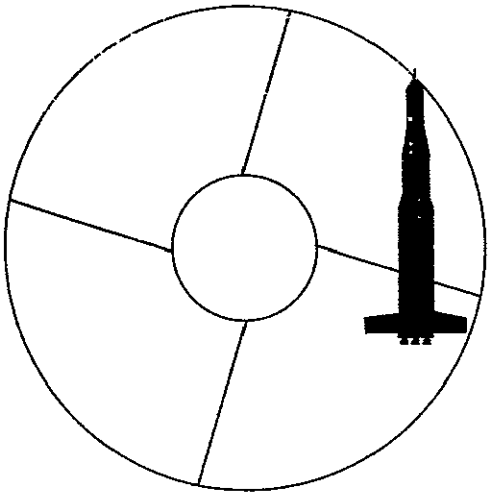

by

Ahmad Jabbari

N69-36288
(ACCESSION NUMBER)
(THRU)
109
(PAGES)
1
(CODE)
CR 105649
(NASA CR OR TMX OR AD NUMBER)
12
(CATEGORY)
FACILITY FORM 602

DEPARTMENT OF AEROSPACE ENGINEERING

UNIVERSITY PARK, PENNSYLVANIA

September 1969

Reproduced by the CLEARINGHOUSE for Federal Scientific & Technical Information Springfield Va. 22151

The Pennsylvania State University

The Graduate School

Department of Aerospace Engineering

TURBULENT BOUNDARY-LAYER CHARACTERISTICS ON A ROTATING HELICAL BLADE

A thesis in

Aerospace Engineering

by

Ahmad Jabbari

Submitted in partial fulfillment
of the requirements
for the degree of

Master of Science

September 1969

Approved:

_____

_____

Assistant Professor of Aerospace Engineering, Thesis Advisor

_____

_____

Head of the Department of Aerospace Engineering

ACKNOWLEDGMENTS

The author wishes to acknowledge the guidance of his advisor, Dr. B. Lakshminarayana without whose advice this thesis would not have been possible.

The author also wishes to express his gratitude to Mr. Hideki Yamaoka for measuring the wall shear stress on the blade surface.

The research contained in this thesis was performed under the sponsorship of National Aeronautics and Space Administration, and was conducted at the Department of Aerospace Engineering of the Pennsylvania State University and is currently operating under contract No. NGL 39-009-007.

TABLE OF CONTENTS

Page

LIST OF FIGURES

LIST OF TABLES

NOMENCLATURE

A	parameter related to the main flow turning angle
c	curvature of the X-axis in the curvilinear coordinate system
C_f	skin friction coefficient
F, f	functional relations
G, g	universal functions of $\eta = y/\delta$
h	distance measured from the wall to a point outside the boundary-layer
H	shape factor
P_o	total pressure
P_s	static pressure
Q, q	dynamic head
R'	perpendicular distance of the particle from the axis of rotation in curvilinear coordinate system
r	local radius
$R = r/r_t$	non-dimensionalized radius
r, θ, y	rotating cylindrical coordinate system
T	temperature
u, v, w	velocities in (θ, y, r) directions
u', w'	fluctuating velocities in θ and r directions
u^*	frictional velocity
X, Y, Z	curvilinear coordinate system
$y^+ = \frac{yu^*}{\nu}$	non-dimensionalized distance
R_r, R_δ, $R_\delta{}^*$	Reynolds number based on r, δ and δ^*
$\alpha = \tan^{-1}\varepsilon_o$	limiting wall streamline angle
$\alpha_L = \tan^{-1}\varepsilon$	local flow angle

δ	boundary-layer thickness
δ^*	momentum thickness
δ_1	displacement thickness
$\eta = y/\delta$	non-dimensionalized parameter
θ	distance in tangential direction
ν	kinematic viscosity
ρ	density
τ_o	wall skin friction
$\tau_{o,u}$, $\tau_{o,w}$	components of τ_o in θ, r directions
Ω	angular velocity
Ω_X, Ω_Y, Ω_Z	angular velocity in (X, Y, Z) directions
ψ_s	non-dimensionalized pressure coefficient

Subscript

t	refers to values at the tip
L	local
s	static
1	refers to the components of the velocity in the curvilinear coordinate system in Equations (11) through (14)

1. INTRODUCTION

1.1 Origin of the Study

The use of multibladed inducers in liquid rocket feed systems is of great practical importance. These devices are used for various purposes such as to handle cavitating flow in pumps, to increase the suction specific speed of the centrifugal impellers, and to regulate the flow before it enters the impeller.

The inducer blades are usually designed in the form of helical surfaces as shown in Fig. (1).

Rocket pump inducers operate at high rotational speeds. At such speeds the Reynolds number of the flow is high enough to produce a turbulent boundary-layer on the blades. Because of the existence of a centrifugal force, the fluid particles near the blade surface are thrown out in a radial direction giving rise to a component of the flow velocity in that direction, which imposes a severe restriction on the performance characteristics of the inducers. Thus it becomes necessary to investigate the three-dimensional boundary-layer characteristics on these blades in order to understand flow behavior within the narrow passages of the inducer blades. Since great difficulties are associated with such an investigation it is proposed to carry out a study of a simplified model, namely a single helical blade of large chord length enclosed in an annulus. The influence of pressure and velocity changes that would normally exist in the inviscid stream of an axial inducer passage is neglected. However, it is hoped that this attempt will be useful in a series of systematic studies toward a better understanding

of the three-dimensional boundary-layers in general and the flow through narrow inducer passages in particular.

1.2 Statement of the Problem

The boundary layer which develops within various parts of a rotating machinery, for example, turbomachinery blades, propellers, rocket inducer blades, and helicopter blades, is not two-dimensional. Because of the rotation of the system two additional forces are introduced. These are centrifugal and Coriolis forces, which in addition to viscous and pressure forces make the direction of the flow within the boundary-layer different from the flow outside, thus forming a three-dimensional flow configuration.

The velocity vector in such a boundary-layer when it is traversed normal to the surface appears to be skewed. Along the normal, the cross-flow velocity component varies in magnitude from zero at the surface to some maximum and then to zero at the edge of the boundary-layer. The reason for the existence of the cross-flow can be found in various publications. In the case of a stationary configuration such as a curved duct, the particles near the flow axis which have a higher velocity are acted upon by a larger centrifugal force than the slower particles near the wall. As a result there will be cross flow inside the boundary-layer.

Boundary-layers of the type described above where the three-dimensional perturbations in the layer are caused by the transverse pressure gradient are commonly referred to as "secondary-flows".

In the case of turbomachinery blades fluid particles adjacent to the blades are carried by them through friction and are thrown outwards due

to centrifugal force, thus giving rise to a cross-flow velocity component. In what follows this cross-flow component is referred to as the radial velocity.

1.3 Methods and Means of the Investigation

The complexity of turbulent flows does not allow us, for the time being, to carry out an exact analysis of this flow using Reynolds' equations. Instead, approximate solutions may be obtained using momentum integral equations and empirical knowledge of the flow. This technique consists of assuming suitable velocity profiles and an empirical relation for shear stress variations so that the momentum integral equations may be solved. The validity of these assumptions are then checked by experiment.

The purpose of the present investigation is to study both analytically and experimentally the turbulent boundary-layer characteristics on a rotating helical blade of small aspect ratio enclosed in an annulus as shown in Fig. (5-a). The investigation includes the measurement of main stream and radial velocity profile, boundary-layer growth and skin friction.

2. THEORETICAL CONSIDERATIONS

2.1 Brief Account of the Related Works

A survey of the existing literature on the subject of three-dimensional turbulent boundary-layer showed that very little theoretical and/or experimental works are available; even these depend largely upon two dimensional considerations. Moreover, momentum integral equations have been used along with assumed velocity profiles and the empirical knowledge of the skin friction to obtain approximate solutions.

The first general model is suggested by Prandtl [3] and has the following form:

$$u/U = G \tag{1}$$

$$w/U = \varepsilon_o \, g \, G \tag{2}$$

where $\varepsilon_o = \tan \alpha$. Here, G and g are universal functions of $\eta = y/\delta$, u and w are velocities in streamwise and cross-flow directions and δ, the boundary-layer thickness. The angle α is commonly referred to as the "limiting streamline angle", which is the angle that the limiting position of a streamline makes relative to the direction of the flow outside as the blade surface is approached. The boundary conditions are:

$$y = \delta, \; G = 1, \; g = 0$$

$$y = 0, \; G = 0, \; g = 1$$

If this model is valid the product of Gg should be a universal function of η.

Prandtl's flow model has been applied to various three-dimensional turbulent boundary-layers with specific powers of g and G. Mager [1] using some of the Grushwitz's [8] data for a flow through a curved duct

concludes that gG is in fact a universal function of η. Specific powers of g and G used by Mager are

$$G = (\eta)^{1/n} . \tag{3}$$

$$g = (1 - \eta)^2 \tag{4}$$

Even though these correlations agree with Grushwitz's data for $\eta = 7$, it is not known whether similar unique coupling of the velocity profiles exists for all three-dimensional layers.

Johnston [9] using some of his own three-dimensional boundary-layer data generated by secondary flow found that such a flow model resulted in a typical spread,meaning that Gg is not a universal function. Johnston's experiment was performed over the flat wall bounding a two dimensional air jet forced to flow against a perpendicular backwall. Therefore,a second model is proposed by Johnston. It is argued that the usual representation of the velocity profiles as a function of the distance from the surface does not lead into a satisfactory solution as compared with w as a function of u and a parameter A. This model has the general form of

$$w/U = w/U \ (\varepsilon_o, A, u/U) \tag{5}$$

The parameter A is related to the main flow turning angle. Equation (5) shows that the y dependency of w has been discarded. However, the y dependency of u still remains to allow for a complete profile change in the boundary-layer. A polar plot of Johnston's profile is shown in Fig. (2-a). At a given position normal to the wall, the locus of the tip of the velocity vector projected on a plane parallel to the wall and corresponding to the outer 90% of the layer is a straight line.

$u/U = 1$ corresponds to the main flow whereas $u/U = 0$ is the point at the surface. Two regions are defined. In the region near the wall

$$w/U = \varepsilon_o \, u/U \tag{6}$$

and in the region near the main flow

$$w/U = A \, (1 - u/U) \tag{7}$$

A more detailed experimental investigation of this phenomenon is carried out by Perry and Joubert [13]. It is found that the triangular model of Johnston is indeed valid for their experiment. Francis and Pierce [15] on the other hand, have carried out another experimental investigation of skewed turbulent boundary-layers in low speed flows and have reported that the triangular model is not universal since their data shows various degrees of rounding off at the apex of the triangle. Also the slope of profiles in the region II is not always approximated as constant. In a similar experiment on a rotating free disk, Stain [10] reports that the universal description of two-dimensional turbulent boundary-layer flow by Cornish [18] can be extended to the tangential component of the three-dimensional layer. However, a new wake function is developed and combined with Cornish's wall function to give a description of the cross-flow profile.

Analysis carried out by von Karman [12] for a free rotating disk using Prandtl's model assumes that

$$u/U = \eta^{1/7} \tag{8}$$

$$w/U = \varepsilon_o \, \eta^{1/7} \, [1-\eta] \tag{9}$$

The expression used for shear stress is

$$\tau_o = 0.0225 \, \rho U^2 \, \left(\frac{U\delta}{\nu}\right)^{-1/4} \tag{10}$$

where τ_o is the value of the skin friction at the wall. In this case ε_o is the tangent of the angle that τ_o make with the tangential direction.

Goldstein [16] assumes a logarithmic law for the shearing stress at the wall and expresses the radial velocity profiles in two parts.

Experiment carried out by Gregory, Stuart, and Walker [14] for the free disk shows that von Karman's profile gives better agreement at the maximum value of radial velocity than Goldstein's logarithmic profile. On the other hand, away from the wall the latter gives a closer fit with the experimental results. Thus, generally speaking, neither of the profiles matches the data throughout the boundary-layer.

Another theoretical investigation by Banks and Gadd [7] on boundary-layers over a free rotating disk indicates that the value of the power of $g = (1 - \eta)$ lies somewhere between 1 and 2. Cham and Head [11] report that their measured tangential velocity profiles can be represented with considerable accuracy by Thompson's two-dimensional profile family while the theory based on entrainment and Mager's cross-flow model gives the best over all agreement.

In the final analysis it can be said that there is still not a perfect model of the velocity profiles or shear stress correlation available for the three-dimensional case.

In the present investigation Mager's quadratic expression for the cross-flow and the shear stress profile used by von Karman are employed as the starting point. The validity of these assumptions will then be checked by experimental observations.

2.2 Equations of Motion

The momentum and continuity equations for the boundary-layer in three-dimensional curvilinear rotating frame of reference was first derived by Mager [1]. Allowing for the simplifications within the boundary-layer these equations simplify to give:

$$u_1 \frac{\partial u_1}{\partial X} + v_1 \frac{\partial u_1}{\partial Y} + w_1 \frac{\partial u_1}{\partial Z} + c u_1 w_1 = \Omega_1^2 R_1 \frac{\partial R}{\partial X} - 2\,\Omega_Y w_1$$

$$+ \frac{1}{\rho} \frac{\partial \tau_{XY}}{\partial Y} \qquad \text{X - momentum} \qquad (11)$$

$$u_1 \frac{\partial w_1}{\partial X} + v_1 \frac{\partial w_1}{\partial Y} + w_1 \frac{\partial w_1}{\partial Z} - u_1^2 c = \Omega_1^2 R_1 \frac{\partial R}{\partial X} + 2\,\Omega_Y u_1$$

$$+ \frac{1}{\rho} \frac{\partial \tau_{XY}}{\partial Y} \qquad \text{Y - momentum} \qquad (12)$$

$$- \Omega^2 R_1 \frac{\partial R_1}{\partial Y} + 2\,(\Omega_Z u_1 - \Omega_X w_1) = 0 \qquad (13)$$

$$\frac{\partial u_1}{\partial X} + \frac{\partial v_1}{\partial Y} + \frac{\partial w_1}{\partial Z} + w_1 c = 0 \qquad (14)$$

where R_1 is the perpendicular distance of a particle from the axis of rotation, c is the curvature of the X-axis, Ω_1 is the angular velocity and $(\Omega_X, \Omega_Y, \Omega_Z)$ are the components of vector Ω_1 in curvilinear coordinate system. It is convenient to express the above equations in a rotating cylindrical coordinate system (r, θ, y) with a constant angular velocity Ω and the y axis perpendicular to the (r, θ) plane. This coordinate system is shown in Fig. (2-b). The following transformations are made:

$$\Omega_X = \Omega_Z = 0$$

$$X \to r\,\theta;\ Y \to y;\ Z \to r$$

$$c = \frac{1}{r},\ \Omega_1 = \Omega_Y = -\Omega$$

The mean motion turbulent flow equation governing the flow over the rotating helical blade can thus be written as:

$$\frac{1}{r}\frac{\partial u}{\partial \theta} + \frac{\partial v}{\partial y} + \frac{\partial w}{\partial r} + \frac{w}{r} = 0 \quad \text{continuity} \qquad (15)$$

$$\frac{u}{r}\frac{\partial u}{\partial \theta} + v\frac{\partial u}{\partial y} + w\frac{\partial u}{\partial r} - \frac{w}{r}(2\Omega r - u) = \frac{1}{\rho}\frac{\partial \tau_u}{\partial y}$$

$$\theta \text{ - momentum} \qquad (16)$$

$$\frac{u}{r}\frac{\partial w}{\partial \theta} + v\frac{\partial w}{\partial y} + w\frac{\partial w}{\partial r} - \frac{(\Omega r - u)^2}{r} = \frac{1}{\rho}\frac{\partial \tau_w}{\partial y}$$

$$r \text{ - momentum} \qquad (17)$$

Here, τ_u and τ_w are the components of shear stress in the tangential and radial directions.

The assumptions made in deriving the above equations are:

1. The helical blade is approximated by a flat circular plate with leading and trailing edge. This is permissible because the helix angle is small. The asymmetry of the flow is maintained by assuming that the leading edge is not under the influence of the trailing edge.

2. The flow is turbulent over the entire blade surface.

3. The pressure gradient is zero everywhere in the boundary-layer meaning that the pressure gradient of the main flow is impressed upon the viscous layer near the wall.

4. The flow is incompressible.

5. Turbulent energy terms like $\overline{\rho u^{2}}$ and $\overline{\rho w'^{2}}$ are small and hence not included in the equations. Shear stress terms τ_u and τ_w include both viscous and Reynolds stresses.

The boundary conditions to be satisfied by these equations are:

$$y = 0;\ u = v = w = 0$$

$$y = \infty;\ u = r\Omega,\ w = 0$$

In order to obtain boundary-layer momentum integral equations, equation (15) is used to eliminate the v component of the velocity from Equations (16) and (17), and integrating the results from y = 0 to y = h where h is a distance outside the boundary-layer. This gives

$$\frac{\partial}{\partial\theta}\int_0^h \frac{u}{\Omega r}\left(\frac{u}{\Omega r} - 1\right) dy + \frac{1}{\Omega}\int_0^h \frac{\partial w}{\partial r}\left(\frac{u}{\Omega r} - 1\right) dy + \int_0^h \left(\frac{2uw}{r^2\Omega^2} - \frac{3w}{\Omega r}\right) dy$$

$$+ \frac{1}{\rho}\int_0^h \frac{\partial u}{\partial r}\frac{w}{\Omega r}\, dy = -\frac{1}{\rho\Omega^2 r}\,\tau_{u,o} \qquad (18)$$

$$\frac{\partial}{\partial\theta}\int_0^h \frac{u\,w}{\Omega^2 r^2}\, dy + \frac{2}{\Omega}\int_0^h \frac{\partial w}{\partial r}\frac{w}{\Omega r} + \int_0^h \frac{w^2}{\Omega^2 r^2}\, dy - \int_0^h \left(1 - \frac{u}{\Omega r}\right)^2 dy =$$

$$= -\frac{1}{\rho\Omega 2_r}\,\tau_{w,o} \qquad (19)$$

where $\tau_{u,o}$ and $\tau_{w,o}$ are the components of the wall shear stress in the θ and r direction respectively.

2.3 Approximate Solution of the Momentum Integral Equations

In a previous section it was mentioned that the usual method of attack to three-dimensional turbulent boundary layer equations is to solve a pair of momentum integral equations assuming suitable profiles for the velocities and an empirical relation for the shear stress at the wall. In a situation involving rotating boundary-layers there are essentially no other theoretical techniques available and in these cases the momentum integral method becomes a more practical means of flow analysis.

Using Mager's profile and von Karman's shear stress relation in the following form

$$\tau_{u,o} = 0.0225\ \rho U^2\ R_\delta^{-1/4} \tag{20}$$

$$\tau_{w,o} = \varepsilon_o\ \tau_{u,o} \tag{21}$$

momentum integral equations can be integrated. The resulting equations so derived by Lakshminarayana [2] are (see Appendix A)

$$.0975\ \frac{\partial\delta}{\partial\theta} + 0.208\varepsilon_o\delta + .052\ \varepsilon_o\ r\ \frac{\partial\delta}{\partial r} + 0.052\ \delta r\ \frac{\partial\varepsilon_o}{\partial r}$$

$$= 0.0225\ r\ (R_\delta)^{-1/4} \tag{22}$$

and

$$-0.207\ \frac{\partial}{\partial\theta}\ (\varepsilon_o\delta) - 0.324\ \varepsilon_o{}^2\ \delta - 0.216\ \varepsilon_o\delta\ r\ \frac{\partial\varepsilon_o}{\partial r} - 0.108\ r\ \varepsilon_o{}^2\ \frac{\partial\delta}{\partial r}$$

$$+ .028\ \delta = .0225\ \varepsilon_o r\ (R_\delta)^{-1/4} \tag{23}$$

The solution to the above two first order partial differential equations should give a good quantitative measure of the boundary-layer growth and the limiting streamline angle at all radial and tangential locations. The solution is very difficult to obtain because of the non-linear terms in these equations.

In solving Eqns. (22) and (23), the effect of physical constraints such as the hub and the annulus wall must be taken into account. This means that the radial velocity should vanish at these boundaries. One would also expect ε_o to vanish at the tip. This is confirmed by the experimental observations reported in the next chapter.

An approximate solution to momentum integral equations is obtained by Lakshminarayana [2], assuming that the blade is infinitely extended radially. This means that the radial velocity gradients in the boundary-layer approximately satisfy the following equations

$$\frac{\partial u}{\partial r} \simeq \frac{u}{r} \tag{24}$$

$$\frac{\partial w}{\partial r} \simeq \frac{w}{r} \tag{25}$$

Using these assumptions in momentum integral equations, the equations (22) and (23) reduce to the following form

$$\frac{d\Delta}{d\theta} = - 2.68\ \varepsilon_o \Delta + 0.29\ r \tag{26}$$

$$\frac{d\varepsilon_o}{d\theta} = 0.135 + 0.54\ \varepsilon_o^{\,2} - 0.34 r \frac{\varepsilon_o}{\Delta} \tag{27}$$

where the transformation of the variable δ,

$$\Delta = (R_\delta)^{1/4}\ \delta = \left(\frac{72}{7}\right)^{5/4} R_{\delta^*}^{1/4}\ \delta^* \tag{28}$$

is used to eliminate Reynolds number from the above equations. Here, δ^* is the momentum thickness given by

$$\overset{*}{\delta} = \frac{1}{U^2} \int_0^{\delta} u(U-u)\, dy \qquad (29)$$

The boundary conditions to be satisfied are

$$\Delta = \varepsilon_o = 0 \text{ at } \theta = 0 \text{ (i.e. at the leading edge of the blade)}$$

For any given r, these equations give Δ and ε_o variations with θ, the distance from the leading edge.

Equations (26) and (27) are solved numerically using a fourth order Runge-Kutta method without taking the effect of constraint due to the annulus wall. The solution is valid provided the flow is fully turbulent from the leading edge. Experiments described in Chapter 3, however, show that near the leading edge a laminar region exists and that the transition to turbulent flow occurs at a critical Reynolds number less than that of a flat plate. The analysis developed by Banks and Gadd [7] is used to correct the solution for the initial laminar effect. The final results are plotted in Figs. (3) and (18). It is one of the purposes of this investigation to check the validity of this solution by experiment.

2.4 Asymptotic Disk Values of δ Taking into Account the Flow Constraints Due to Annulus Wall

For large values of θ the flow should approach the asymptotic disk values. Thus it is permissible to drop the terms of the form $\frac{\partial}{\partial\theta}$ from Equations (22) and (23), and using the transformation given by Equation (28), the following equations can be derived:

$$\frac{d\Delta}{dR} = \frac{0.54 r_t}{\varepsilon_o} - 4.78 \frac{\Delta}{R} - 1.25 \frac{\Delta}{\varepsilon_o} \frac{d\varepsilon_o}{dR} \qquad (30)$$

$$\frac{d\varepsilon_o}{dR} = - 1.4 \frac{\varepsilon_o}{R} - 0.4 \frac{\varepsilon_o}{\Delta} \frac{d\Delta}{dR} + \frac{0.14}{\varepsilon_o R} - \frac{0.104 r_t}{\Delta} \qquad (31)$$

where $R = \frac{r}{r_t}$. It is now suggested to predict a function for $\varepsilon_o = f(R)$ based partially on theory and the experiment and then to obtain an approximate solution for Δ from the above equations. A typical experimental and theoretical variation of ε_o with R is shown in Fig. (4) at $\theta = 270$ degrees. Among all the continuous functions that could be fitted to these points, a hyperbolic tangent appears to be the most suitable one. The equation has the following form

$$\varepsilon_o = 0.23 \tan h \, [14.2(1 - R)] \qquad (32)$$

where 0.23 is the asymptotic value of ε_o derived theoretically in Sec. (2.3). Substituting Equation (32) in (30) and (31) gives

$$\frac{d\Delta}{dR} = 3.58 \, \mathrm{CothX} - 4.78 \frac{\Delta}{R} + 17.75 \, \Delta \, \mathrm{SechX} \, \mathrm{CshX} \qquad (33)$$

θ - momentum

$$\frac{d\Delta}{dR} = 6.12 \frac{\Delta}{R} \mathrm{Coth}^2 X - 1.73 \, \mathrm{CothX} - 3.5 \frac{\Delta}{R} + 35.5 \, \Delta \, \mathrm{CschX} \, \mathrm{SechX} \qquad (34)$$

r - momentum

where $X = 14.2(1 - R)$

For the solution of the above equations it is assumed that boundary-layer growth at the hub is zero i.e.,

$$\Delta = 0 \text{ at } R = 0.5$$

Equation (33) is solved numerically using the fourth order Runge-Kutta method. Large boundary-layer growth near the tip is observed. The results are shown in Fig. (4). The second solution obtained from the r-momentum equation is found to be drastically different from that of Equation (33). The reason for such a discrepancy may lie within the assumptions made in deriving the r-momentum equation. In other words the turbulence energy and pressure terms that are neglected in the present analysis are likely to play an important role near the tip. Thus, the future analysis should not only include pressure gradient terms, whose measured values are found to be appreciable as described in Sec. (3.4), but also turbulent terms such as $\overline{\rho w'^2}$ and $\overline{\rho u'^2}$. It is also obvious that the order of magnitude of terms in Equation (33) is much larger than those in the r-momentum Equation (34). Hence the neglection of pressure and turbulence terms is likely to introduce larger errors in Equation (34) than in Equation (33). In summary, it can be concluded that the physically realistic model assumed above for ε_o near the tip cannot be handled mathematically by a simple differential equation. One has to resort to the solution of the Reynolds' equation in such a case.

Although the analysis that has been carried out so far is only preliminary, the experiment has shown relatively good agreement between the two. This is discussed in the next chapter.

3. EXPERIMENTAL PROGRAM

3.1 Apparatus Used in the Experiment

a. - Helical Blade

For the purposes of experimental investigations a helical blade of constant thickness with an axial advance of 10 inches was designed and built out of fiberglass. The blade is mounted within an annulus with 0.08 inches of clearance between the blade and the annulus wall. The details of the blade are shown in Fig. (5-a) and (5-b). The circumferential extent of the blade is 300 degrees from the leading edge. Metallic tubes of 1/4 inch in diameter are embedded in the blade at 30° degree intervals for a total of 10 stations. These tubes are used to determine the limiting streamline angle as well as the static pressures on the front and back surfaces of the blade. The notation given in Fig. (5-b) is used throughout this report, i.e., $\theta = 150°$ and $r = 17"$ refers to a tangential location of 150 degrees from the leading edge and a radial location of 17 inches from the axis of rotation.

Unless otherwise stated, all profile measurements are carried out at the rotational speed of 450 rpm corresponding to a Reynolds number of $7 \times 10^{+5}$ based on the tip radius. Since all the measurements are taken relative to the rotating system, the following two devices are used.

b. - One Channel Pressure Transfer Device (PTD)

This is a modified and improved version of the three channel (PTD) explained in Ref. [6]. The object is to transfer pressures from the rotating blade to a stationary precision manometer. This device is shown in Fig. (6). The surface of the shaft in contact with the O-rings is

coated with self lubricating teflon for smoother contact and also to prevent leakage. This device is mounted inside the hub nose cone with the shaft clamped to stop it from rotating. However, the main body containing the O-rings rotates along with the hub to allow the pressures to be transferred from the blade through the channel between the O-rings and to the manometer. The schematic diagram of the entire assembly is shown in Fig. (7).

c. - Ammonia Transfer Device (ATD)

This device is similar to the PTD and is used to transfer the ammonia gas from the stationary source of ammonia contained in a cylinder to the desired location on the rotating blade surface. It is mounted in a similar manner to PTD. The method of measuring ε_o is described in Sec. (3.3-b).

3.2 Instrumentation

Three different kinds of probes are used in measuring the velocity profiles, wall skin friction and the flow angle within the blade boundary-layer. A photograph of the probes is given in Figure (8).

Probe No. 1 is a boundary-layer probe which is essentially a total pressure probe. The tip of the probe is flattened to minimize the shift in effective center. This probe is used to determine tangential velocity profiles at various stations on the blade as well as the boundary-layer thickness.

Probe No. 2 is a total pressure probe commonly referred to as Preston tube, since it was first used by Preston for skin friction measurements. It is bent as shown in Fig. (8) for least interference of

the flow in the boundary-layer as well as for better adjustment at different radii.

Finally, probe No. 3 is a two hole yawmeter used to detect the flow angles inside the boundary-layer. Detailed dimensions of all these boundary layer probes are given in Fig. (8).

All three kinds of probes introduced above are installed on the same mounting mechanism for different experimental purposes. A schematic diagram of this device is given in Fig. (7). The distance between the mounter and the point at which the data are taken is far enough (8 inches) to insure the least interference with the flow in the layer. Thus the probes are inserted into the layer from outside and proper adjustments are made prior to each individual measurement. The methods of recording the data are described in the subsequent sections.

3.3 Flow Visualization Experiment

a. - Location of the Flow Transition Zone

The analysis carried out by Lakshminarayana [2] and summarized in Sec. (2.3) is based on the assumption that the flow is completely turbulent over the entire blade surface. If the extent of initial laminar region is known, it is possible to combine this analysis with those developed by Banks and Gadd [7] for laminar flow to predict accurately the boundary-layer growth throughout the blade surface. The procedure adopted here for finding the extent of initial laminar region is known as the sublimation technique. The method consists of coating the blade surface with a smooth, white thin film of a chemical solid, spraying it with a chemical liquid until the film becomes transparent, and then exposing it to the air flow for a few minutes until evaporation has

taken place. The evaporation takes place faster in the turbulent region than in the laminar region and an indication is given by the whiteness of the former and the darkness of the latter regions.

After several methods are tried it is found that the technique suggested in Ref. [4] is the most suitable one to apply. The solid chemical selected is china clay and a solution is prepared according to the following formula:

China Clay	160 gr.
Water	250 ml.
Acetone	300 ml.
Glycerol	5 ml.

The mixture is sprayed over the surface and allowed to dry. The result is a white film of china clay uniformly coating the surface. When a chemical liquid of the same index of refraction is sprayed over the coating, the film becomes transparent, but the white deposit reappears as soon as the evaporation is completed.

The liquid selected is nitrobenzene. An indication of the transition zone is obtained after the blade is allowed to rotate for about three minutes. A typical photograph of the transition zone is given in Fig. (9). The line of transition of the mid chord length corresponds to a distance of 44 degrees from the leading edge. The corresponding Reynolds number is 3.0×10^5 which is smaller than the critical Reynolds number of a flat plate boundary layer, 3.2×10^5. Figure (9) also indicates that near the tip and the hub, the flow becomes turbulent much earlier. This is further confirmed by the velocity profile measurements reported in the next section. The sharp leading edge of the blade has caused early transition to

turbulence to take place but relaminarization occurs immediately thereafter.

b. - Measurements of the Limiting Streamline Angle

The limiting streamline angle ε_o is determined using the ammonia transfer device described in Sec. (3.1-b). A second method is also used at lower rpm as a check on the accuracy of the ammonia streak method. This method is described first.

A solution of titanium tetrachloride and carbon tetrachloride is prepared. When exposed to the airflow this solution generates a white, dense smoke capable of being photographed. The mixture is brushed on the surface of the blade at the desired locations and photographs are taken while the blade is rotating. The deflection of the smoke filament from the tangential position gives an indication of ε_o. This technique is found to be successful at lower angular velocities (100 rpm) where the flow is predominantly laminar, but the smoke rapidly diffuses at higher speeds (450 rpm) when the flow is turbulent, before any pictures can be taken. Figure (10-a) shows a typical of such measurements. However, as it was mentioned earlier, this method is used to check on the accuracy of the ammonia streak technique described below.

First, a number of small diameter holes are drilled on the blade surface through the metallic tubes. Using ATD a small amount of ammonia gas at very low velocities is fed into the tubes at various tangential locations. A sheet of ozalid paper sensitive to ammonia is pasted along the edges of the static holes and thus traces of ammonia are recorded on the ozalid paper while the blade is in rotation. Figure (10-c) shows some typical traces of ammonia at a particular location. The amount of deflection from the tangential direction gives

the value of ε_o at that location. This procedure is repeated several times at each point to make certain the angles obtained are accurate. In Fig. (3) variations of ε_o with θ are given. The vertical lines indicate the amount of experimental scatter. This experimental scatter, however, is only a few degrees at the most.

A few interesting conclusions may be deduced by comparing experimental and theoretical values of ε_o from Fig. (3). It is seen that much larger values of ε_o are obtained in the laminar region than in the turbulent region. This is in conformity with the analysis of Banks and Gadd [7] for a screw propeller. At the trailing edge ($\theta>5$ rad.) a consistent decrease in values of ε_o are observed at all radii accounting for the decay of the radial velocity as the flow leaves the trailing edge.

Radial variations of ε_o are shown plotted in Fig. (11) for various fixed tangential locations on the blade surface. For accurate predictions of ε_o, the Equations (22) and (23) have to be solved simultaneously without neglecting any terms. The analysis carried out in Sec. (2.3) does not take into account constraint due to the annulus wall and hence predicts $\frac{d\varepsilon_o}{dr} = 0$. Experimental results seem to indicate that this is true at most of the radial locations except near the tip, where a decrease in ε_o is observed. This important boundary condition must be taken into account when the complete momentum integral equations are solved. Thus, it can be said that the solution of Equations (26) and (27) which predicts a constant value of ε_o with radius may not be valid near the tip.

Generally speaking the agreement between measured and predicted values of ε_o is very close at most tangential locations. Departure

between the theory and experiment near the leading edge at R = 0.55 and R = 0.965 is due to early flow transition at these locations.

3.4 Blade Static Pressure

The theoretical analysis presented in Chapter 2 is based on the assumption that the pressure gradient of the flow is zero everywhere in the field. To check the validity of this assumption, the static pressures are measured on the back and front surfaces of the blade using the PTD and the static holes drilled on the surface. The radial variations of the non-dimensionalized static pressure coefficient ψ_s at two typical locations are plotted in Fig. (12). ψ_s is defined as

$$\psi_s = 2gh/U_t^2 \tag{35}$$

where U_t is the tip velocity and h is the static head. It is seen from the figure that the radial pressure gradient is negligibly small throughout the flow field except, perhaps, near the tip. A flag test carried out near the tip shows that there is no appreciable pre-swirl existing in the incoming flow. Thus the reason for such a large radial pressure gradient at the tip may be due to high turbulence mixing, interaction between blade and annulus wall boundary layer and clearance effects. Therefore, in the analysis of the flow near the tip, energy terms such as $\rho\overline{u'^2}$ and $\rho\overline{w'^2}$ are likely to be large and play an important role in the radial momentum equation.

3.5 Tangential Velocity Profiles

This section describes tangential velocity profile measurements carried out by means of the boundary-layer probe described in Sec. (3.2).

The probe is clamped rigidly to a mounter such that the stem is parallel to the axis of the rotation and the sensing head is in the direction of the relative tangential flow. The block (a) shown in Fig. (7) is capable of moving up and down to enable the measurements to be taken at various radial locations. Boundary-layer profile measurements at other tangential blade locations are carried out by shifting the entire mounting assembly to desired tangential stations. Thus at each fixed (r, θ) location, the probe is traversed in a direction normal to the blade surface until the free stream velocity is observed. This axial distance is taken to be the boundary-layer thickness at that location. The total pressures sensed by the probe are transferred to a precision manometer through the pressure transfer device PTD . If P_o is the pressure recorded by the manometer the dynamic head of the relative flow is given by (the blade static pressure is the same as the ambient pressure)

$$\frac{1}{2}\rho U^2 = P_o + \frac{1}{2}\rho\,(r\Omega)^2 \qquad (36)$$

where r is the radial distance at which P_o is recorded. At the edge of the boundary-layer where the value of $u = r\Omega = U$, P_o will be zero. Knowing P_o and the local blade speed, the values of u can be computed from Equation (36). The velocity profiles so measured are shown in Fig. (13). The agreement between the 1/7 Power Law and the experiment is generally good. The departure of the measured profile from the 1/7 Power Law occurs only near the tip. This is the region where appreciable radial pressure gradients are found to exist. Note that at $\theta = 30°$ and $r = 11$, 13 and 15 [Fig. (13-a)], where the measurements are taken within the initial laminar region, the shape of the velocity profile is

parabolic, typical of laminar profiles. This is in conformity with the Banks and Gadd [7] theoretical prediction plotted in the same figure. Near the hub and the tip, where the flow is turbulent, the shape of the velocity profiles are typical of turbulent flows. These quantitative results are in agreement with the earlier qualitative results obtained in Sec. (3.3-a). Apart from this particular tangential location, the profiles obtained at other locations on the blade show good agreement with the assumed 1/7 Power Law.

It is also advantageous to replot Fig. (13) using momentum thickness δ^* given by Equation (29) instead of δ as a non-dimensionalizing parameter, because the experimental values of δ may have been overestimated. Therefore, using measured values of u, U and δ, momentum thickness is determined by numerical integration of Equation (29). Velocity profiles are replotted in Fig. (14) using this approach. The agreement with 1/7 Power Law is extremely good except near the tip radius where the profiles are steeper. The tabulated values of complete tangential velocity profiles are given in Table I.

It is now possible to determine the shape factor H, defined as

$$H = \frac{\delta_1}{\delta^*} \tag{37}$$

where δ_1 is the displacement thickness given by

$$\delta_1 = \frac{1}{U} \int_0^{\delta} (U-u)\, dy \tag{38}$$

The shape factor gives the change in the velocity profile of the boundary-layer. These values are tabulated in Table III. The corresponding value of H for a flat plate at zero incidence is 1.285. At $\theta = 30°$

(Table III), values of H are closer to 2.00, indicating the region where laminar flow exists. This is consistent with velocity profile and flow visualization reported earlier. At all other tangential locations the values of shape factor are very close to that of a flat plate at zero incidence.

3.6 Radial Velocity Profiles

The method of obtaining radial velocity profiles is to determine the flow angle within the boundary layer at various locations by means of the two hole yawmeter probe. The probe is mounted in the same way as the boundary-layer probe discussed in Sec. (3.5).

The usual way of finding the flow direction is to nullify the pressures read by each individual probe hole of a yaw or wedge probe by turning it through appropriate angles. This method is found to be difficult and time consuming since the probe is rotating. An alternate method is to align the probe relative to a fixed direction (tangential direction in the present case) and record the pressure difference registered by two faces of the probe. Then using the calibration curve given in Fig. (15) it is possible to determine the local flow angle α_1 within a reasonable degree of accuracy.

If ε denotes the local values of the tangents of the flow angles, then

$$\varepsilon = \tan \alpha_L = \frac{w}{u} \tag{39}$$

and the measured g function is given by

$$g = \frac{w}{\varepsilon_o u} = \frac{\varepsilon}{\varepsilon_o} \tag{40}$$

whereas the theoretical assumed function for g is given by Equation (4).

Equation (4) is shown plotted in Fig. (16) by a solid line. To compare assumed and experimental profiles, the values of ε are divided by ε_o at the wall and are tabulated in Table II. In obtaining these values, the difference in pressure detected by the probe is divided by $q = \frac{1}{2}\rho u^2$, which is the local dynamic head of the tangential flow. This may give slightly higher angles at the large values of w, the radial velocity. Therefore, a second approximation is carried out using the dynamic head of the resultant flow given by

$$Q = \frac{1}{2}\rho\ (u^2 + w^2)^{1/2} \qquad (41)$$

The angles are found to be a few degrees smaller near the blade surface. These values are plotted in Fig. (16) vs. y/δ. All the curves show a similar trend at all radii. The experimental curves reach a maximum value slightly away from the wall and drop to zero as the edge of the layer is approached. This shows relatively large departure from the assumed profile especially near the blade surface.

In Fig. (17) a triangular or hodographic plot of the velocities are given. The curves show up to 6 degrees difference in the values of ε_o derived by this method and the ones obtained from ammonia stream technique. In the region II, however, a consistent trend is observed. The predicted angles by these figures at two different tangential locations differ only by a small amount. That is

$$\text{Tan}^{-1} A = 34.6^\circ \quad \text{at } \theta = 150^\circ$$

$$\text{Tan}^{-1} A = 37.2^\circ \qquad \theta = 210^\circ$$

It is evident from this discussion that the measured radial velocities are in qualitative agreement with Mager's profile and in quantitative agreement with region II of Johnston's model. It is likely that the measurements very close to the blade surface are in error.

3.7 Comparison Between Predicted and Measured Values of Momentum Thickness of the Boundary-Layer

Experimental and predicted values of the growth of momentum thickness δ^* at various locations on the blade surface are plotted in Fig. (18). The agreement is reasonably good at all the radii except near the tip where a large departure is observed. It is seen that at the trailing edge ($\theta > 5$ rad.) and at all the radii, experimental points deviate from the expected steady state disk values. This might be due to the influence of the wake. In general boundary-layer growth both in laminar and turbulent flow regions are predicted accurately.

3.8 Measurements of the Skin Friction

The two-dimensional turbulent boundary-layer measurements have revealed that an adequate picture of the flow can be obtained if one distinguishes between an inner region and an outer region. In the inner region, or sometimes referred to as the wall region, the flow is influenced by the fluid viscosity and the wall shear stress. The thickness of this layer is approximately 0.1δ to 0.2δ. The velocity distribution may be described by

$$u/u^* = f\left(\frac{yu^*}{\nu}\right) \equiv f\left(y^+\right) \qquad (42)$$

where u^* is the frictional velocity equal to $\left(\frac{\tau_o}{\rho}\right)^{1/2}$

The shear stress variation in this region is small and could be considered constant to a certain degree of approximation. If the wall is smooth there exists a viscous sublayer adjacent to the wall whose thickness is approximately 0.001δ to 0.01δ. In this region the viscosity dominates the entire sublayer and the mean velocity increases linearly with the distance from the wall. A small transition region connects the viscous sublayer to the wall layer. In the rest of the inner layer the flow is fully turbulent and eddy viscosity varies linearly with the wall, resulting in a logarithmic distribution of the mean velocity. It is well known that the inner region is not directly influenced by the flow conditions outside the boundary-layer.

The rest of the boundary-layer, about 80% to 90%, is called the outer layer. Here, the mean flow may be descirbed by a relationship known as velocity defect law.

$$\frac{U-u}{u^*} = F\ (y/\delta) \tag{43}$$

This region is highly influenced by the external conditions.

For the determination of the wall skin friction τ_o, the Preston tube technique is employed. The fundamental principle governing this technique lies within the meaning of the Equation (42). A pitot tube of given dimensions resting on the blade surface in the direction of the flow measures a total pressure P_o, which is related to the wall shear stress. This pressure reading must obviously depend on ρ, ν, and the diameter of the probe d. Such a dependence is given by the following general equation suggested by Preston

$$\frac{P_o - P_s}{\rho\nu^2}\ d^2 = f\left(\frac{\tau_o d^2}{\rho\nu^2}\right) \tag{44}$$

where P_s is the static pressure. The above equation was further developed by Preston [17] to the following form

$$\log_{10}\left(\frac{\tau_o d^2}{4\rho\nu^2}\right) = \overline{2}.64 + 7/8 \log_{10}\left(\frac{P_o - P_s}{4\rho\nu^2} d^2\right) \quad (45)$$

Using the above equation and the measured values of $P_o - P_s$, it is possible to determine the wall skin friction τ_o. This leads to the determination of the skin friction coefficient C_f from the following equation

$$C_f = 2\tau_o/\rho U^2 \quad (46)$$

where U is the free stream velocity.

In order to determine the effect of Reynolds number based on radius and to compare it with the expression given by von Karman for a free rotating disk, the values of τ_o are determined at different rotational speeds of 100, 200, 300, 450, 500, and 600 RPM. These values are plotted in Fig. (19) and are compared with von Karman's expression. It is seen that higher values of C_f are obtained for the helical blade. If an average curve is drawn through these points it may be expressed by the following equation

$$C_f = .079\ R_r^{-1/5} \quad (47)$$

where $R_r = \frac{\Omega r^2}{\nu}$.

3.9 Application of the Law of the Wall and Wake to the Three-Dimensional Boundary-Layer on the Helical Blade

The determination of τ_o by the Preston tube technique requires that the inner region exists. This may be checked as follows. If u* is the frictional velocity then

$$u^* = \left(\frac{\tau_o}{\rho}\right)^{1/2} = 0.707\ U\ C_f^{1/2} \qquad (49)$$

u^* is a measure of the intensity of turbulent eddying and of the transfer of momentum due to these fluctuations. Equation (49) can also be written in the following form

$$u/u^* = 1.412\ C_f^{-1/2}\ u/U \qquad (50)$$

From Equation (50) the values of u/u* are determined by substituting experimental values of C_f and u/U. These values are plotted in Fig. (20) vs. $y^+ = \frac{yu^*}{\nu}$, using the logarithmic velocity distribution of the form

$$u/u^* = A \log_{10} y^+ + B \qquad (51)$$

where A and B are experimentally determined constants. The values of A and B used here are 5.8 and 5.0 respectively. These numbers may be varied at different locations to obtain a better fit with the data points.

It is interesting to observe that the two-dimensional logarithmic velocity profile does indeed give good results in this particular three-dimensional configuration even though the constants used are slightly different. As in the case of high Reynolds number flow with zero pressure gradient, the law of the wall [Equation (51)] is obeyed by the tangential component of the boundary-layer velocity on a rotating helical blade.

4. CONCLUSIONS

The following conclusions may be drawn from the theoretical and analytical investigations reported in this thesis.

1) The solution of approximate momentum integral Equations (26) and (27) predicts reasonably well the boundary-layer growth Δ [see Equation (28)] and the limiting streamline angle ε_o at various locations on the rotating blade surface. Although the effects of physical constraints due to annulus and hub walls are neglected, these predictions seem to agree closely with the experimental observations at all radii except very near the tip. Large departure from the asymptotic disk values of Δ at the tip may be due to substantial turbulence mixing and interaction between annulus and blade boundary-layers. These solutions also predict a constant value for ε_o with θ, the limiting streamline angle, at all radii, but the experiment seems to indicate that ε_o should vanish at the tip. The solution to Equations (22) and (23) should give a more realistic estimate of the boundary-layer flow over a rotating helical blade. The fact that turbulent energy terms are likely to be high near the tip indicates that they may not be neglected in the complete analysis of the flow in this region.

2) The static pressure measurements on the blade surface show that no appreciable pressure gradient exists in the flow except near the tip. Such large radial pressure gradients substantiate the existence of high turbulence levels and other factors described above.

3) Agreement between the assumed and measured tangential velocity profile is generally good. Some departure from 1/7 Power Law occurs as

the tip is approached. In this region, the exponent in the Power Law representation of the velocity profile is likely to be 1/8 or 1/9.

4) The radial velocity profiles show a substantial amount of difference between Mager's profile and the experimental observations. This is in contradiction with the recent report of Cham and Head [11] whose measured values on a free disk seem to agree with Mager's profile better than any other existing flow model. Application of Johnston's triangular model seems to give closer agreement in the outer region although such a model predicts larger limiting streamline angles than those obtained by the author.

5) The skin friction measurements carried out on the helical blade surface are generally 40% higher than the expression used by von Karman. It seems that the skin friction can be expressed as a function of one variable, $R_r(\frac{\Omega r^2}{\nu})$, the Reynolds number based on radius.

6) Application of the two-dimensional velocity profile to this three-dimensional configuration results in an almost perfect fit with the measured data points, except near the tip where the general trend of the curves remains unchanged but seems to yield different constants in the Law of the Wall. It is the author's feeling, based upon experimental observations, that the two-dimensional Law of the Wall could very well be extended to include three-dimensional flows.

7) The use of three-dimensional momentum integral equations together with (a) the circumferential velocity profile represented by the 1/7 Power Law or the well known Law of the Wall, (b) the radial velocity profile represented by Mager and (c) the skin friction expression given by the author should provide a fairly good estimate of the boundary-layer characteristics over the rotating helical blade.

APPENDIX A

Derivation of Equations (22) and (23) is as follows:

$$\frac{1}{r\Omega^2}\int_o^h \frac{\partial}{\partial r}(u\,w)\,dy = \frac{1}{r}\frac{\partial}{\partial r}\int_o^h \left(\frac{u}{r\Omega}\frac{w}{r\Omega}\,r^2\right) dy$$

$$\frac{1}{\Omega}\int_o^h \frac{\partial w}{\partial r}\,dy = \frac{1}{r}\frac{\partial}{\partial r}\int_o^h \left(\frac{w}{r\Omega}\right) r^2\,dy - \int_o^h \frac{w}{r\Omega}\,dy$$

$$\frac{2}{r\Omega^2}\int_o^h \frac{\partial w}{\partial r}\,w\,dy = \frac{1}{r}\frac{\partial}{\partial r}\int_o^h \left(\frac{w}{r\Omega}\right)^2 r^2\,dy$$

At $y = 0$ and h, $w = uw = 0$.

Thus Equations (18) and (19) reduce to

$$\frac{\partial}{\partial\theta}\int_o^h \frac{u}{r\Omega}\left(1 - \frac{u}{r\Omega}\right) dy + 2\int_o^h \frac{w}{r\Omega}\left(1 - \frac{u}{r\Omega}\right) dy + \frac{1}{r}\frac{\partial}{\partial r}\int_o^h$$

$$\frac{w}{r\Omega}\left(1 - \frac{u}{r\Omega}\right) r^2\,dy = \frac{1}{\rho\Omega^2 r}\,\tau_{u,o}$$

$$-\frac{\partial}{\partial\theta}\int_o^h \frac{u\,w}{r^2\Omega^2}\,dy - \int_o^h \frac{w^2}{r^2\Omega^2}\,dy + \int_o^h \left(1 - \frac{u}{r\Omega}\right)^2 dy - \frac{1}{r}\frac{\partial}{\partial r}$$

$$\int_o^h \left(\frac{w}{r\Omega}\right)^2 r^2\,dy = \frac{\varepsilon_o}{r\rho\Omega^2}\,\tau_{w,o}$$

Substituting Equations (2), (3), (20), and (21) in the above integral equations and carrying out the integration process gives Equations (23) and (24). In a similar manner, Equations (26) and (27) may be derived using the fact that $\frac{\partial w}{\partial r} \simeq \frac{w}{r}$ and $\frac{\partial u}{\partial r} \simeq \frac{u}{r}$ inside the boundary-layer.

REFERENCES

1. Mager, A., "Generalization of Boundary-Layer Momentum Integral Equations to Three-Dimensional Flows Including Those of Rotating Systems", NACA Technical Note, No. 2310, March, 1951.

2. Lakshminarayana, B., "Investigation and Analysis of Flow Phenomena of Secondary Motions in Axial Flow Inducers", Semi-Annual Progress Report to NASA, The Pennsylvania State University, May, 1968.

3. Prandtl, L., "On Boundary-Layer in Three-Dimensional Flow", R&T No. 64, British M.A.P., May, 1946.

4. Richard, E. J. and Burstall, F. H., "The China Clay Method of Indicating Transition", Report and Memoranda No. 2126, N.P.L. August, 1945.

5. Schlichting, H., Boundary-Layer Theory, McGraw Hill Book Co., 1968.

6. McCafferty, H. G., "Errors in Measuring the Fluctuating Flow at the Discharge of an Inducer", M. S. Thesis, Dept. of Aerospace Engineering, The Pennsylvania State University, December, 1966.

7. Banks, W. H., Gadd, G. E., "A Preliminary Report on Boundary-Layers on Screw Propellers and Simpler Rotating Bodies", Ship Division, N.P.L., England, March, 1962.

8. Gruchwitz, E., "Turbulente Reibungasschichten mit Sekundarstronung", Ingenieur-Archiv, Bd. VI, 1935.

9. Johnston, J. P., "On the Three-Dimensional Turbulent Boundary Layer Generated by Secondary Flow", Journal of Basic Engineering, Page 233, March, 1960.

10. Stain, W. C., "The Three-Dimensional Turbulent Boundary Layer on a Rotating Disk", The Aerophysics Department, Mississippi State University, Res. Rep. No. 35, August, 1961.

11. Cham, T. S. and Head, M. R., "Turbulent Boundary-Layer Flow on a Rotating Disk", J. Fluid Mech., Vol. 37, Part 1, pp. 129-147, 1969.

12. Karman, Th., von, "On Laminar and Turbulent Skin Friction", NACA TM 1092, 1946.

13. Perry, A. E. and Joubert, P. N., "A Three-Dimensional Turbulent Boundary-Layer", J. Fluid Mech., Vol. 22, Part 2, pp. 285-304, 1965.

14. Gregory, N., Stuart, J. T. and Walker, W. S., "On The Stability of Three-Dimensional Boundary-Layers with Application to the Flow Due to a Rotating Disk", Phil. Trans. A 248, 155-99, 1955.

15. Francis, G. P. and Pierce, F. J., "An Experimental Study of Skewed Turbulent Boundary-Layers in Low Speed Flows", Journal of Basic Engineering, Trans. ASME, Series D, Vol. 89, pp. 597-608, 1967.

16. Goldstein, S., "On the Resistance to the Rotation of a Disk Immersed in a Fluid", Proc. Camb. Phil. Soc. 31, 232, 1935.

17. Preston, J. H., "The Determination of Turbulent Skin Friction by Means of Pitot Tube", Journal of The Royal Aeronautical Society, Vol. 58, February, 1954.

18. Cornish, J. J., III, "A Universal Description of Turbulent Boundary-Layer Profiles With or Without Transpiration", Aerophysics Department, Mississippi State University, Research Report No. 29, June, 1960.

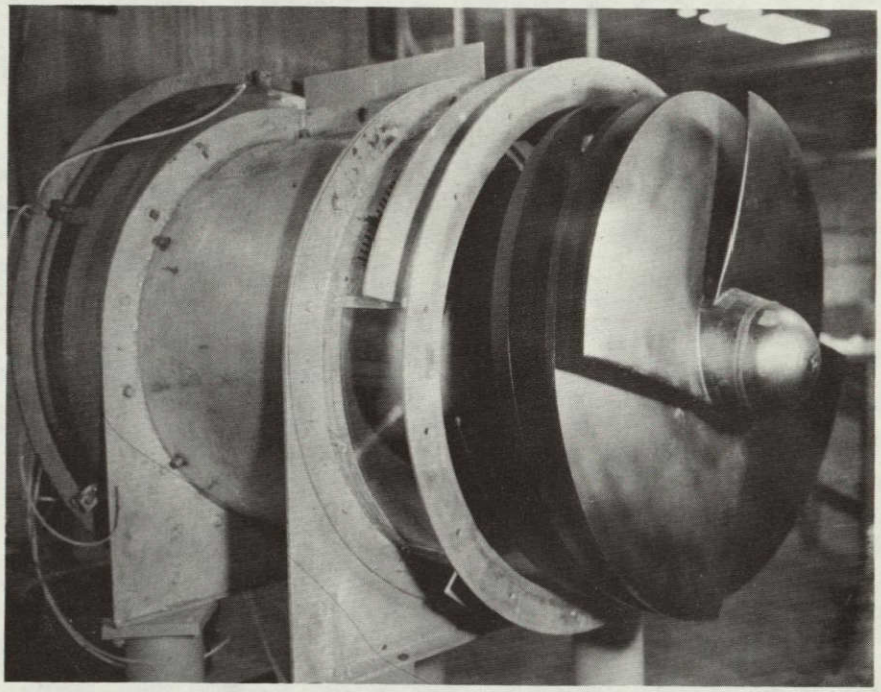

Figure 1: Photograph of an Inducer

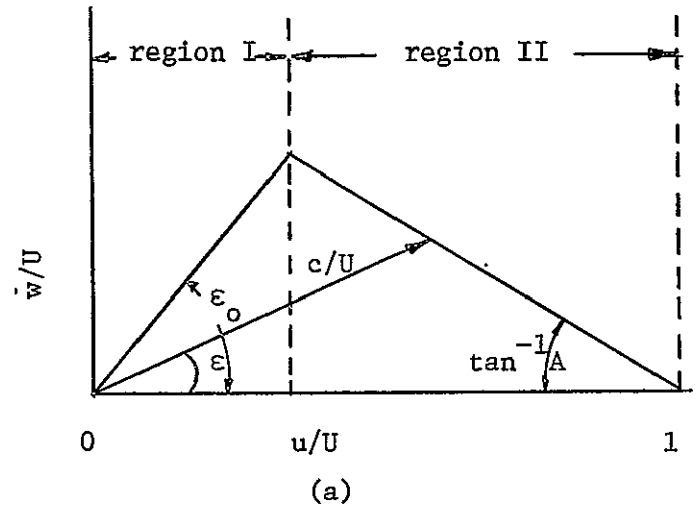

(a)

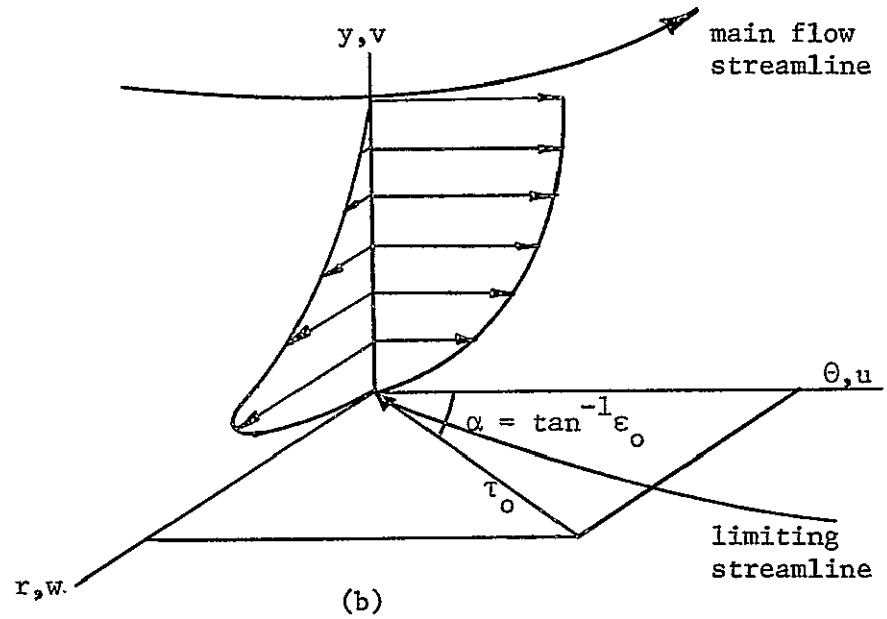

(b)

Figure 2: (a) Johnston's Profile Model, (b) Coordinate System and the Assumed Velocity Profiles

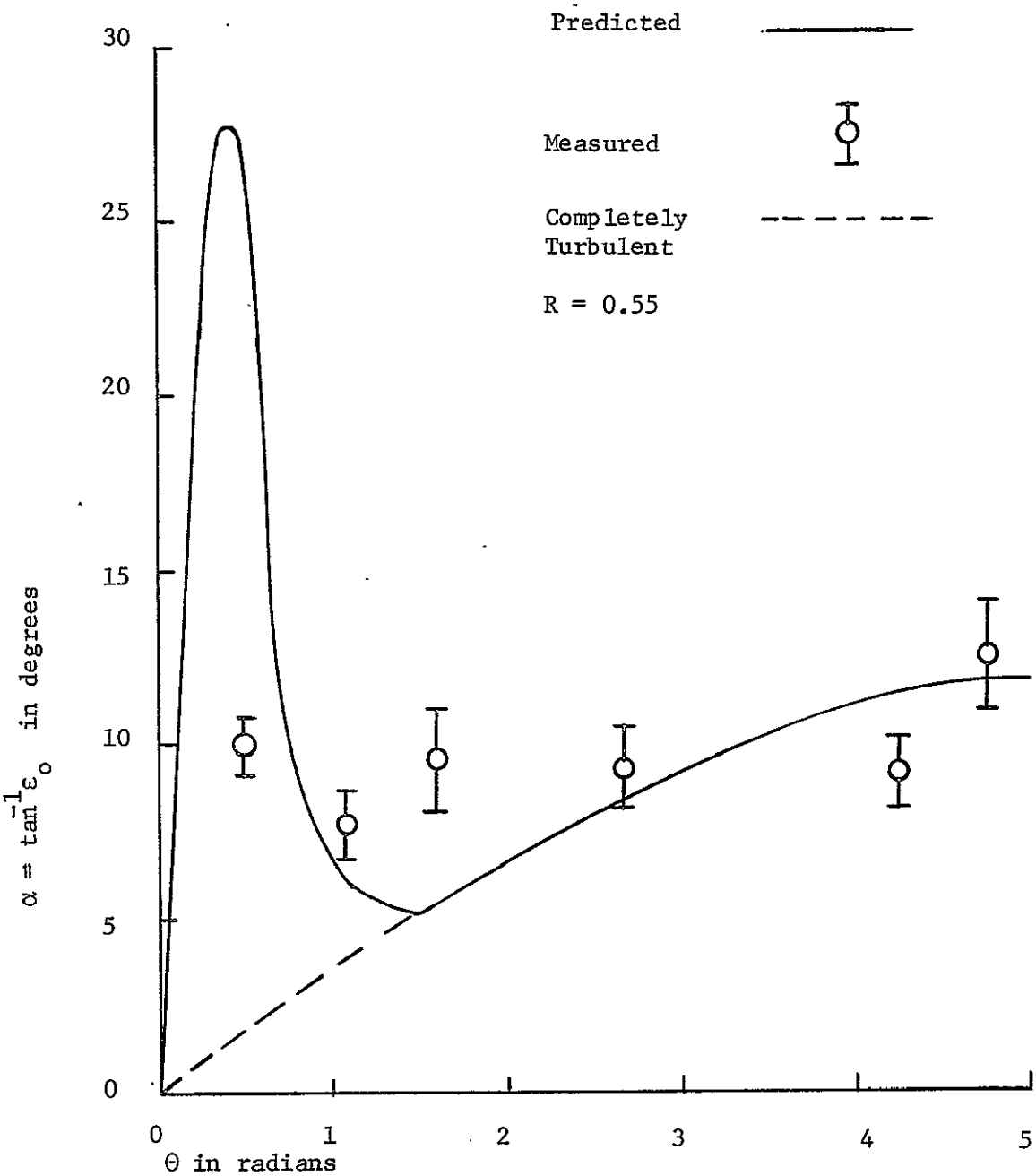

Figure 3-a: Variations of the Limiting Streamline Angle ε_o with Θ

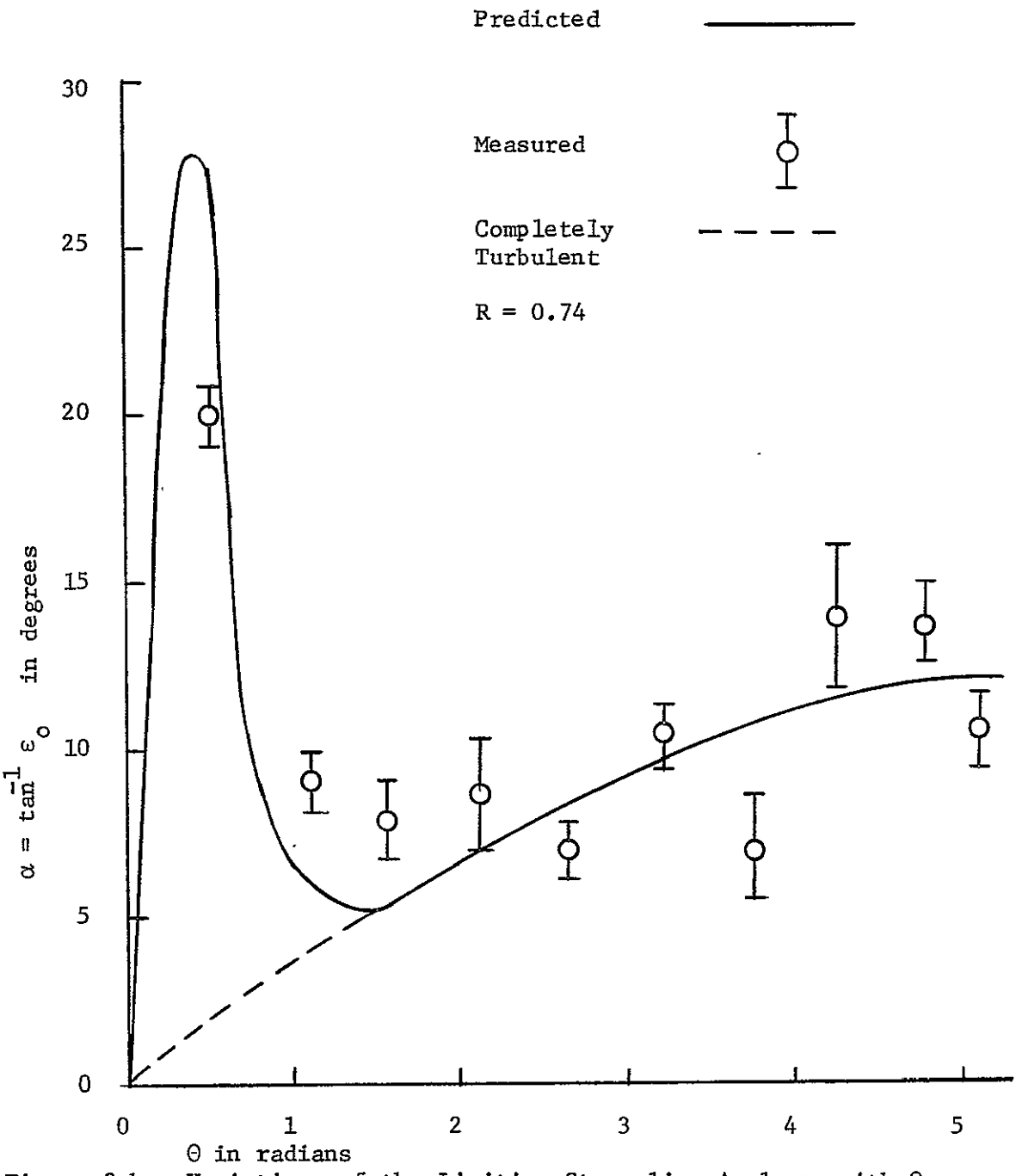

Figure 3-b: Variations of the Limiting Streamline Angle ε_o with Θ

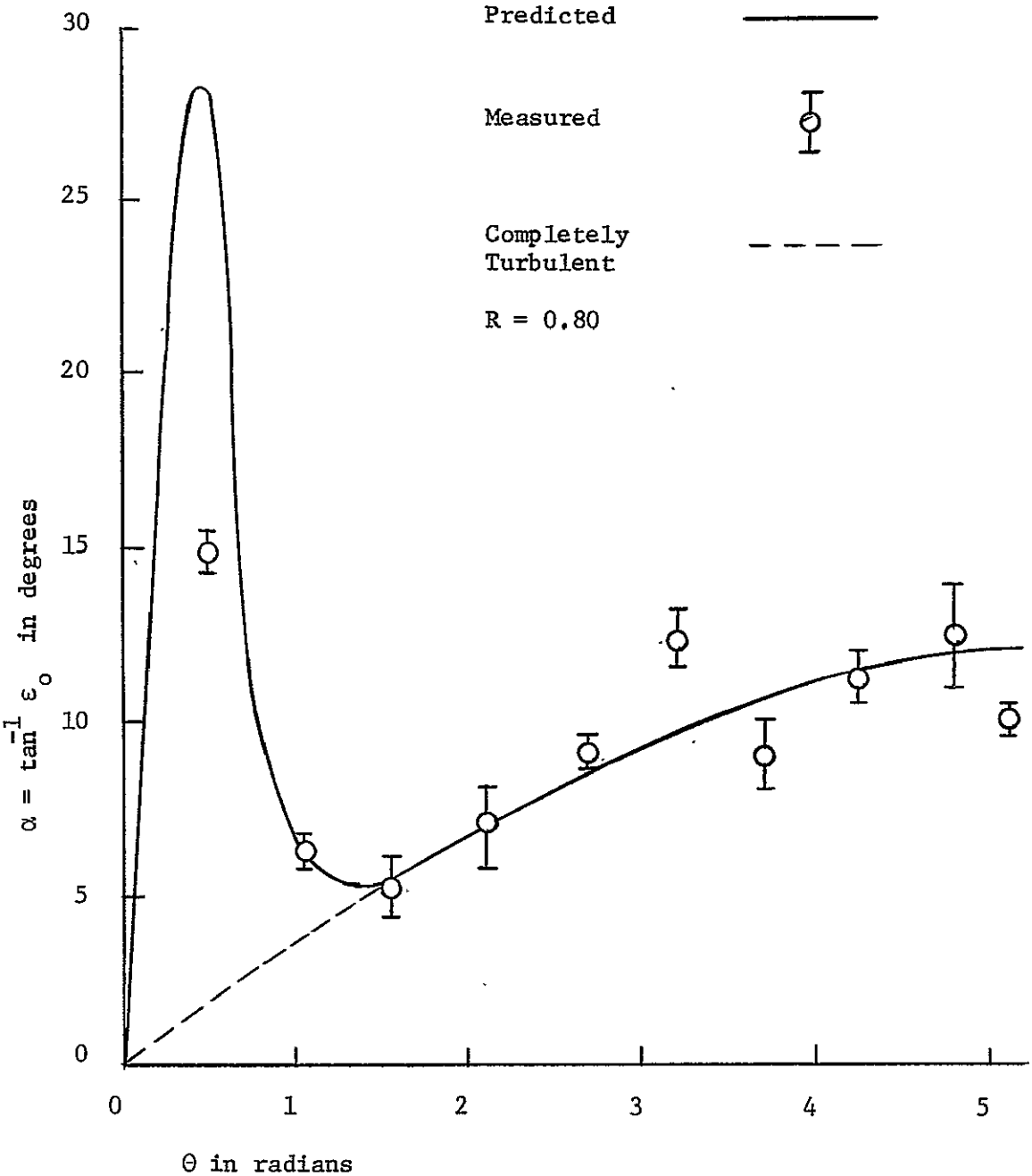

Figure 3-c: Variations of the Limiting Streamline Angle ε_o with Θ

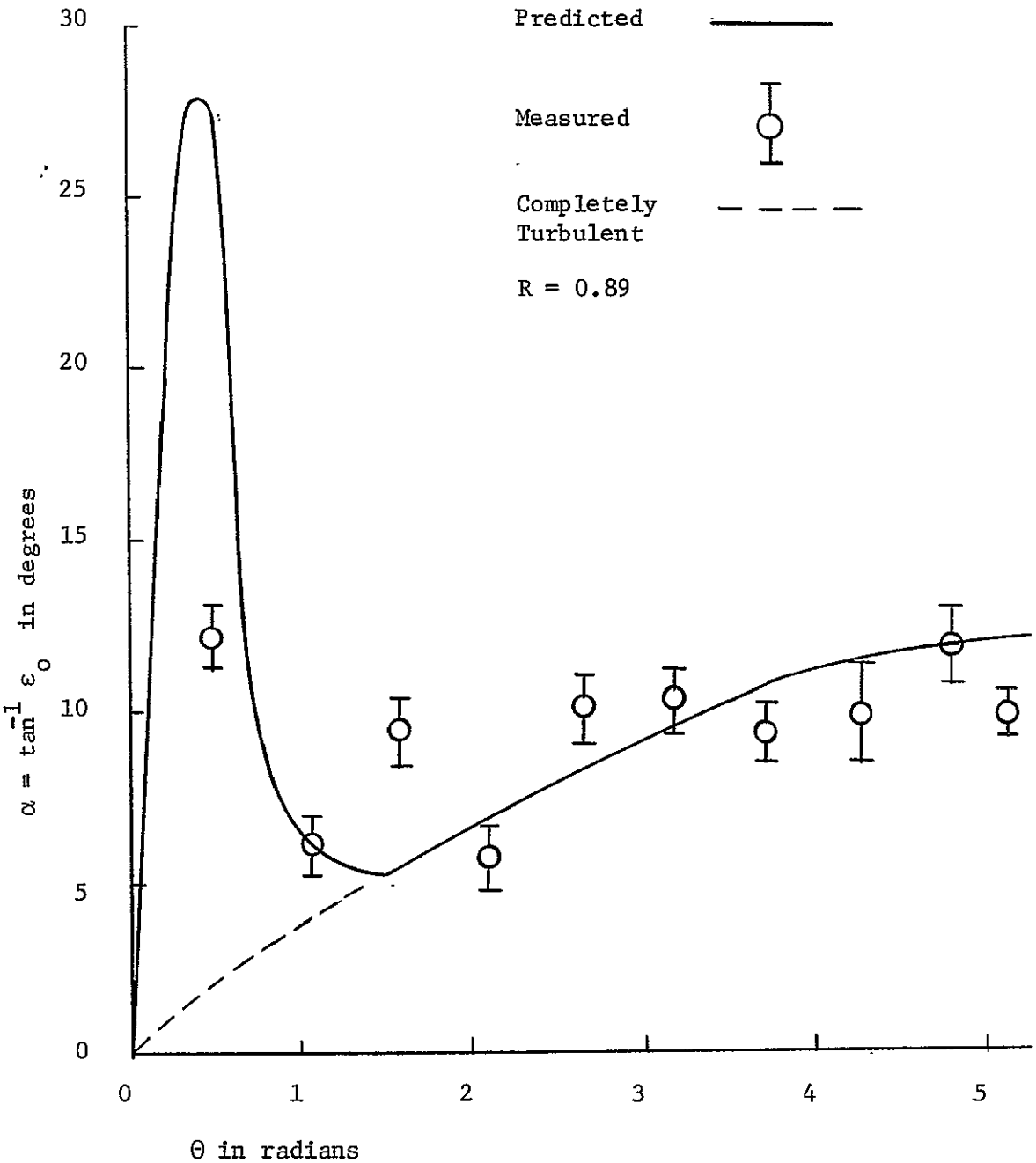

Figure 3-d: Variations of the Limiting streamline Angle ε_o with Θ

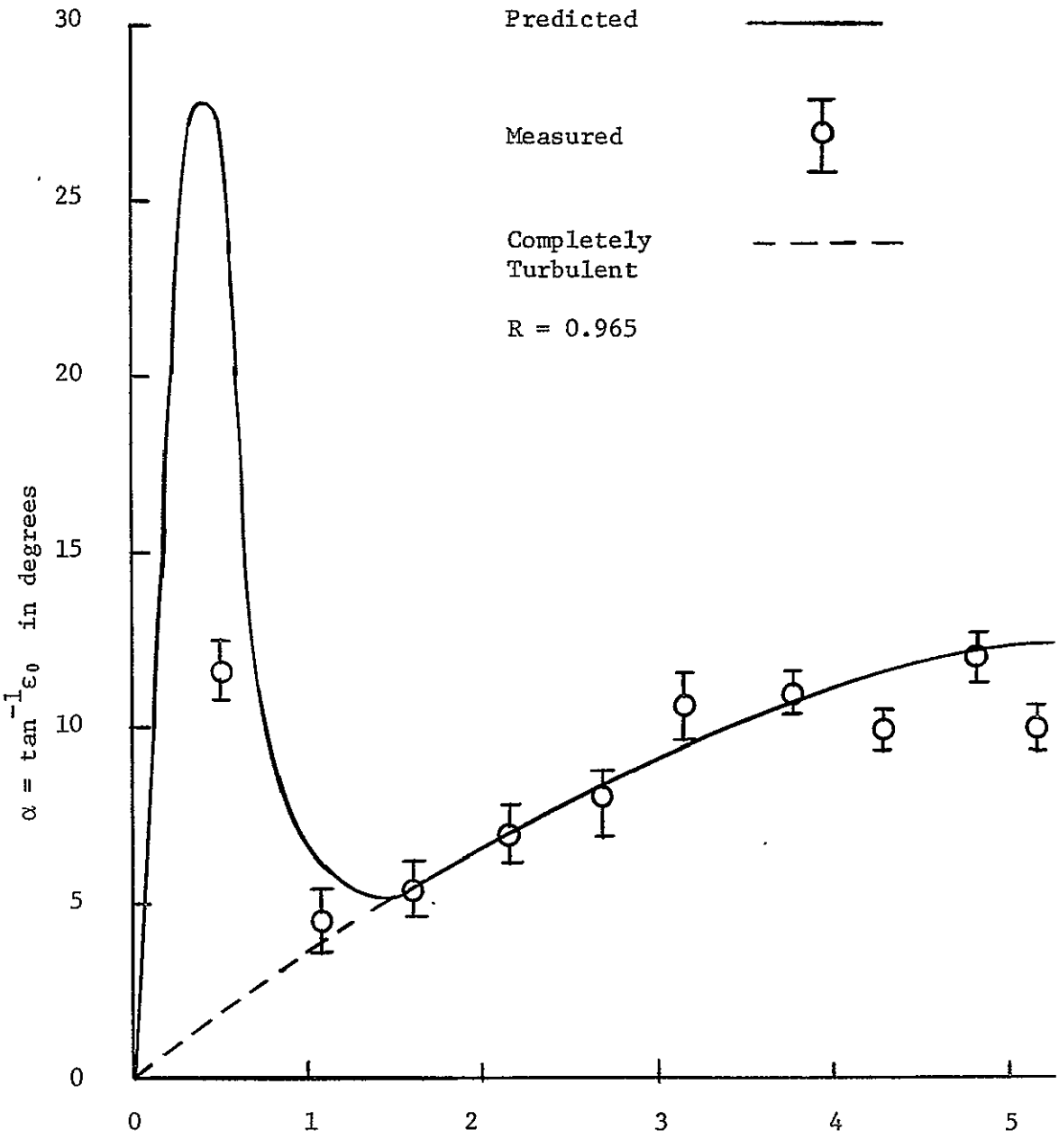

Figure 3-e: Variations of the Limiting streamline Angle ε_o with Θ

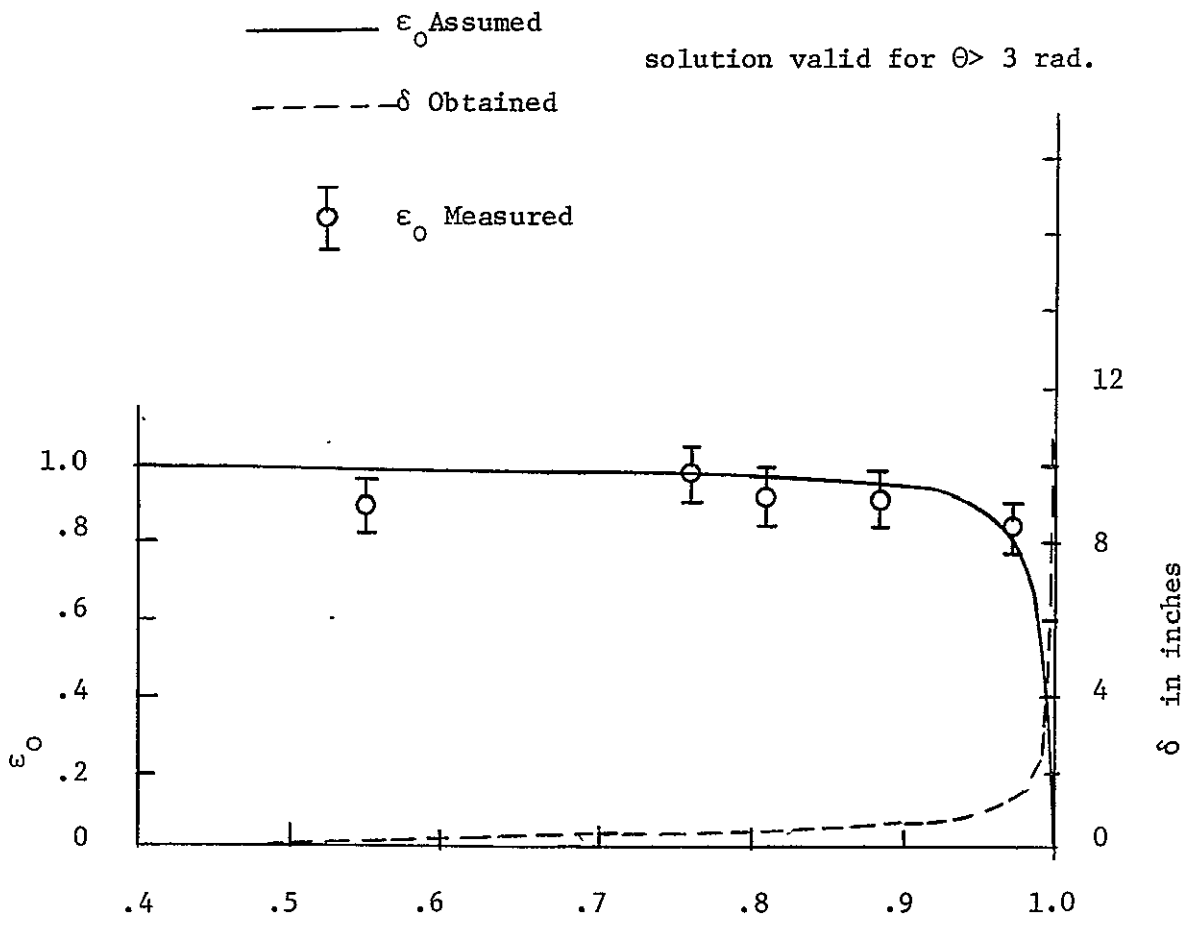

Figure 4: Asymptotic Solution of the θ-Momentum Equation

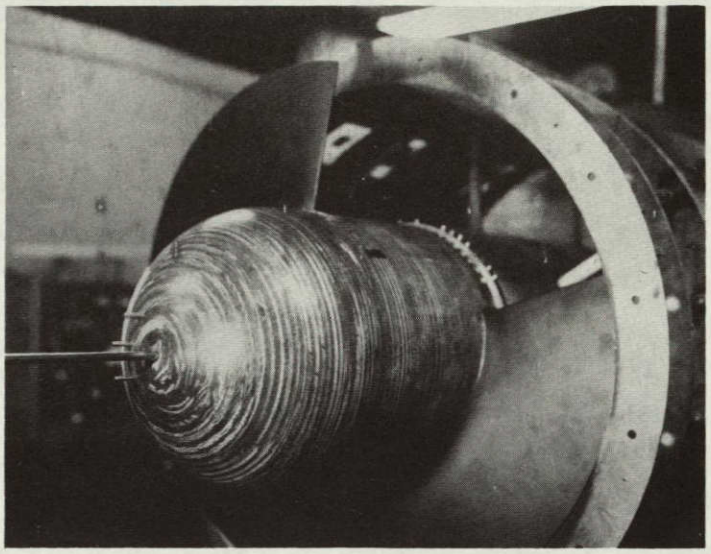

(a)

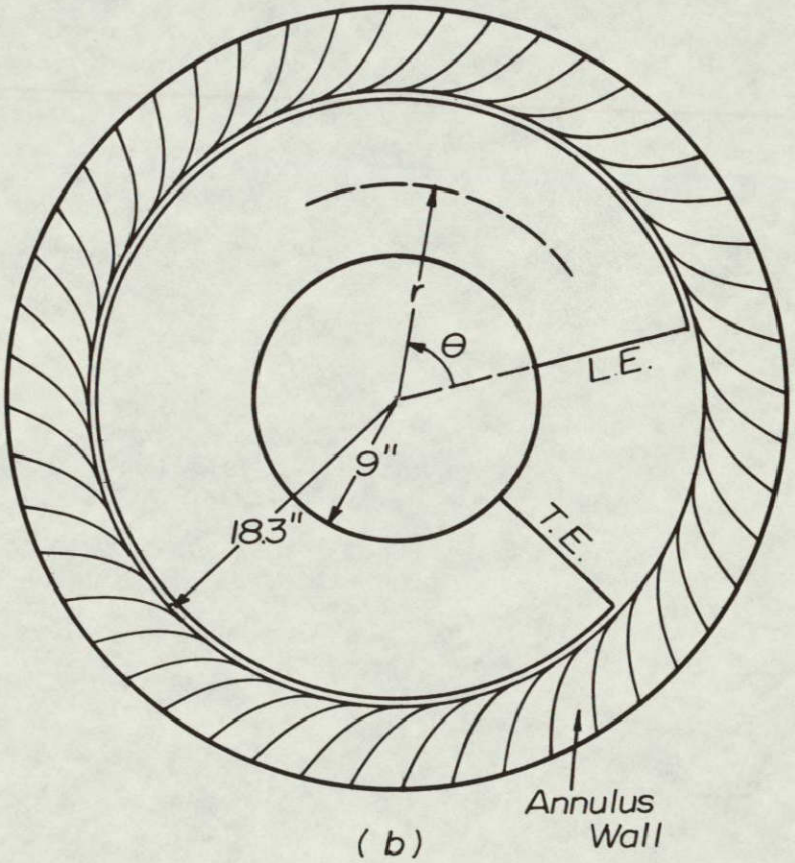

(b)

Figure 5: (a)- Photograph of the Blade with the annulus wall Removed
(b)- Schematic Diagram of the Blade

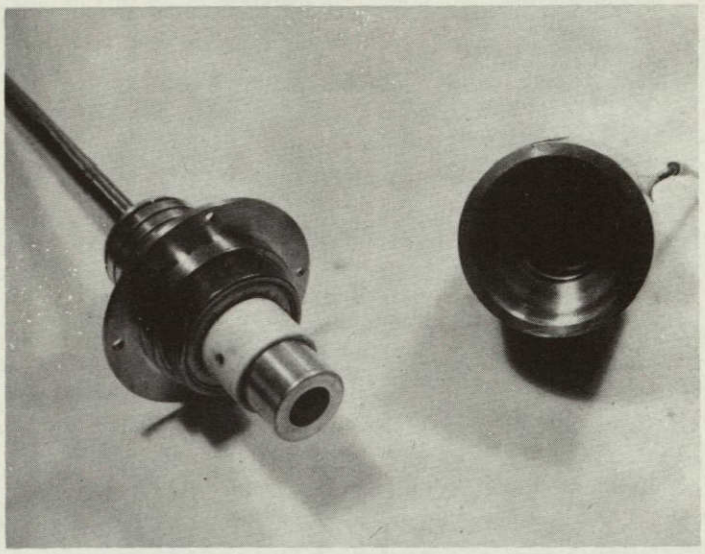

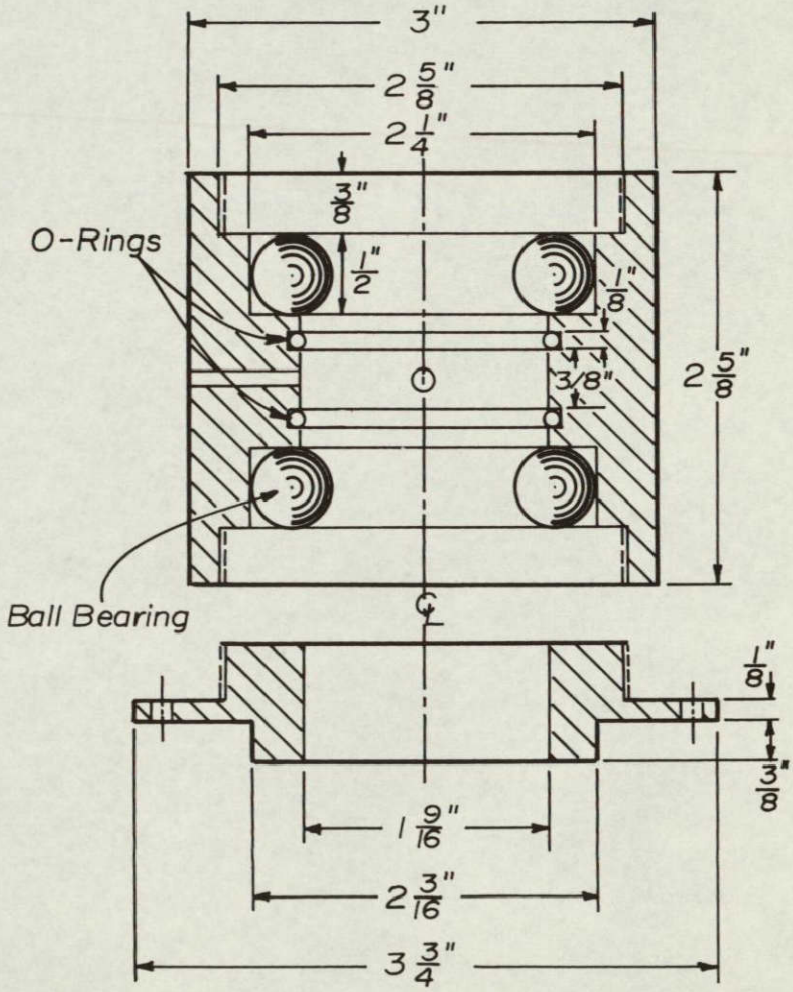

Figure 6: One Channel Pressure Transfer Device

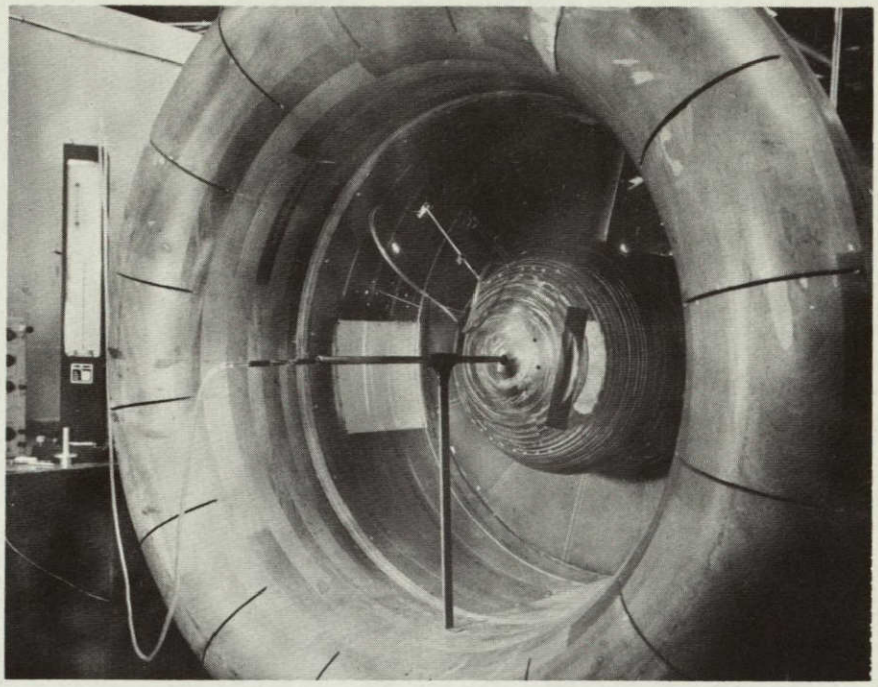

NOT REPRODUCIBLE

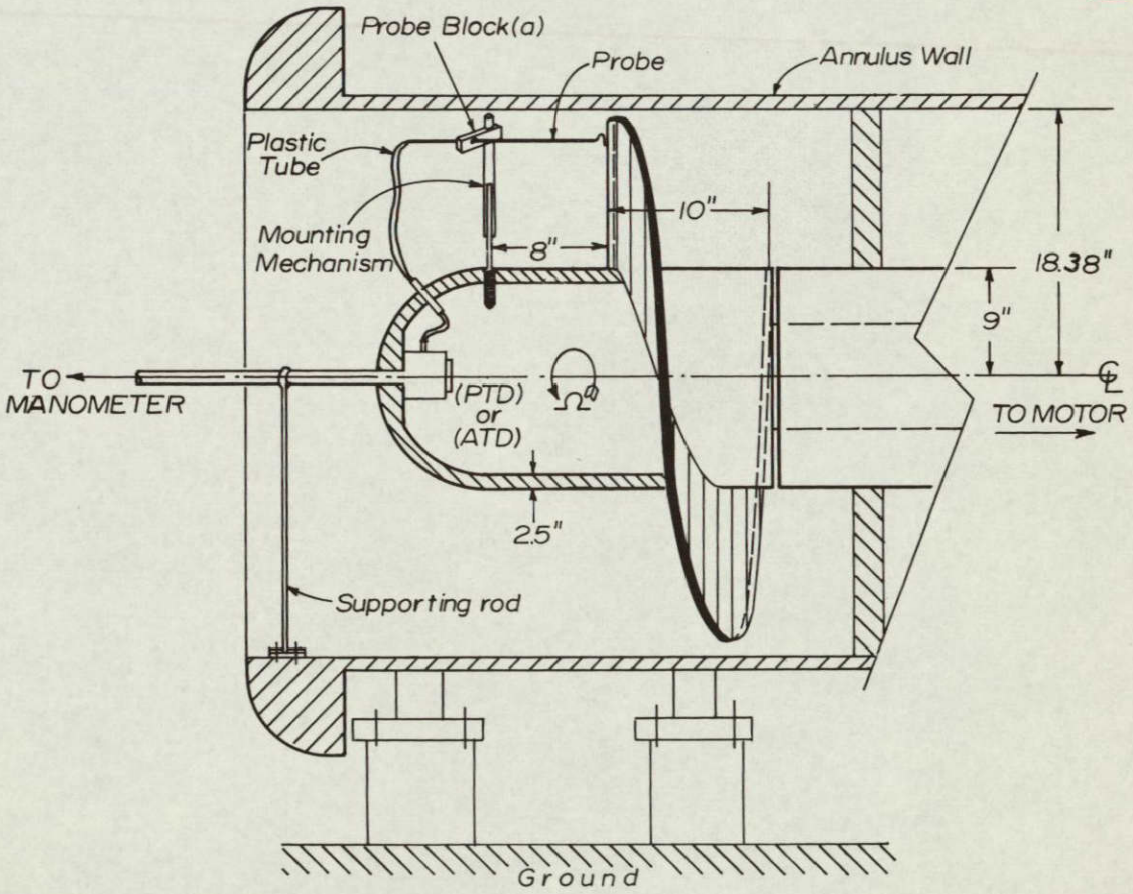

Figure 7: Photograph and the Schematic Diagram of the Test Assembly

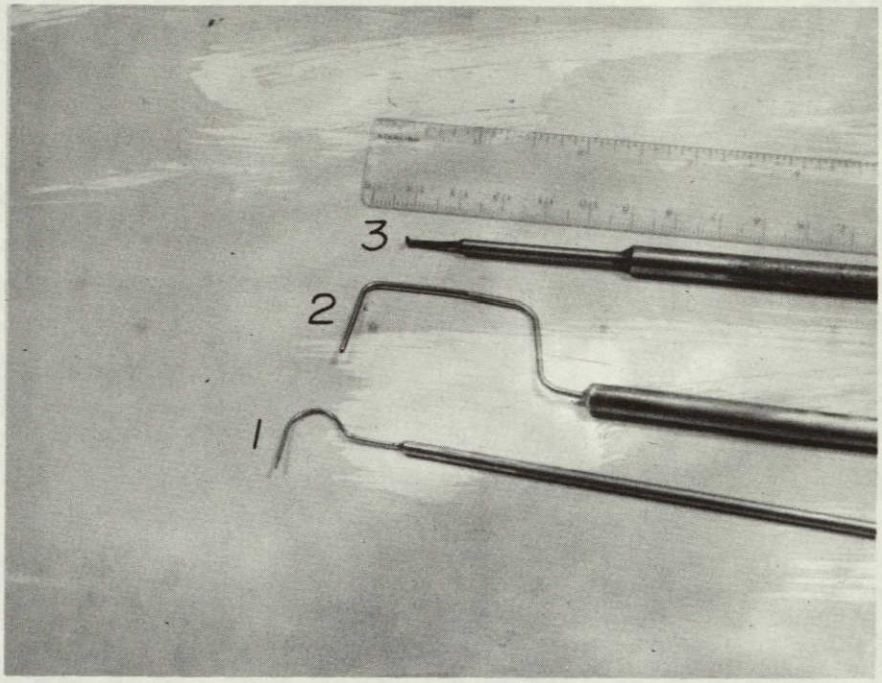

1- Boundary-Layer Probe:

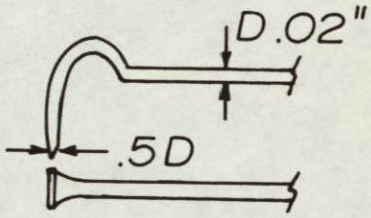

2- Preston Tube:

1/16 O.D.

3- Two-hole Yaw-meter Probe:

0.04 inch O.D. of each hole

Figure 8: Photograph and the Dimensions of the Probes

NOT REPRODUCIBLE

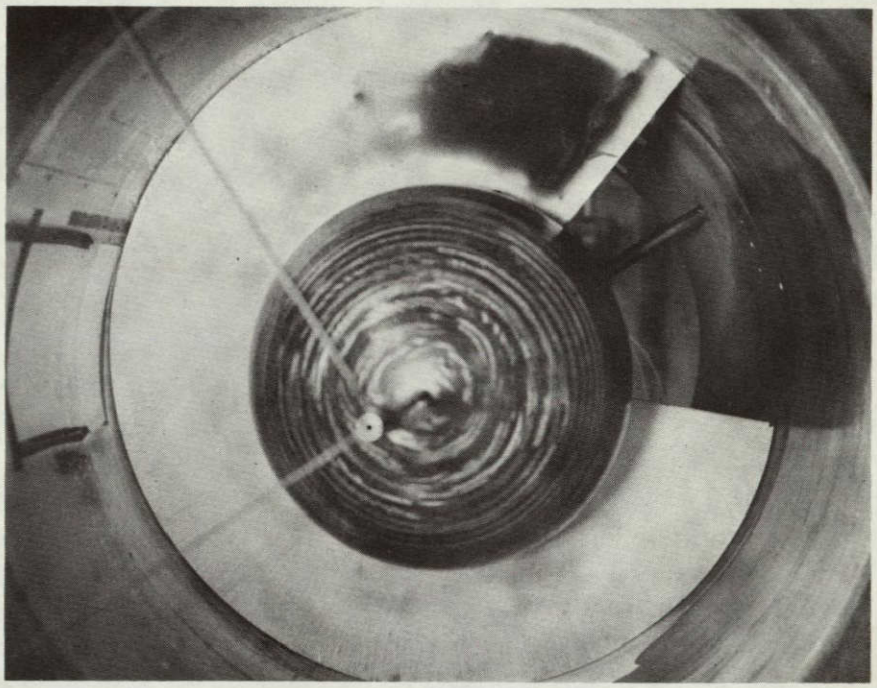

Figure 9: Visualization of the Location of Flow Transition Zone

NOT REPRODUCIBLE

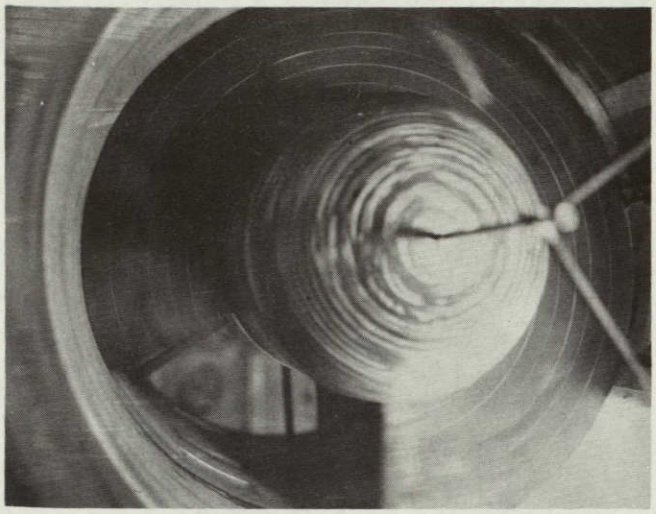

(a)

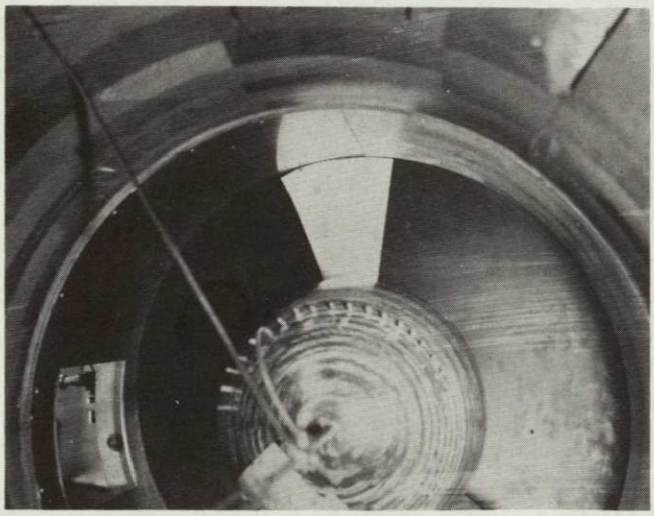

(b)

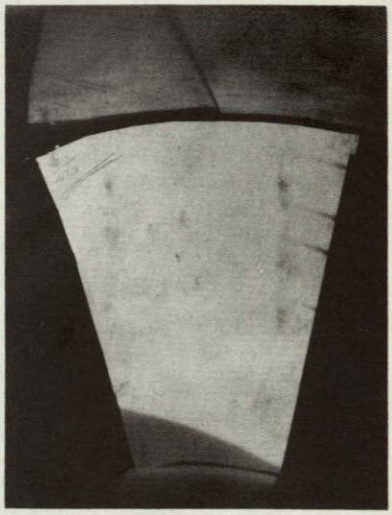

(c)

Figure 10: (a)- Smoke Filament Method of Visualizing the Limiting Streamline
(b)- Ammonia Streak Technique of Visualizing the Limiting Streamline
(c)- Photograph of the Streamlines

NOT REPRODUCIBLE

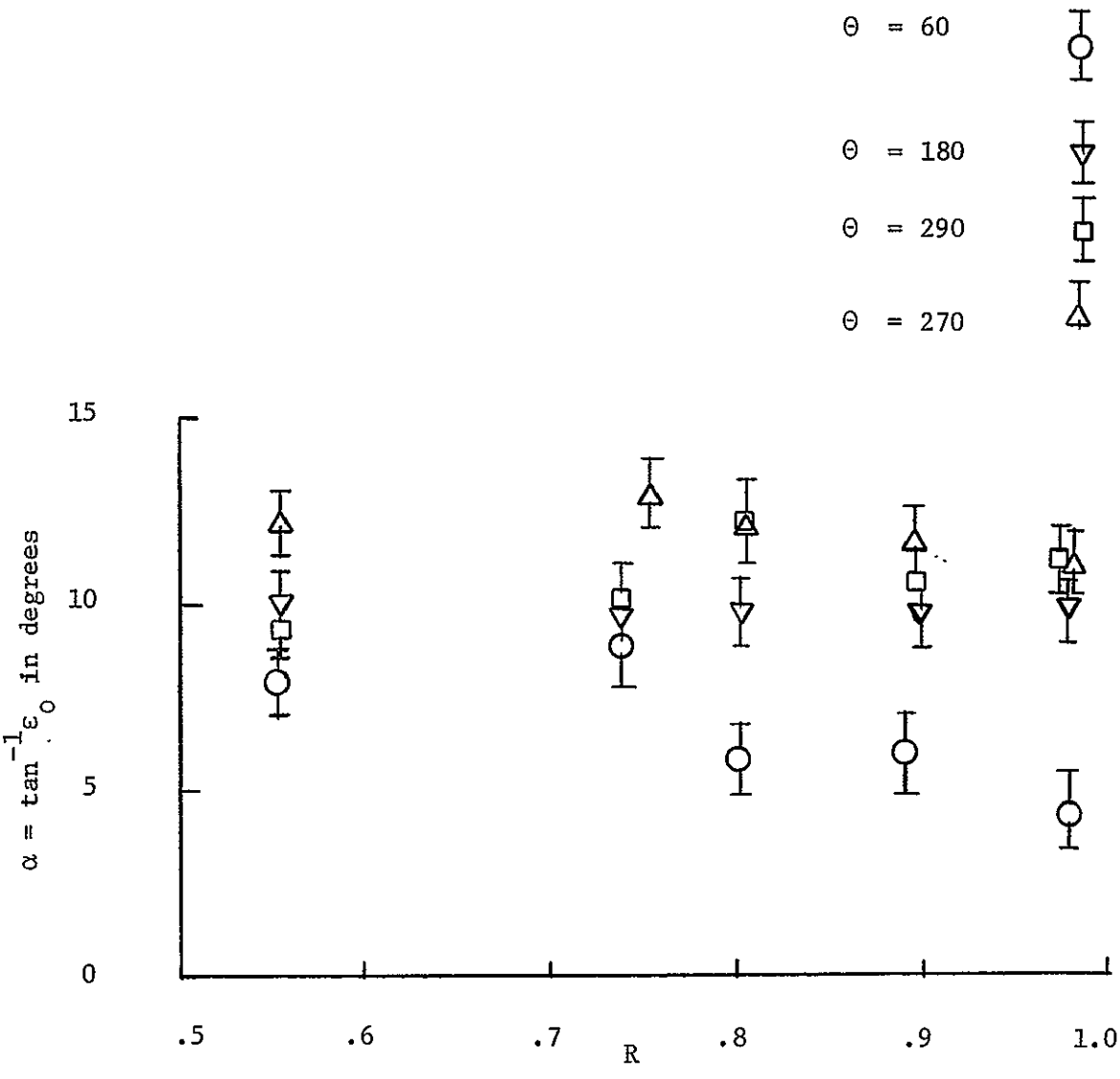

Figure 11: Radial Variations of the Limiting Streamline Angle

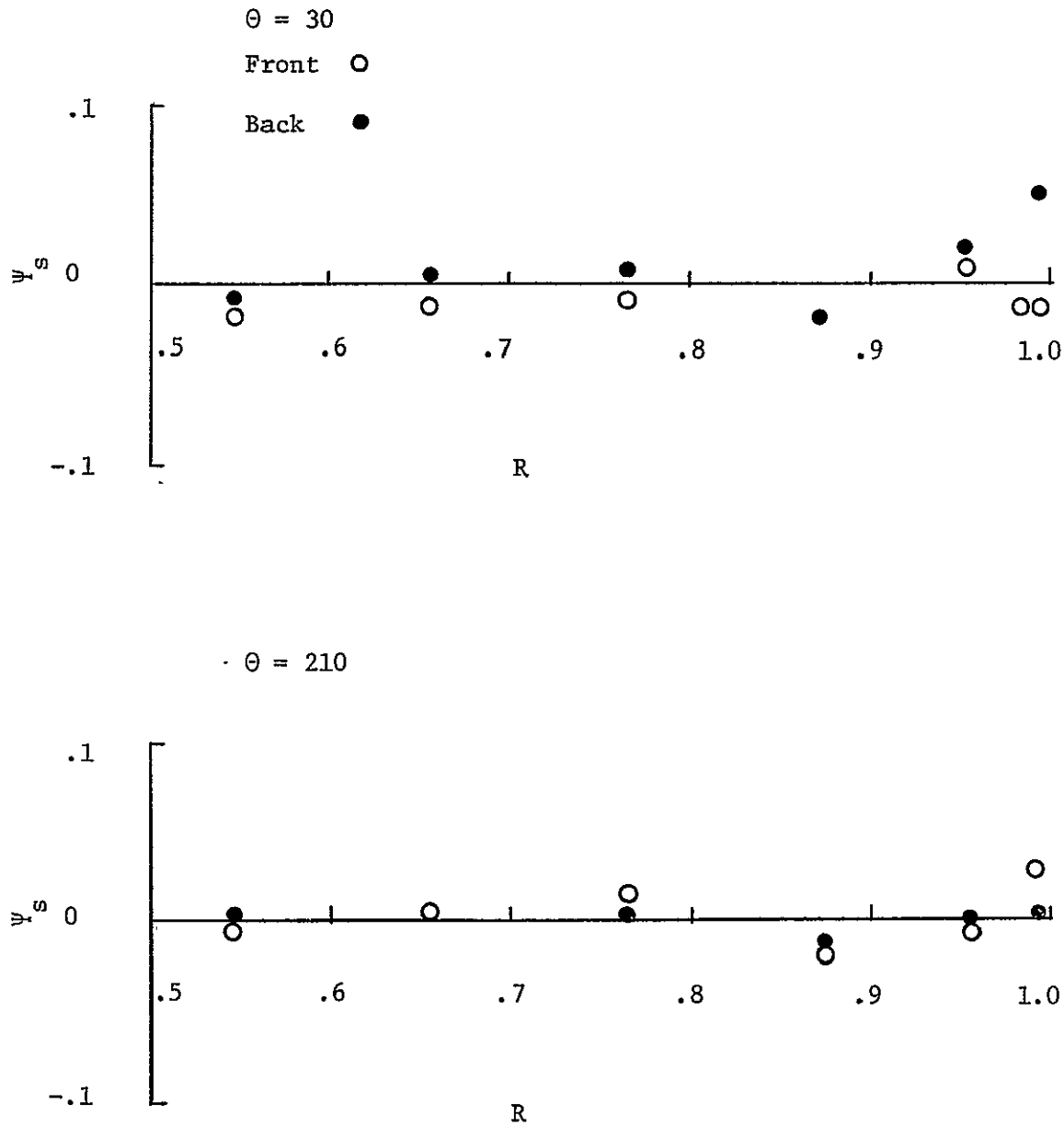

Figure 12: Blade Static Pressure

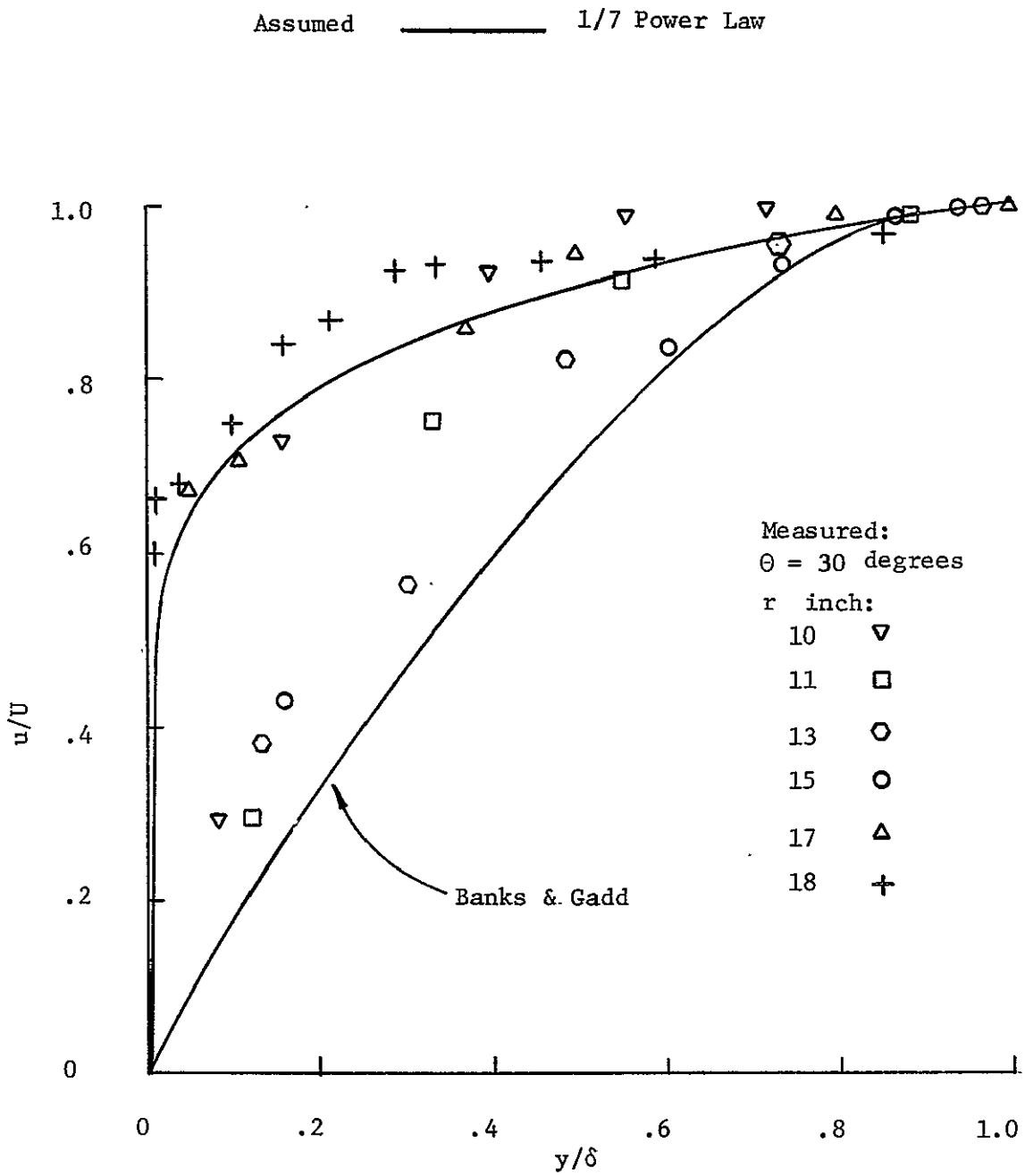

Figure 13-a: Tangential Velocity Profiles

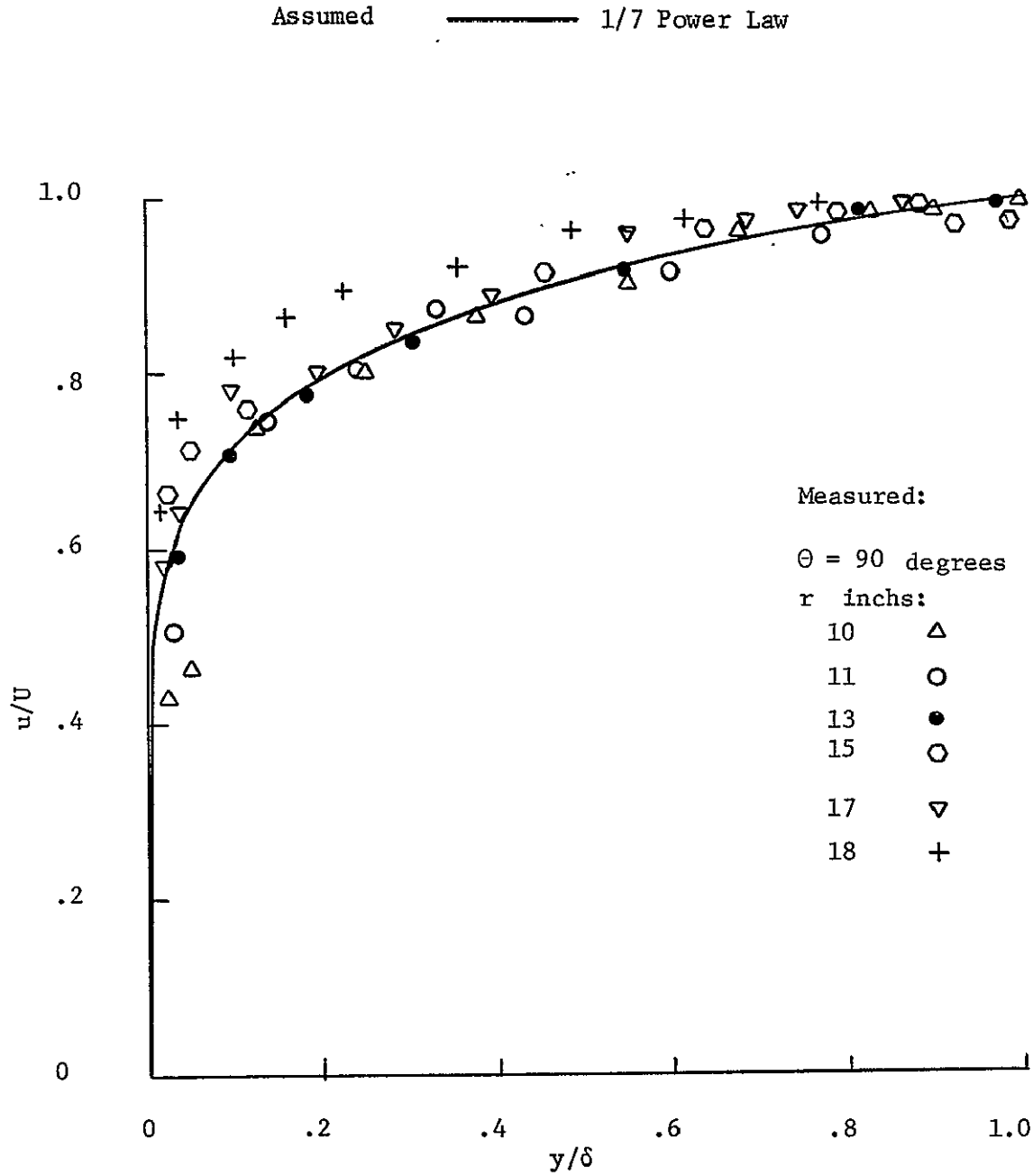

Figure 13-b: Tangential Velocity Profiles

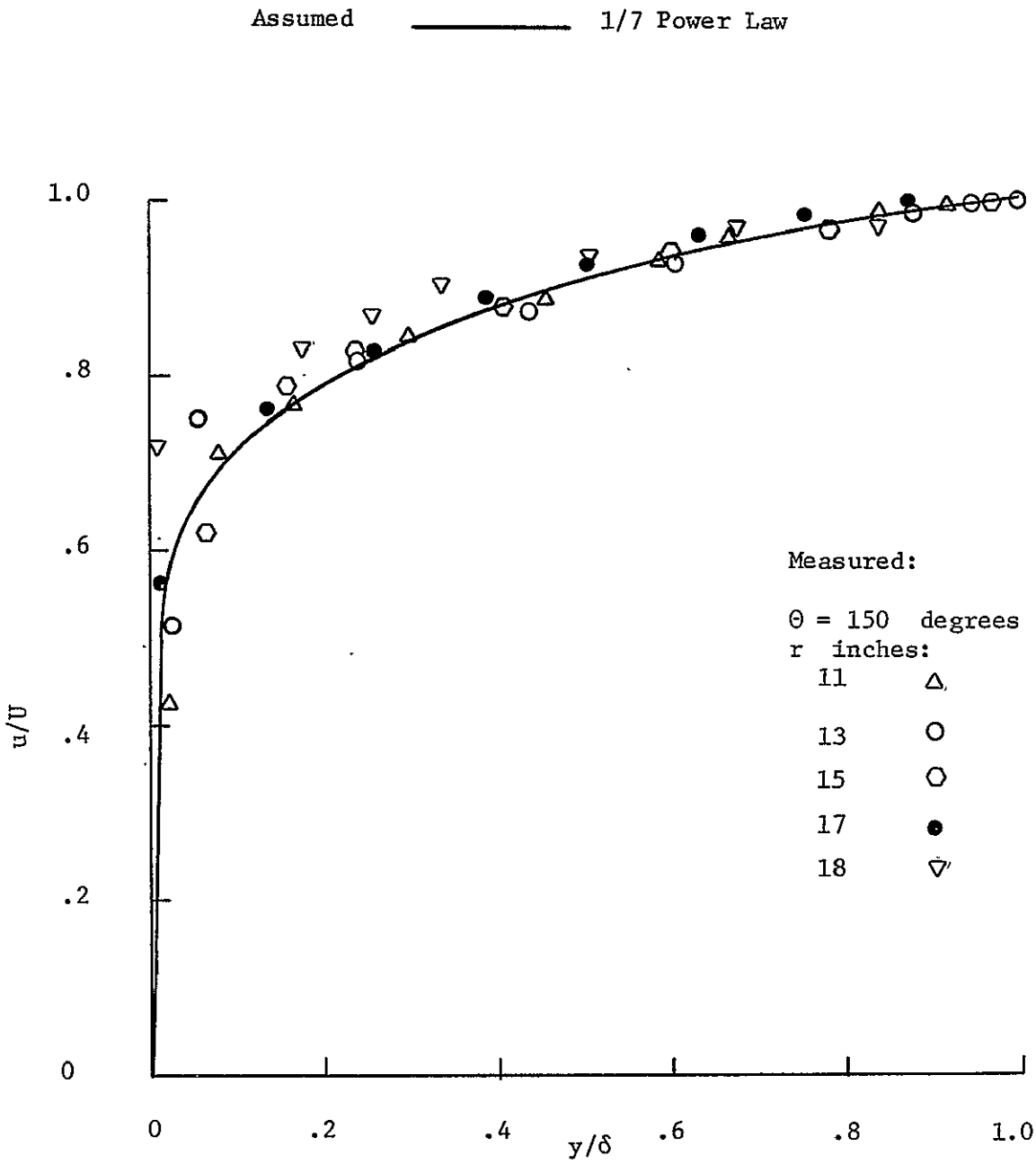

Figure 13-c: Tangential Velocity Profiles

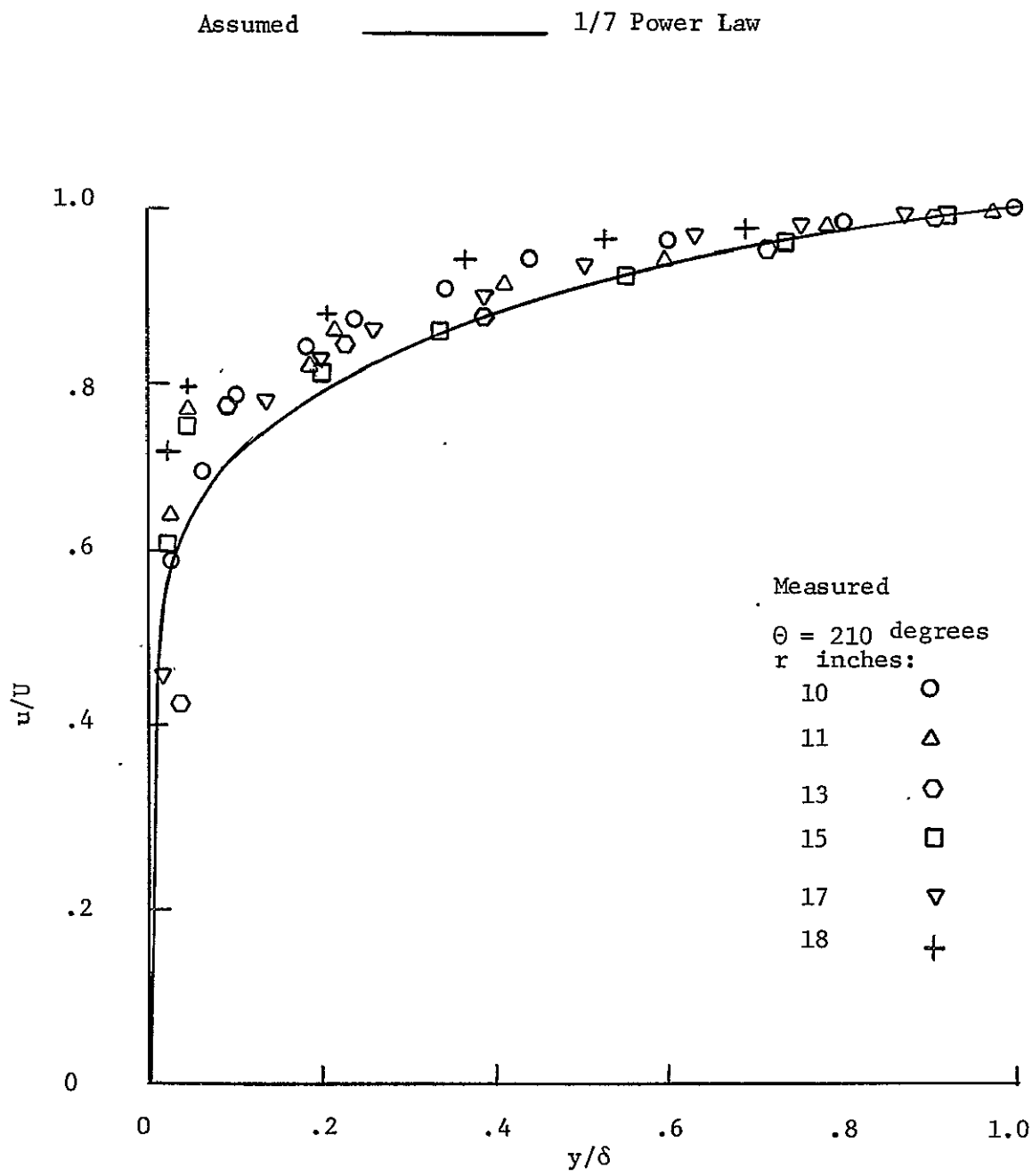

Figure 13-d: Tangential Velocity Profiles

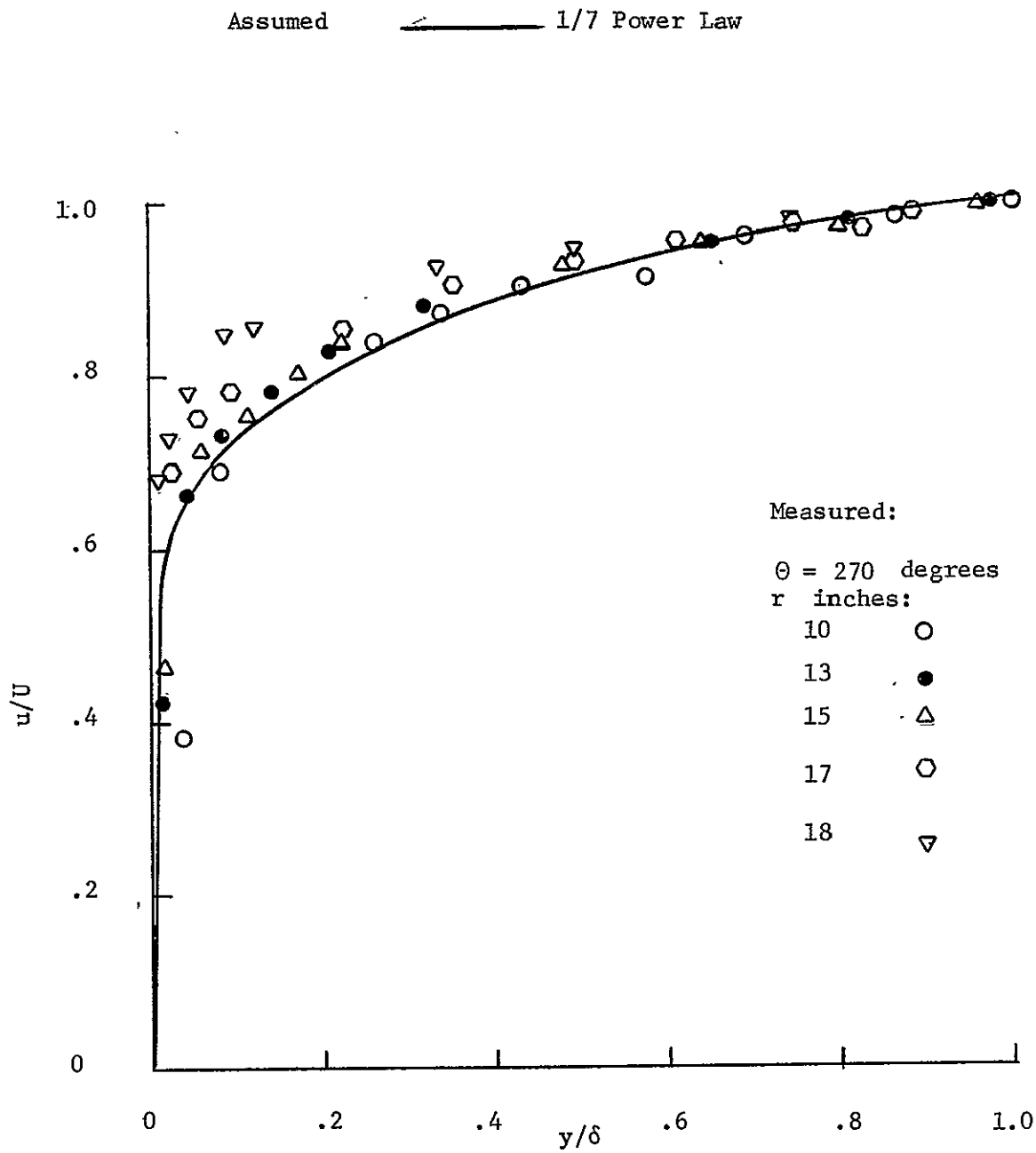

Figure 13-e: Tangential Velocity Profiles

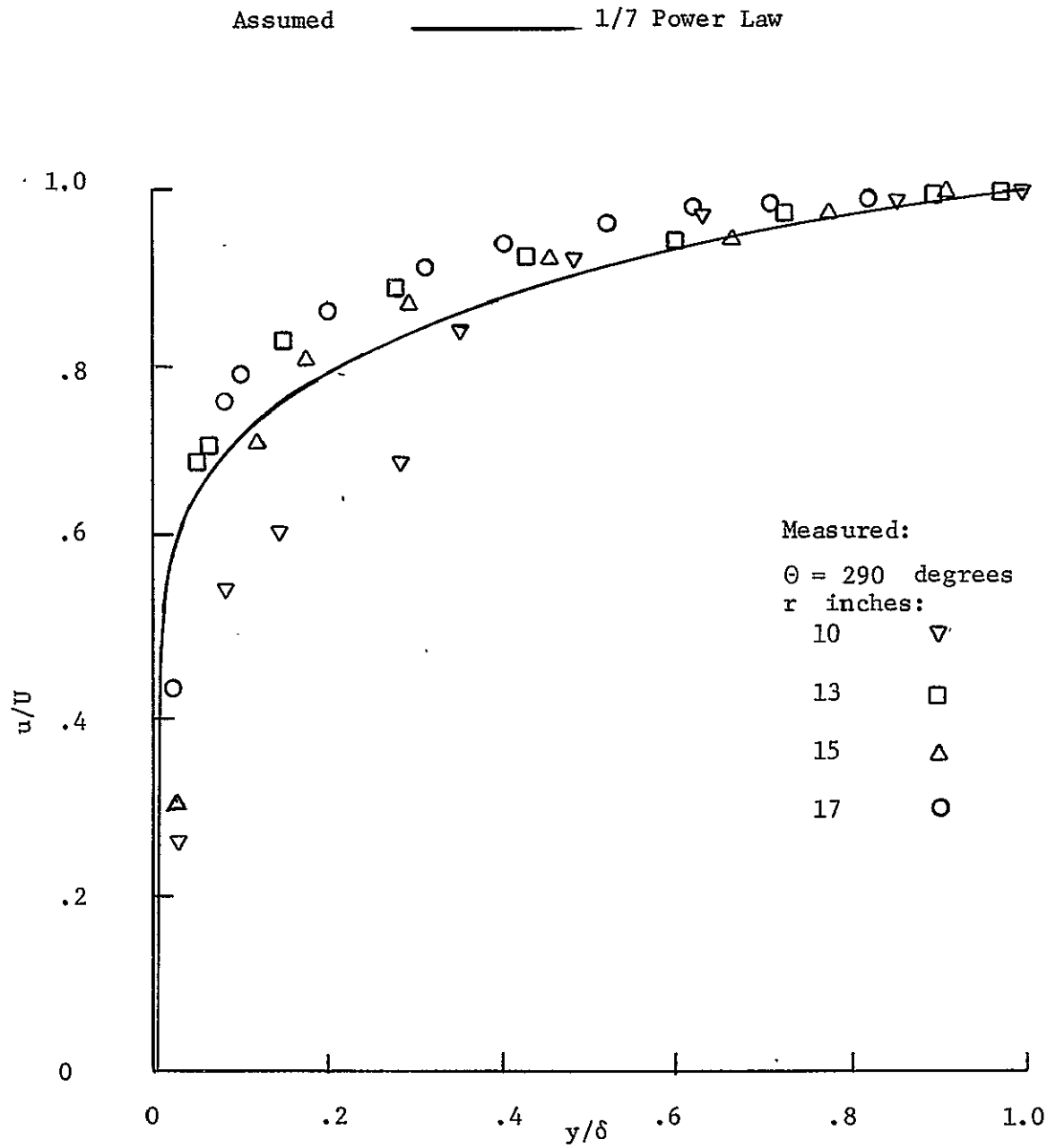

Figure 13-f: Tangential Velocity Profiles

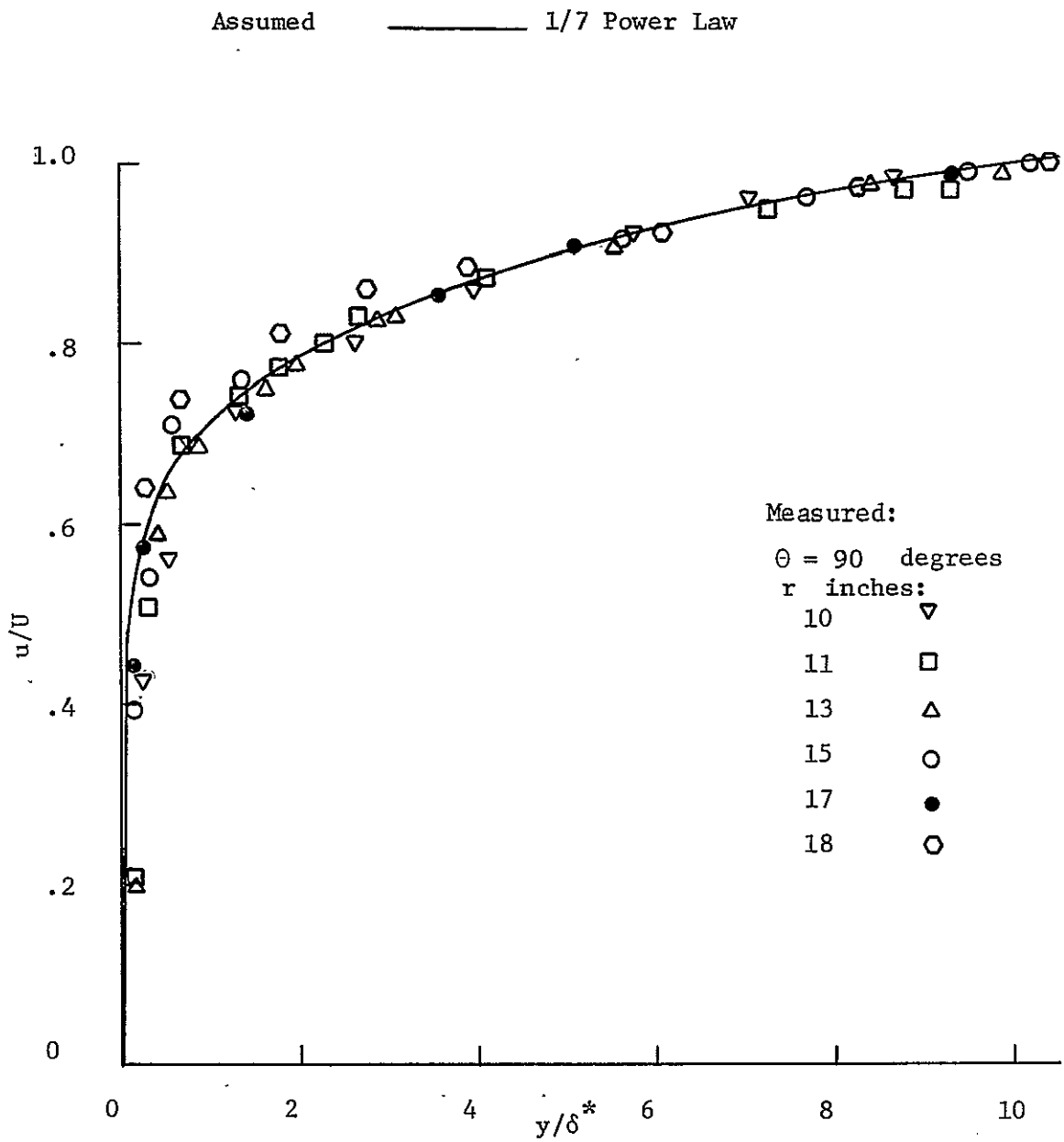

Figure 14-a: Tangential Velocity Profiles

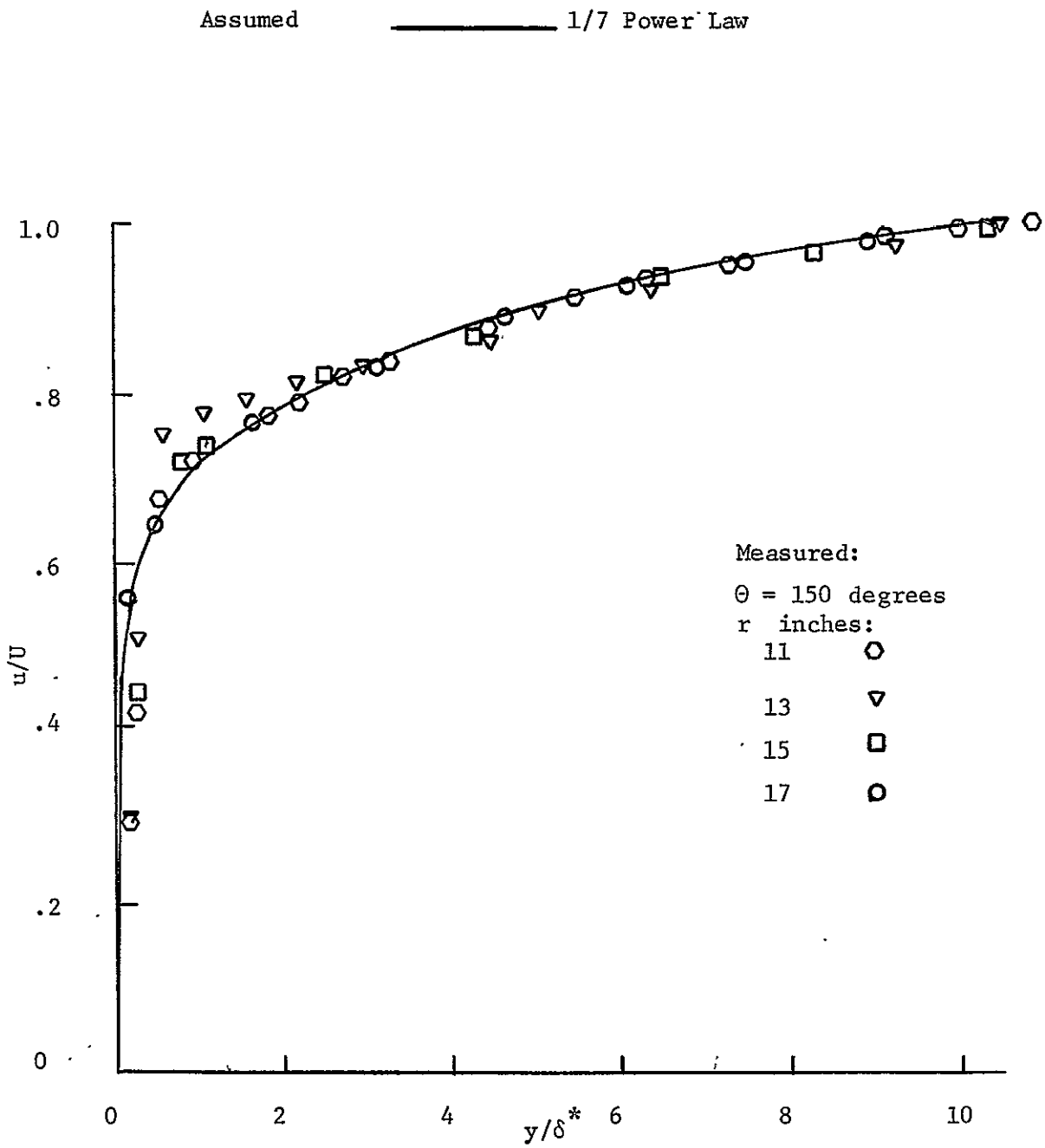

Figure 14-b: Tangential Velocity Profiles

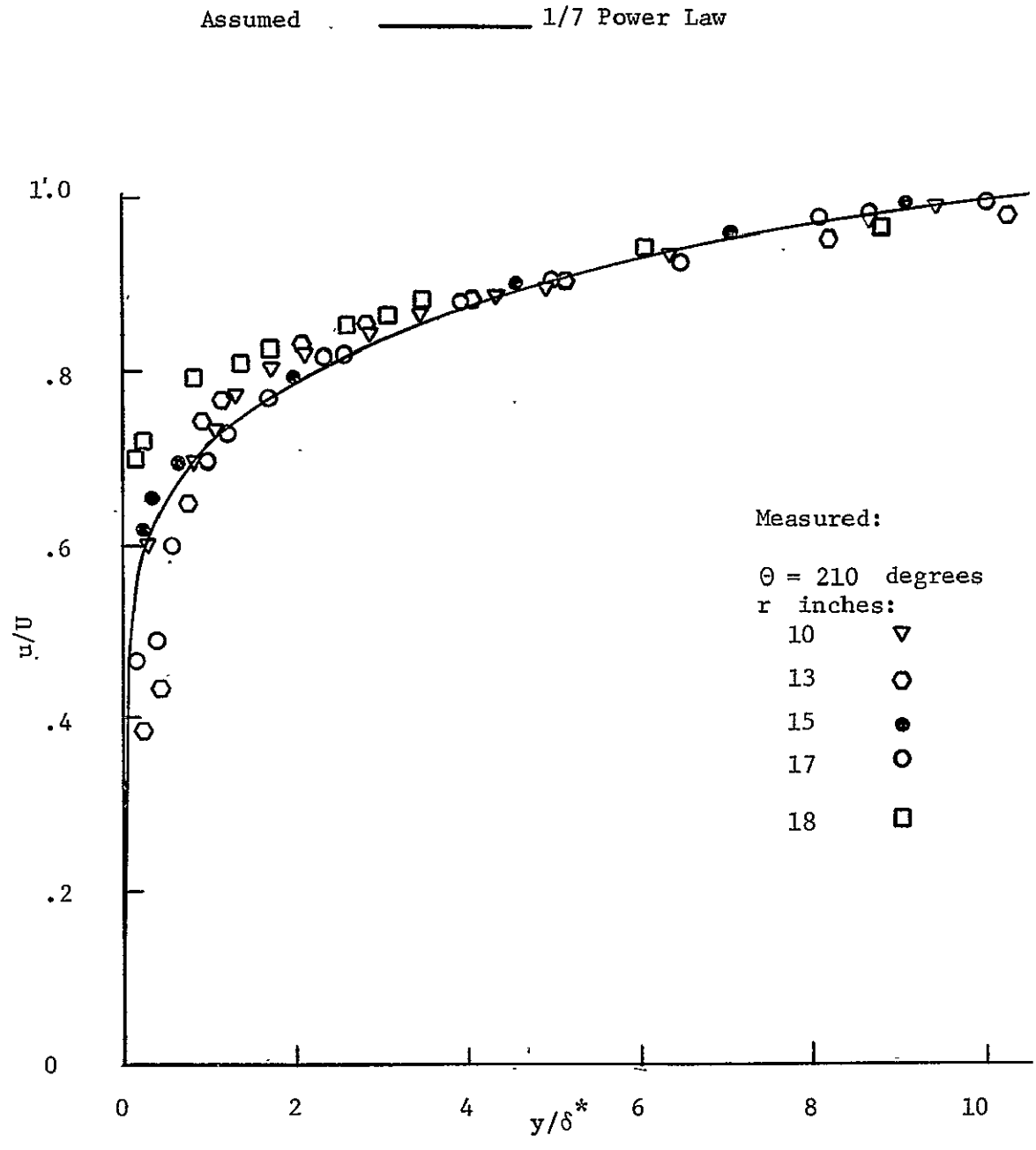

Figure 14-c:. Tangential Velocity Profiles

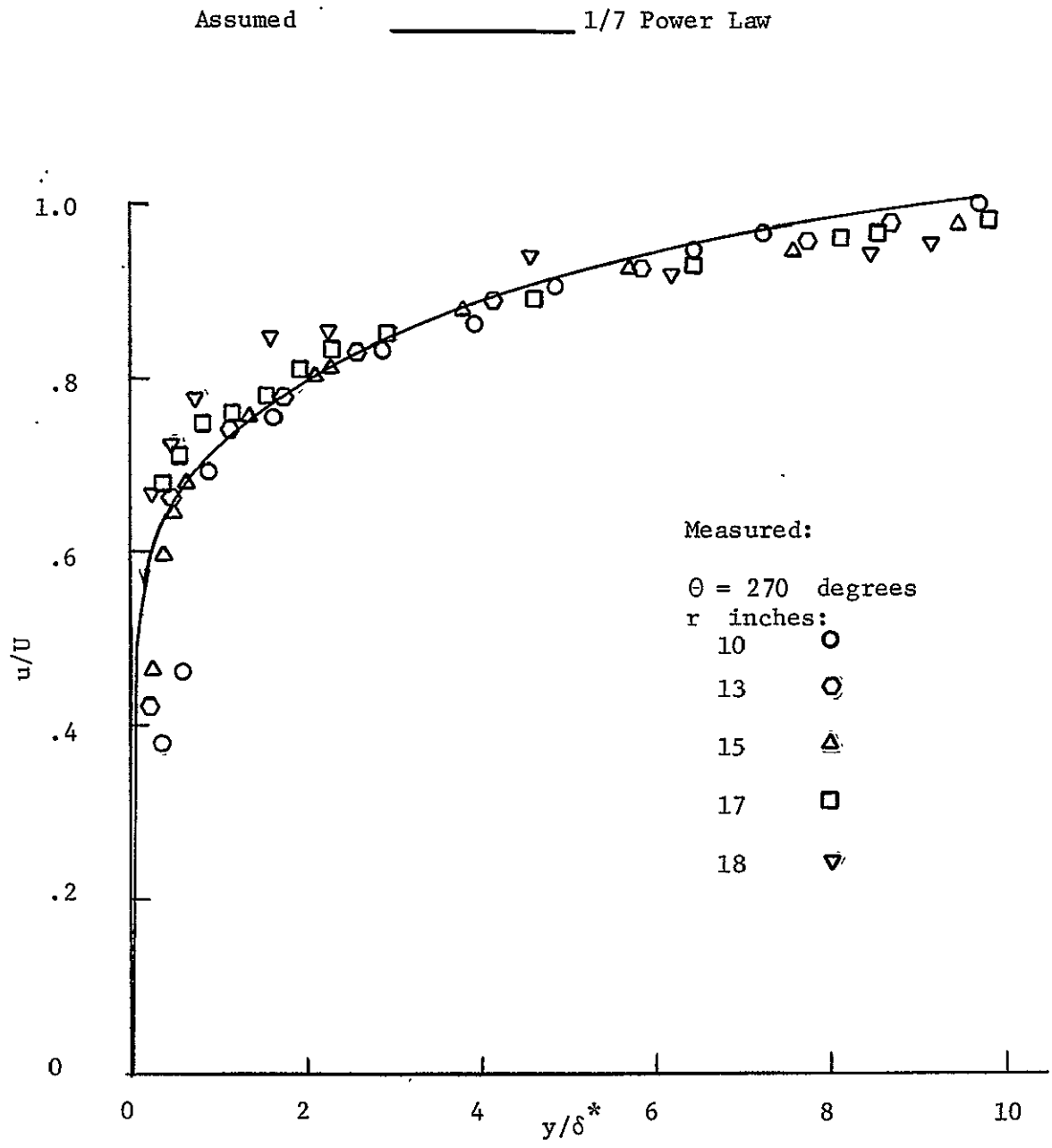

Figure 14-d: Tangential Velocity Profiles

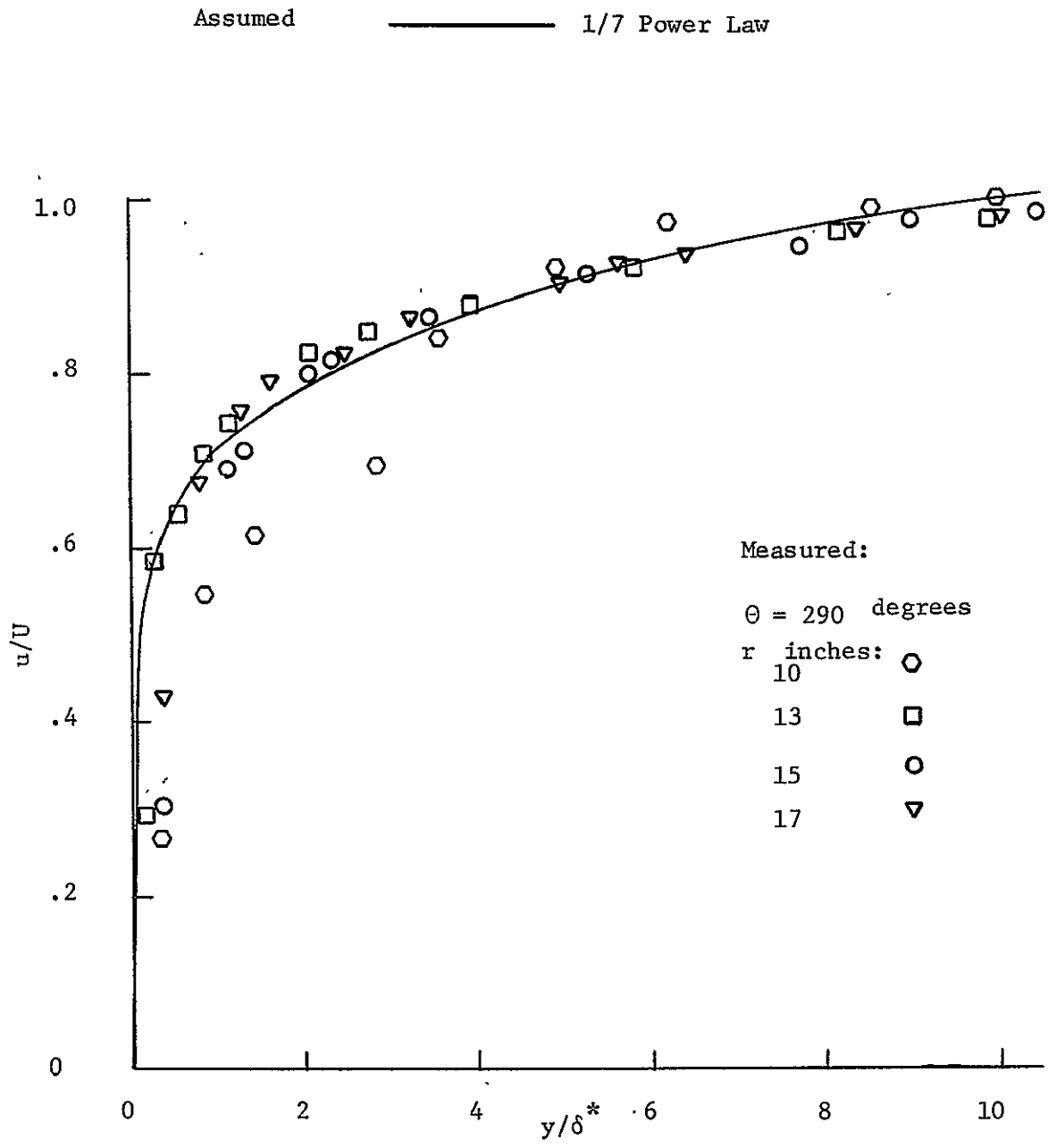

Figure 14-e: Tangential Velocity Profiles

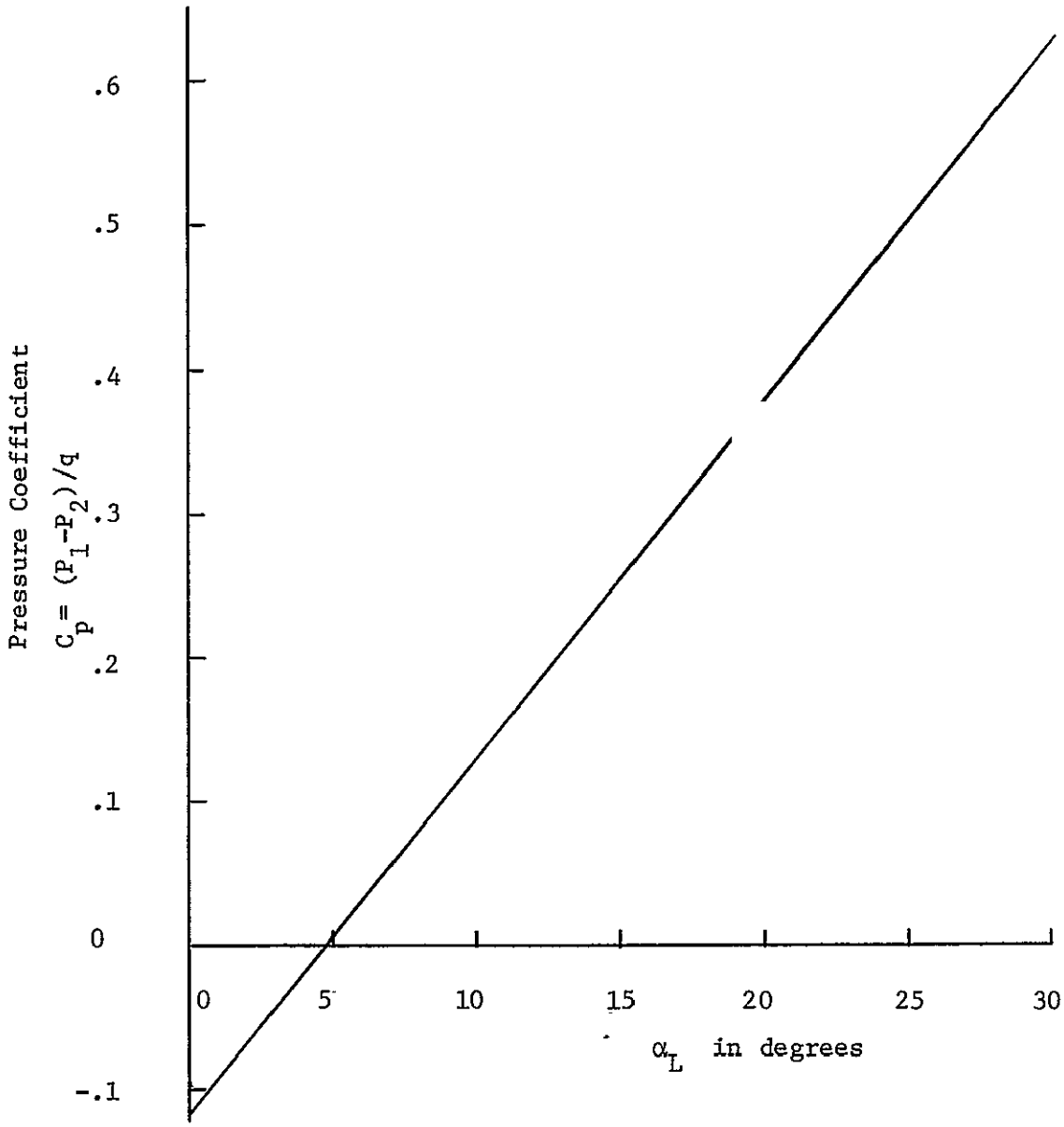

Figure 15: Calibration Curve of the Two-Hole Yaw Meter Probe

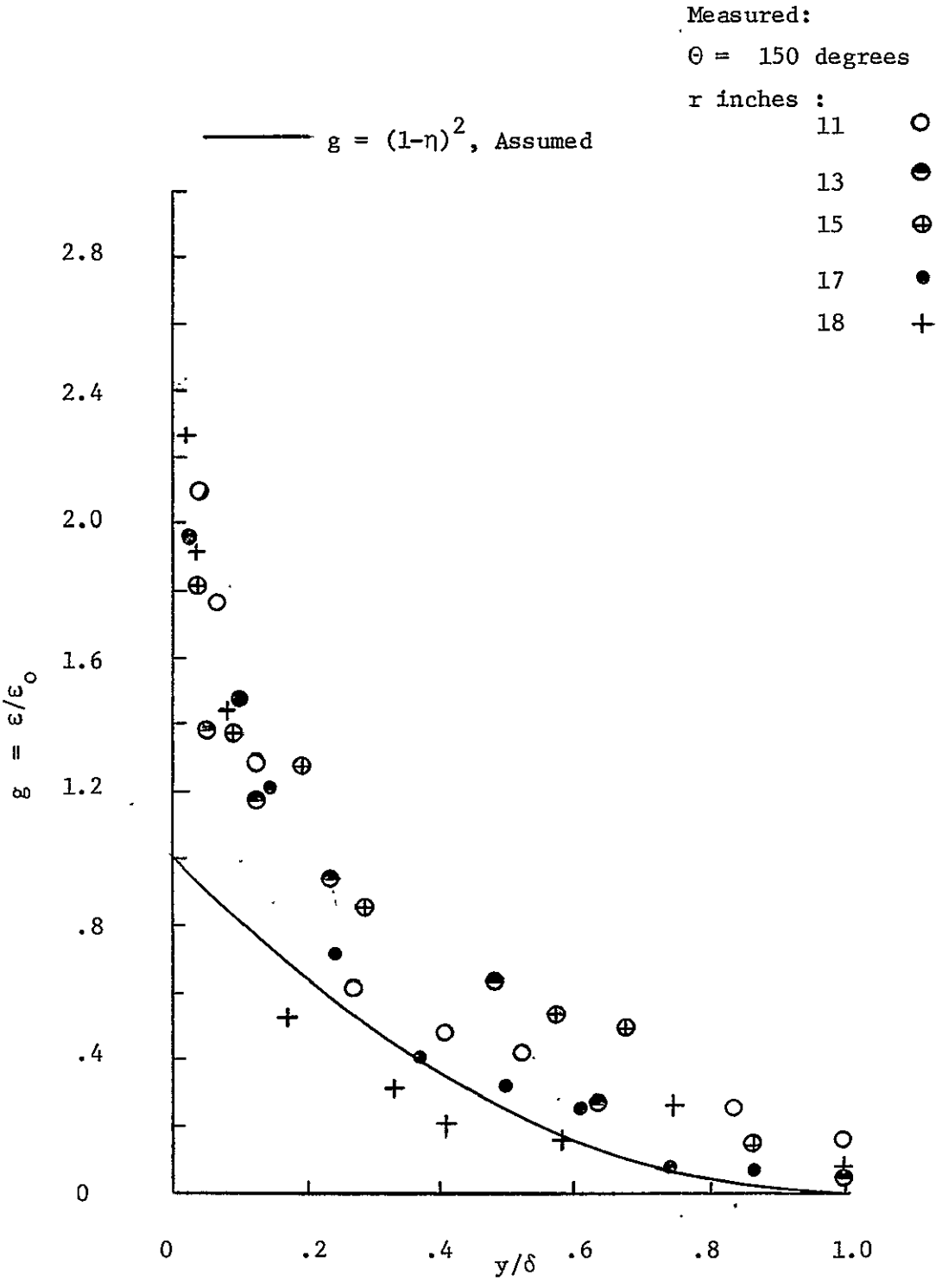

Figure 16-a: Comparison Between the Assumed and Experimental Radial Velocity Profiles.

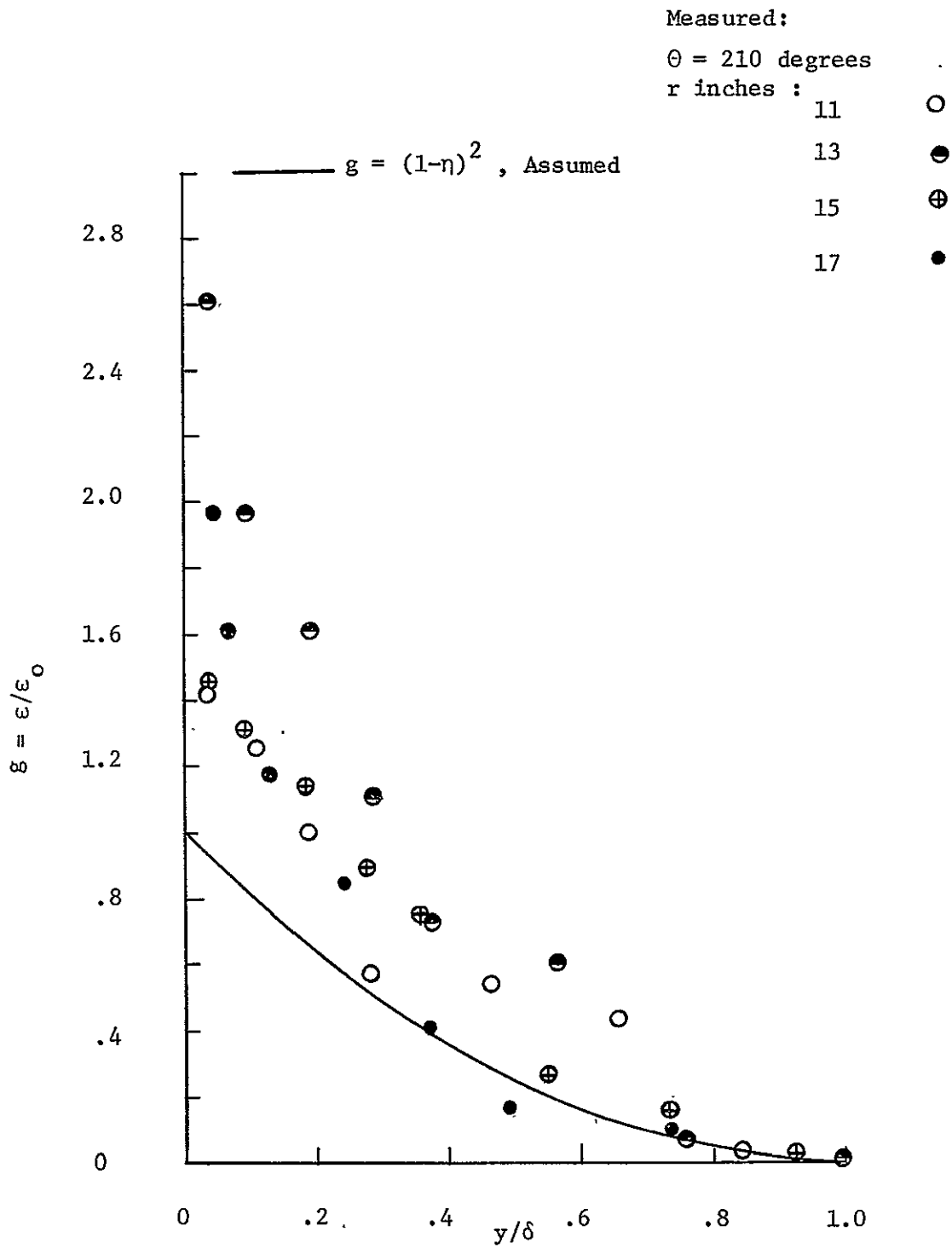

Figure 16-b: Comparison Between the Assumed and Experimental Radial Velocity Profiles

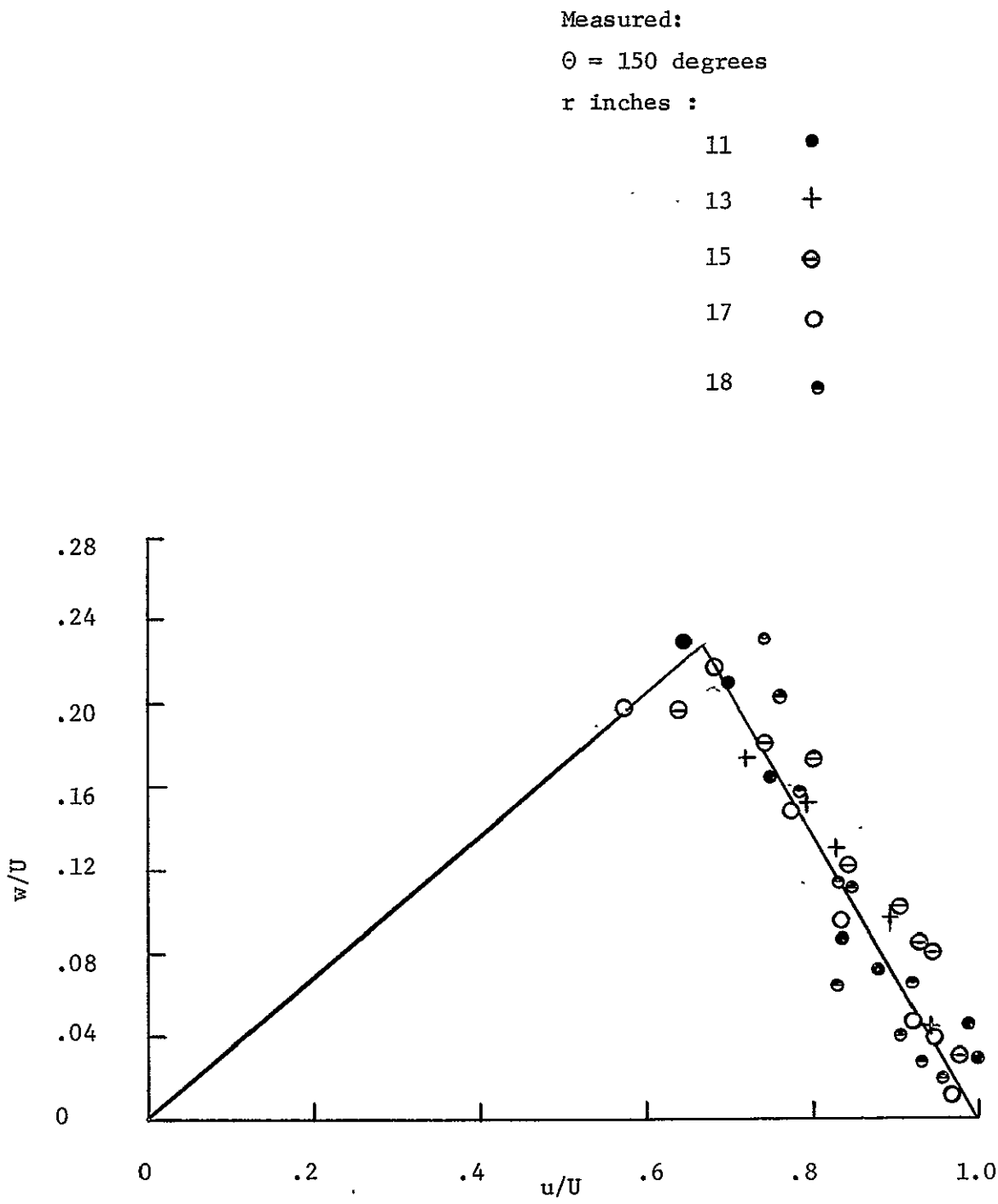

Figure 17-a: Triangular Plot of the Radial Velocity Profiles

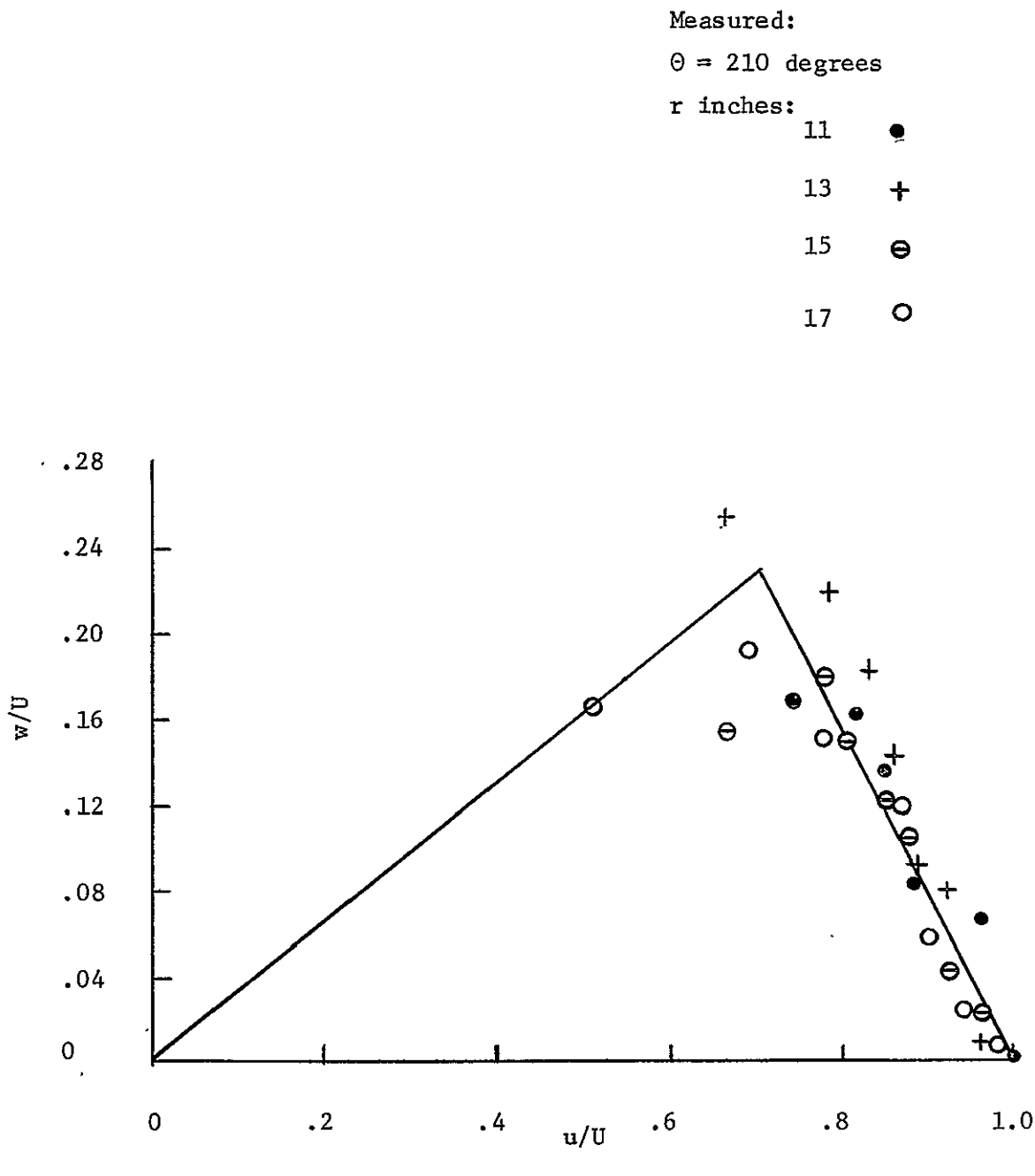

Figure 17-b: Triangular Plot of the Radial Velocity Profiles

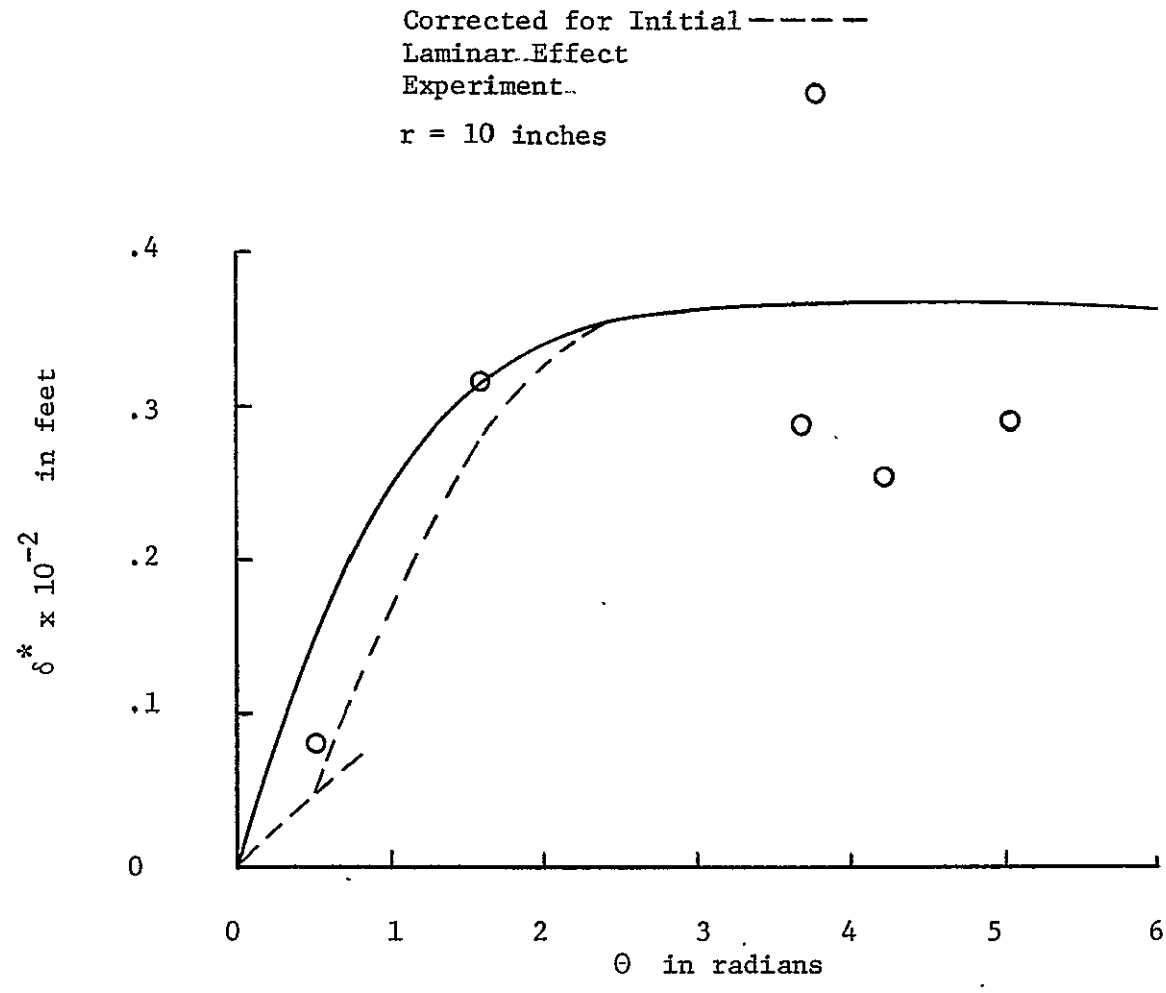

Figure 18-a: Tangential Variations of the Momentum Thickness

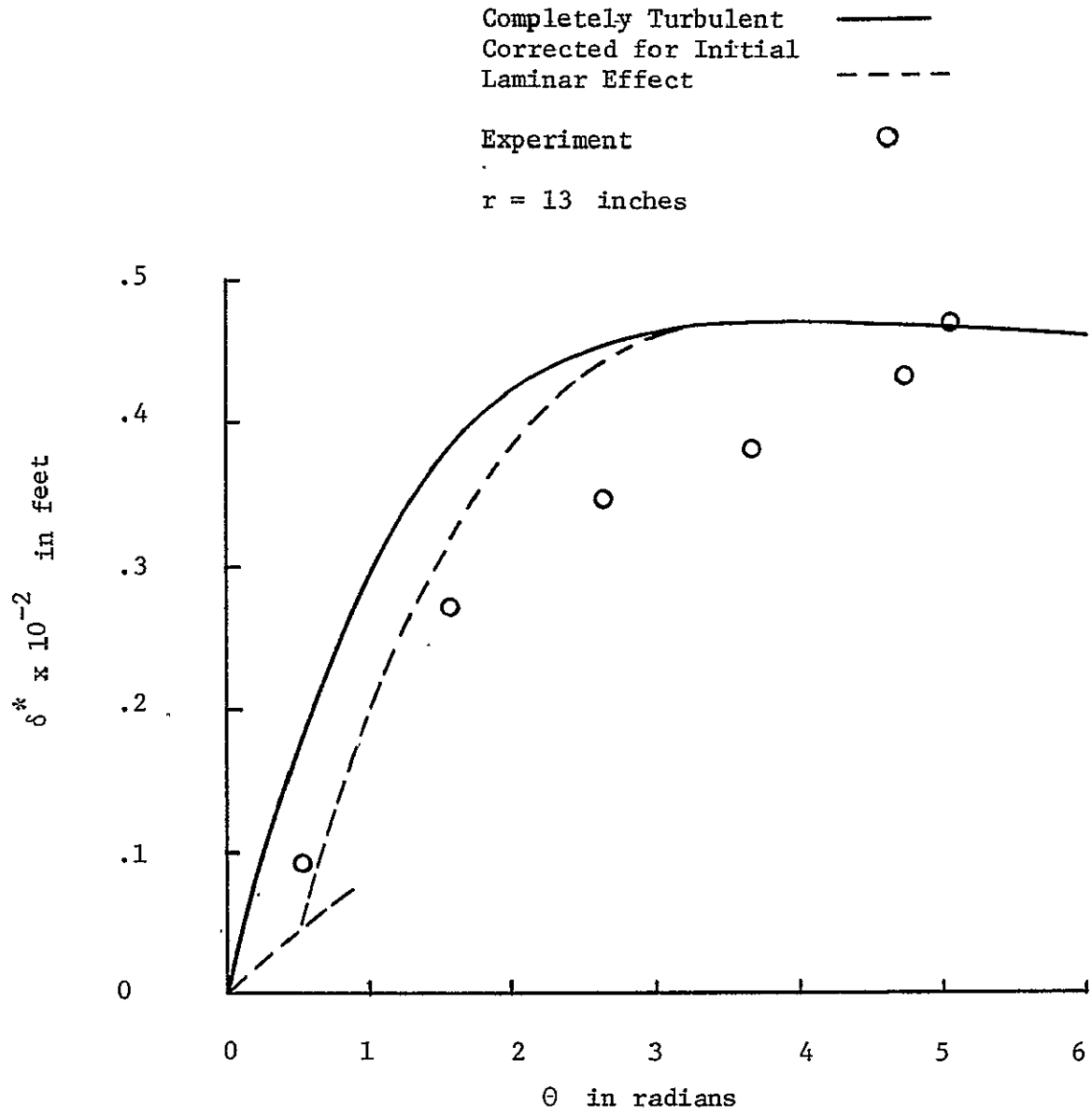

Figure 18-b: Tangential Variations of the Momentum Thickness

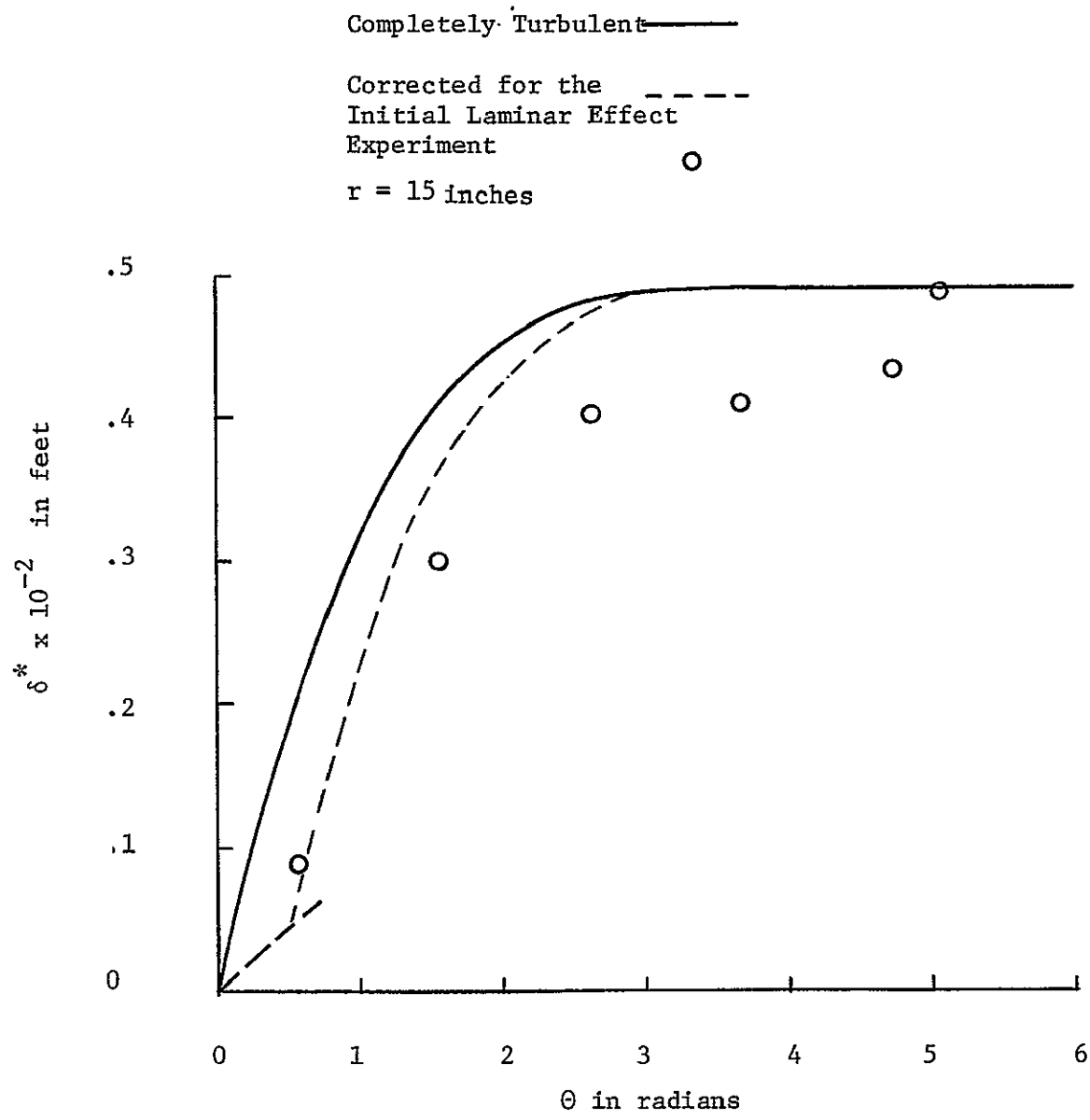

Figure 18-c: Tangential Variations of the Momentum Thickness

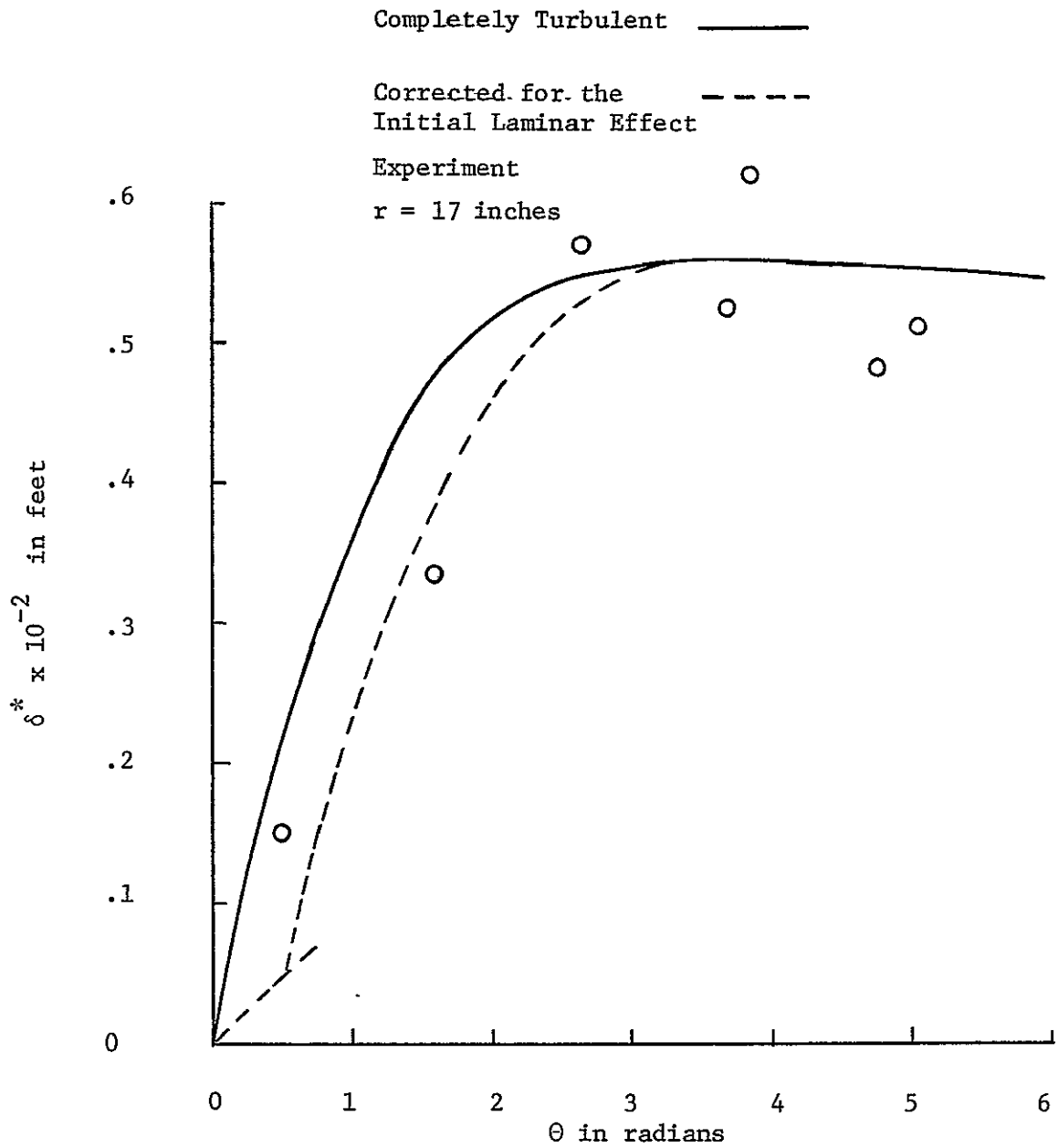

Figure 18-d: Tangential Variations of the Momentum Thickness

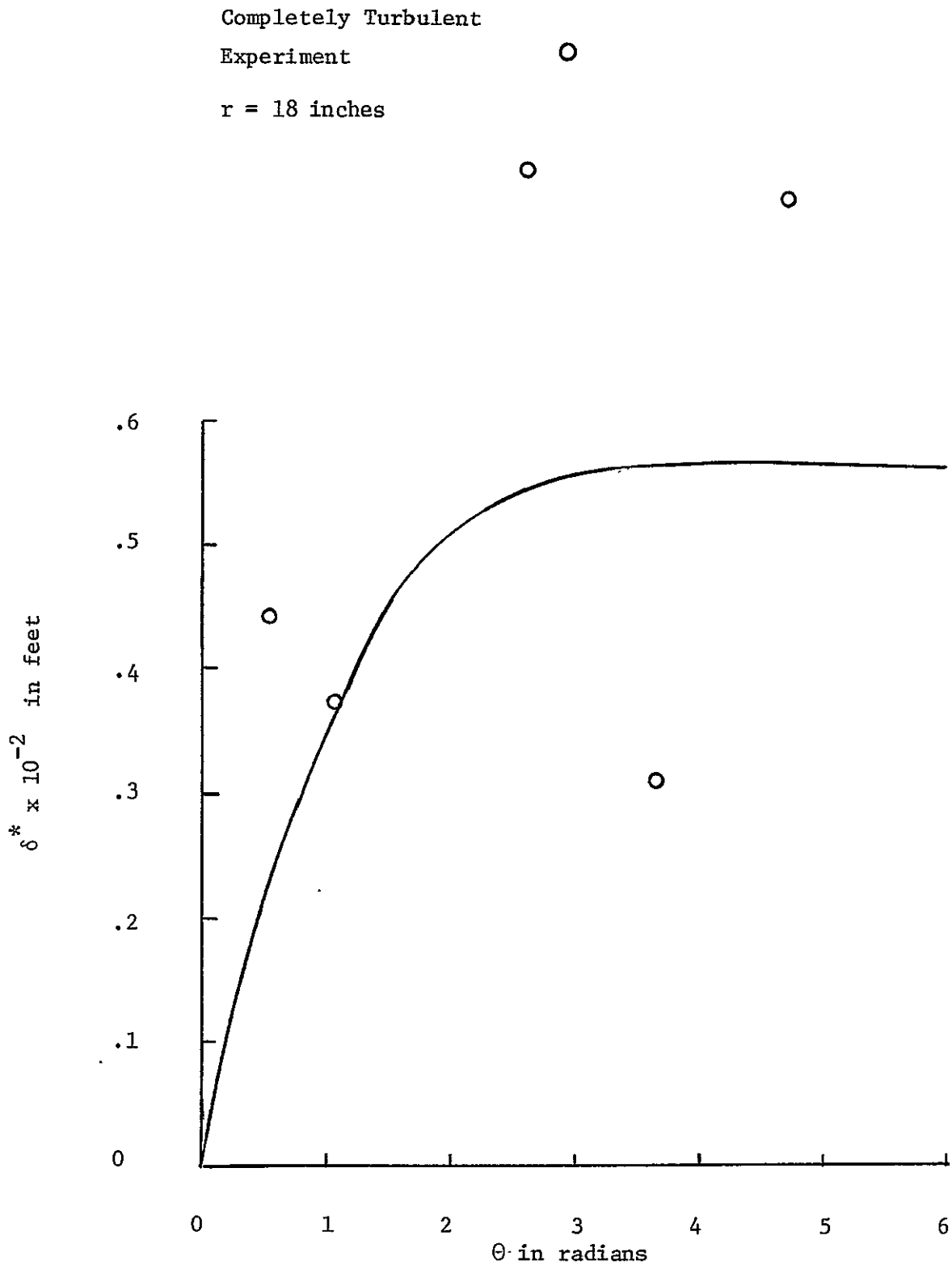

Figure 18-e: Tangential Variations of the Momentum Thickness

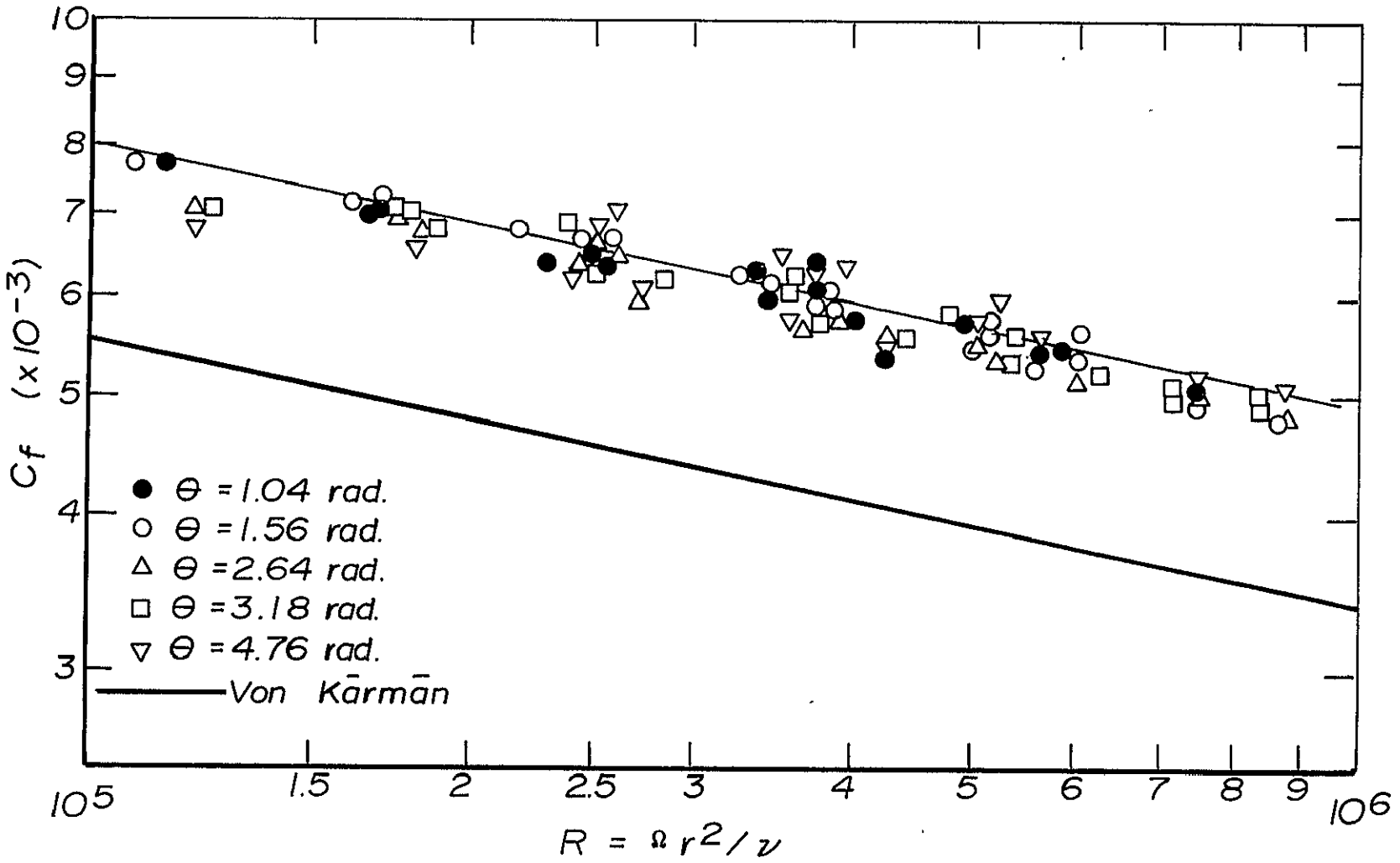

Figure 19: Comparison of the Skin Friction Coefficient of the Blade with that of a Circular Disk

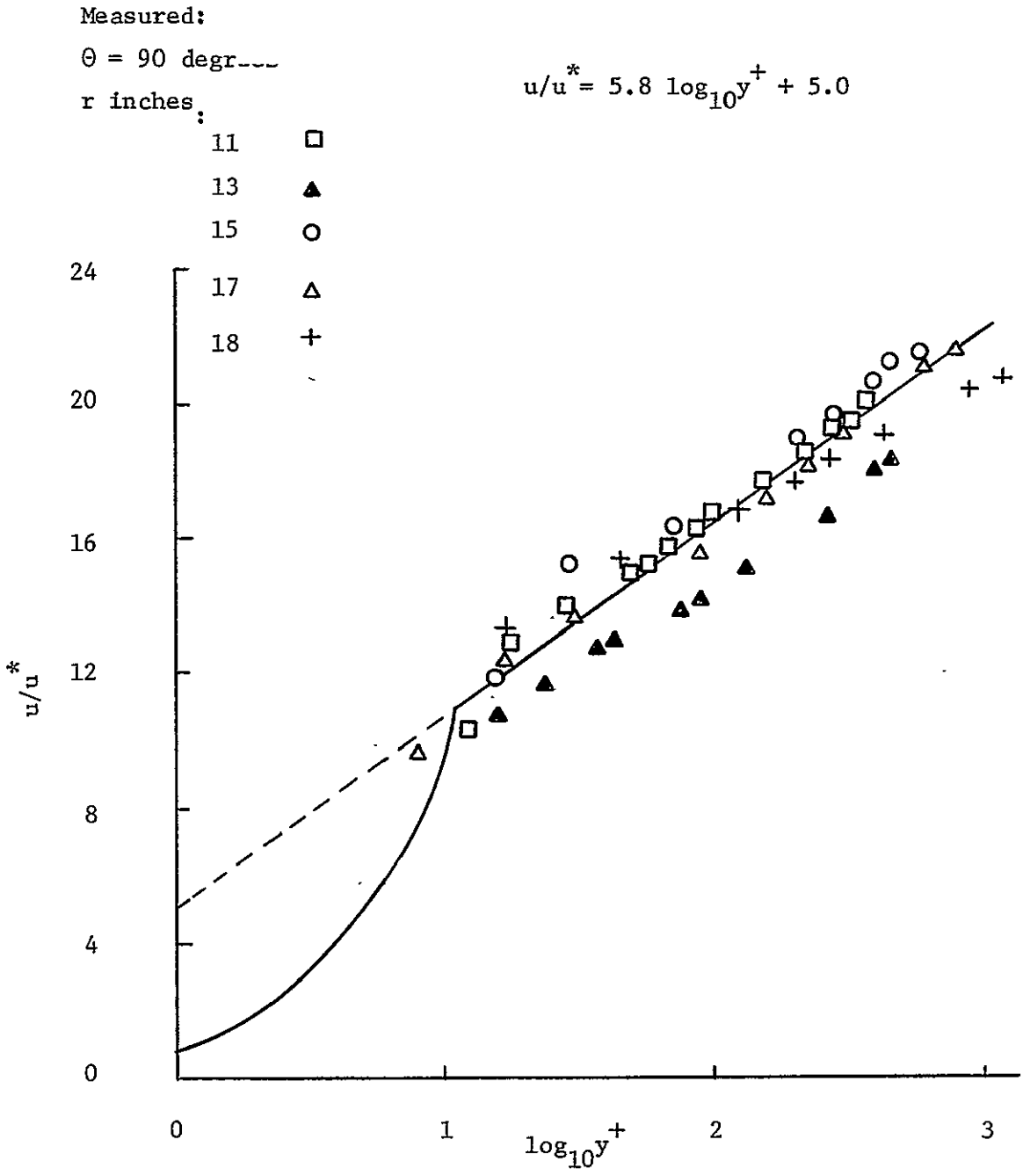

Figure 20-a: Comparison of the Tangential Velocity Profiles with the Law of the Wall

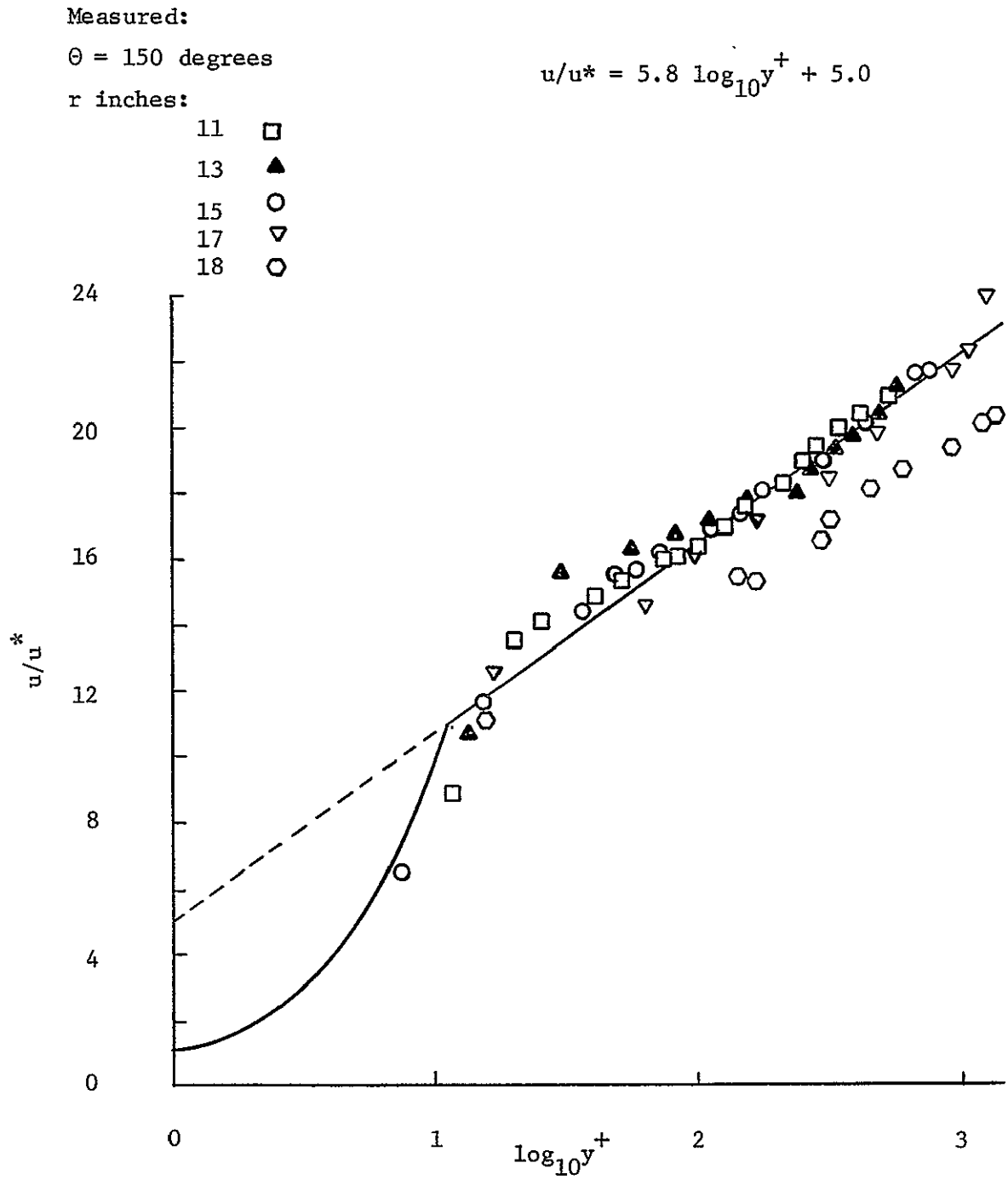

Figure 20-b: Comparison of the Tangential Velocity Profiles with the Law of the Wall

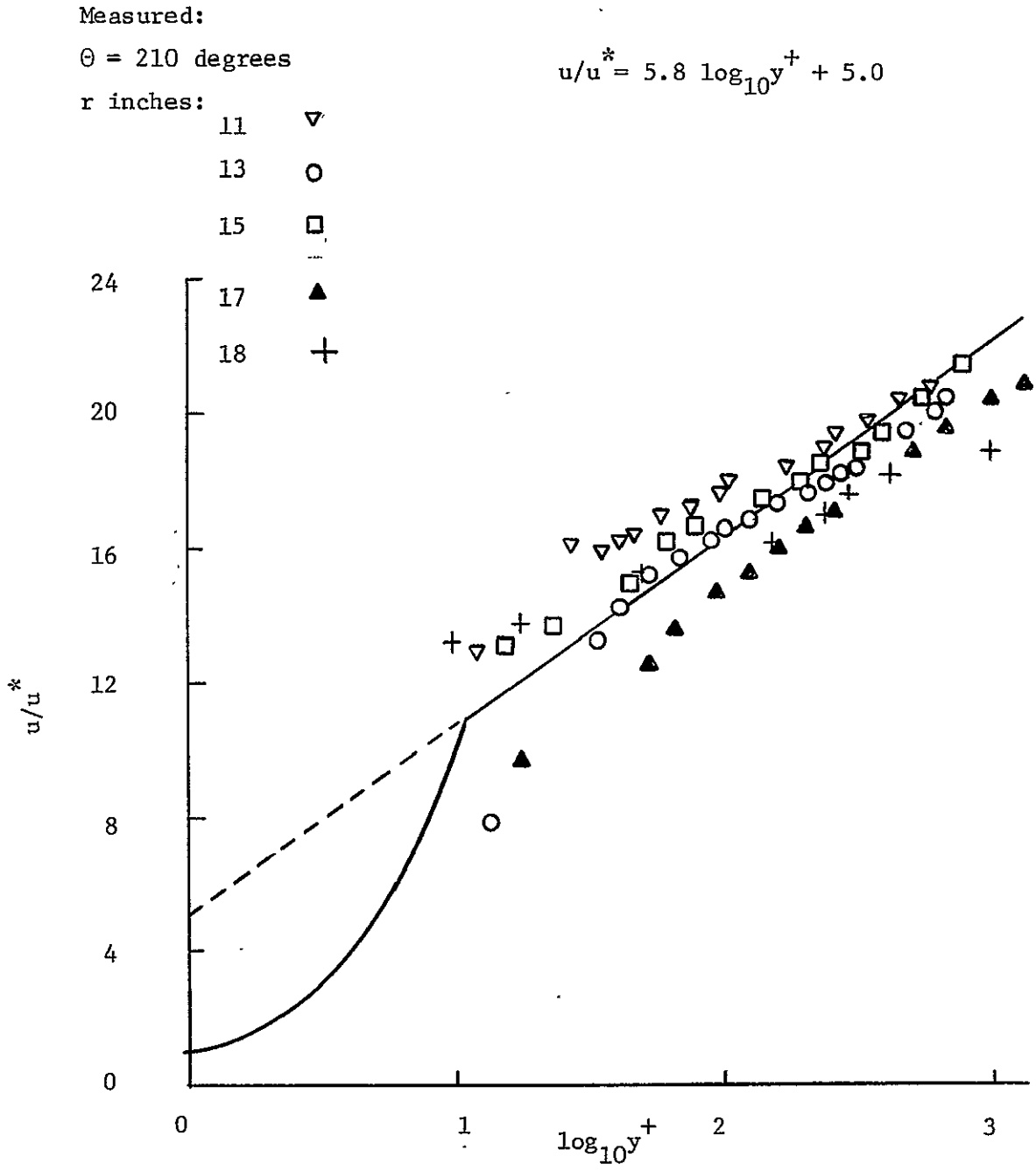

Figure 20-c: Comparison of the Tangential Velocity Profilea with the Law of the Wall

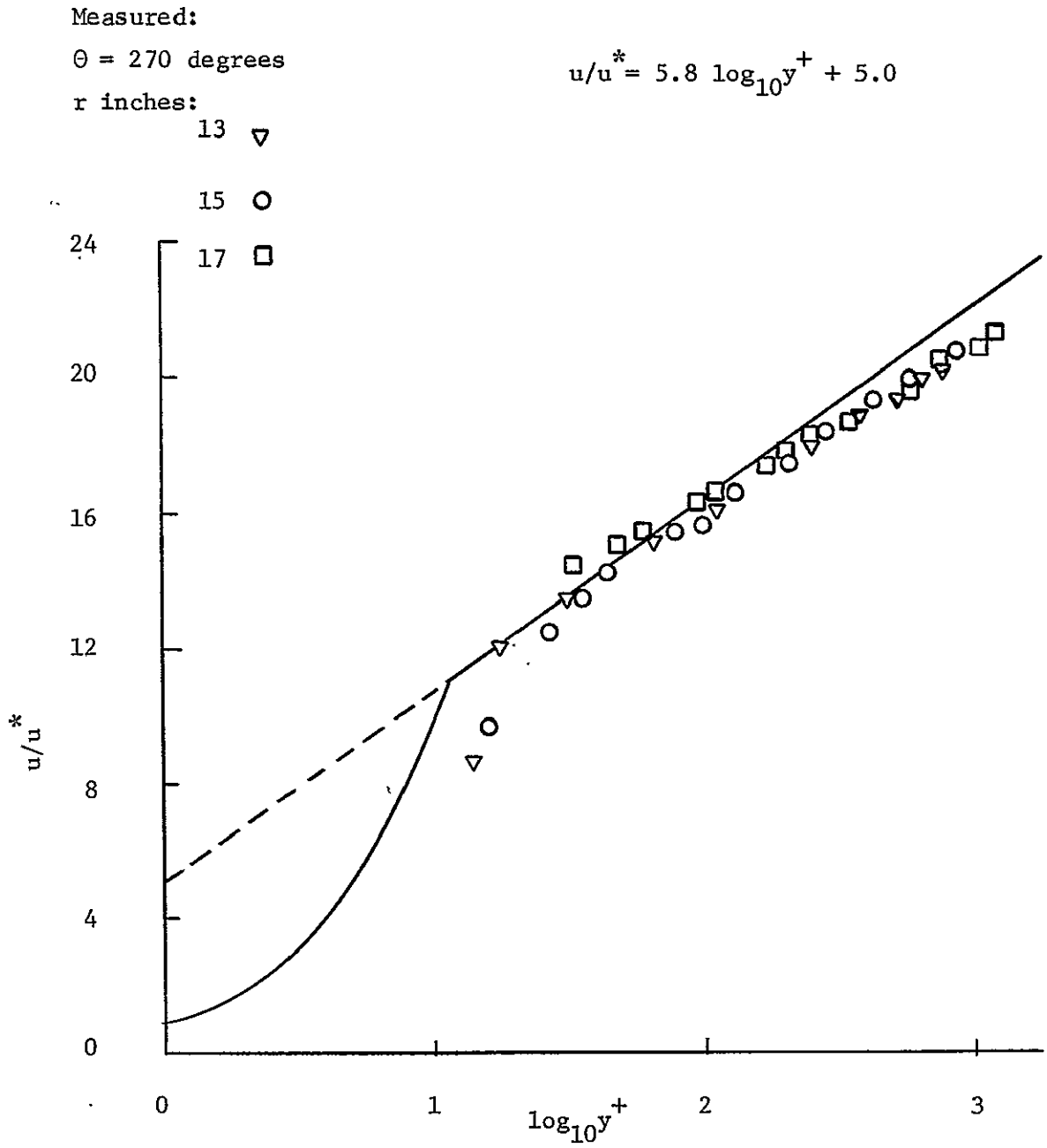

Figure 20-d: Comparison of the Tangential Velocity Profiles with the Law of the Wall

TABLE I

Tangential Velocity Profiles

θ^{o} = 30, r" = 10, T = 64 degrees F°

y (inch)	y/δ	u (ft./sec.)	u/U
0.011	0.088	14.8	0.399
0.020	0.160	27.1	0.730
0.050	0.400	34.4	0.926
0.070	0.056	35.7	0.988
0.090	0.720	36.9	0.995
0.125	1.000	37.1	1.000

θ^{o} = 30, r" = 11, T = 64

y (inch)	y/δ	u (ft./sec.)	u/U
0.011	0.122	12.4	0.299
0.030	0.344	31.6	0.758
0.050	0.555	38.1	0.915
0.090	1.000	41.6	1.000

θ^{o} = 30, r" = 13, T = 64

y (inch)	y/δ	u (ft./sec.)	u/U
0.011	0.134	19.0	0.387
0.025	0.0305	27.7	0.564
0.060	0.733	46.7	0.952
0.080	0.976	49.0	0.977
0.082	1.000	49.2	1.000

θ^{o} = 30, r" = 15, T = 64

y (inch)	y/δ	u (ft./sec.)	u/U
0.012	0.162	24.6	0.432
0.045	0.608	47.5	0.835
0.055	0.743	52.5	0.923
0.065	0.877	56.0	0.984
0.070	0.946	56.6	0.966
0.074	1.000	56.9	1.000

TABLE I (continued)

$\theta = 30$, r = 17, T = 64

y (inch)	y/δ	u (ft./sec.)	u/U
0.11	0.0552	43.4	0.676
0.022	0.110	45.4	0.706
0.075	0.375	55.7	0.867
0.110	0.500	60.5	0.947
0.160	0.800	63.4	0.986
0.200	1.000	64.2	1.000

$\theta = 30$, r = 18, T = 64

y (inch)	y/δ	u (ft./sec.)	u/U
0.011	0.016	45.9	0.660
0.030	0.0435	47.9	0.680
0.070	0.102	52.9	0.750
0.110	0.160	58.3	0.840
0.150	0.218	61.0	0.877
0.200	0.290	64.5	0.928
0.240	0.348	64.6	0.930
0.320	0.464	65/0	0.935
0.410	0.595	65.1	0.938
0.590	0.855	66.9	0.961
0.690	1.000	69.5	1.000

$\theta = 90$, r = 10, T = 64

y (inch)	y/δ	u (ft./sec.)	u/U
0.011	0.0275	16.2	0.433
0.020	0.050	21.2	0.566
0.050	0.125	27.6	0.738
0.100	0.250	30.0	0.802
0.150	0.375	32.2	0.861
0.220	0.550	34.6	0.925
0.270	0.676	36.0	0.962
0.330	0.825	36.8	0.984
0.360	0.900	37.0	0.989
0.400	1.000	37.4	1.000

TABLE I (continued)

$\theta = 90$, r = 11, T = 64

y (inch)	y/δ	u (ft./sec.)	u/U
0.011	0.0339	21.4	0.509
0.045	0.138	31.2	0.742
0.052	0.160	31.7	0.754
0.080	0.246	33.8	0.804
0.140	0.431	36.5	0.869
0.195	0.600	38.4	0.914
0.250	0.770	40.1	0.945
0.300	0.922	40.8	0.971
0.320	0.985	41.1	0.978
0.325	1.000	42.0	1.000

$\theta = 90$, r = 13, T = 64

y (inch)	y/δ	u (ft./sec.)	u/U
0.011	0.0333	29.2	0.592
0.030	0.090	34.6	0.701
0.060	0.183	38.1	0.772
0.100	0.303	41.0	0.831
0.180	0.545	45.0	0.912
0.270	0.816	48.4	0.981
0.320	0.970	49.2	0.997
0.33	1.000	49.3	1.000

$\theta = 90$, r = 15, T = 64

y (inch)	y/	u (ft./sec.)	u/U
0.011	0.025	31.0	0.549
0.020	0.0455	40.2	0.712
0.050	0.1135	43.1	0.764
0.145	0.330	49.4	0.575
0.200	0.455	51.6	0.914
0.280	0.636	54.2	0.960
0.345	0.784	55.7	0.987
0.390	0.886	56.2	0.996
0.440	1.000	56.4	1.000

TABLE I (continued)

$\theta = 90$, r = 17, T = 64

y (inch)	y/δ	u (ft./sec.)	u/U
0.011	0.026	36.6	0.575
0.02	0.0392	40.9	0.643
0.057	0.100	46.1	0.724
0.100	0.192	51.4	0.808
0.200	0.392	56.8	0.893
0.280	0.550	61.6	0.968
0.350	0.686	62.1	0.976
0.380	0.745	62.6	0.984
0.440	0.863	63.3	0.995
0.510	1.000	63.6	1.000

$\theta = 90$, r = 18, T = 64

y (inch)	y/δ	u (ft./sec.)	u/U
0.011	0.0142	37.9	0.644
0.030	0.0387	44.0	0.748
0.080	0.103	48.2	0.819
0.125	0.161	50.8	0.863
0.175	0.226	52.3	0.889
0.275	0.355	54.2	0.921
0.375	0.484	56.6	0.962
0.475	0.614	57.7	0.976
0.575	0.743	58.4	0.993
0.775	1.000	58.8	1.000

$\theta = 150$, r = 11, T = 64

y (inch)	y/δ	u (ft./sec.)	u/U
0.011	0.023	17.7	0.426
0.024	0.050	28.2	0.679
0.120	0.250	34.0	0.819
0.140	0.292	35.1	0.845
0.270	0.457	37.2	0.896
0.240	0.500	37.8	0.910
0.280	0.583	38.8	0.934
0.320	0.666	39.8	0.959
0.400	0.834	40.8	0.983
0.440	0.916	41.1	0.990
0.480	1.000	41.5	1.000

TABLE I (continued)

$\theta = 150$, r = 13, T = 64

y (inch)	y/δ	u (ft./sec.)	u/U
0.011	0.025	25.4	0.516
0.044	0.100	38.4	0.780
0.066	0.150	39.3	0.789
0.088	0.200	40.3	0.819
0.123	0.280	41.2	0.837
0.190	0.432	42.9	0.861
0.210	0.480	44.2	0.898
0.264	0.600	45.6	0.926
0.308	0.700	46.7	0.949
0.385	0.875	48.1	0.977
0.415	0.943	48.7	0.989
0.440	1.000	49.2	1.000

$\theta = 150$, r = 15, T = 64

y (inch)	y/δ	u (ft./sec.)	u/U
0.011	0.0212	30.8	0.541
0.026	0.050	38.1	0.669
0.035	0.0673	41.0	0.720
0.052	0.100	42.6	0.748
0.080	0.154	44.8	0.787
0.120	0.231	47.1	0.827
0.130	0.250	47.2	0.829
0.210	0.406	50.0	0.878
0.310	0.596	53.0	0.931
0.400	0.780	54.9	0.904
0.500	0.962	56.8	0.998
0.520	1.000	56.9	1.000

$\theta = 150$, r = 17, T = 64

y (inch)	y/δ	u (ft./sec.)	u/U
0.011	0.01355	36.2	0.565
0.065	0.080	46.6	0.728
0.111	0.137	49.2	0.768
0.211	0.260	53.2	0.831
0.311	0.383	57.0	0.890
0.411	0.506	59.6	0.931
0.511	0.630	61.6	0.926

TABLE I (continued)

$\theta = 150$, $r = 17$, $T = 64$

y (inch)	y/δ	u (ft./sec.)	u/U
0.611	0.754	63.0	0.993
0.711	0.876	63.6	0.993
0.811	1.000	64.0	1.000

$\theta = 150$, $r = 18$, $T = 64$

y (inch)	y/δ	u (ft./sec.)	u/U
0.011	0.0091	31.6	0.536
0.111	0.917	42.5	0.721
0.182	0.150	47.0	0.797
0.210	0.174	49.0	0.831
0.310	0.256	51.3	0.870
0.410	0.339	53.2	0.903
0.610	0.504	55.2	0.937
0.810	0.670	56.8	0.964
1.010	0.835	57.5	0.976
1.21	1.000	58.9	1.000

$\theta = 210$, $r = 10$, $T = 64$

y (inch)	y/δ	u (ft./sec.)	u/U
0.011	0.022	22.0	0.601
0.030	0.060	25.8	0.704
0.050	0.100	29.0	0.792
0.075	0.150	30.3	0.827
0.090	0.180	31.0	0.846
0.100	0.200	31.1	0.849
0.120	0.240	32.0	0.874
0.150	0.300	32.7	0.893
0.170	0.340	33.3	0.909
0.220	0.440	34.5	0.942
0.300	0.600	35.4	0.967
0.325	0.650	35.6	0.972
0.400	0.800	36.1	0.986
0.500	1.000	36.6	1.000

TABLE I (continued)

Θ = 210, r = 11, T = 64

y (inch)	y/δ	u (ft./sec.)	u/U
0.01	0.026	27.5	0.650
0.025	0.0467	32.7	0.773
0.053	0.100	34.3	0.810
0.091	0.170	35.7	0.843
0.120	0.214	36.5	0.862
0.161	0.300	37.6	0.888
0.188	0.350	37.8	0.983
0.220	0.410	38.7	0.914
0.240	0.450	39.4	0.931
0.240	0.450	39.4	0.931
0.320	0.598	40.0	0.945
0.420	0.785	41.5	0.981
0.520	0.972	42.0	0.992
0.535	1.000	42.3	1.000

Θ = 210, r = 13. T = 64

y (inch)	y/δ	u (ft./sec.)	u/U
0.011	0.020	19.2	0.389
0.021	0.0396	21.6	0.438
0.053	0.100	38.3	0.776
0.100	0.190	41.2	0.835
0.120	0.226	41.9	0.849
0.185	0.350	43.4	0.880
0.205	0.387	43.8	0.888
0.380	0.716	47.1	0.955
0.480	0.905	48.5	0.983
0.530	1.000	49.3	1.000

Θ = 210, r = 15, T = 64

y (inch)	y/δ	u (ft./sec.)	u/U
0.011	0.0202	35.1	0.617
0.071	0.130	45.1	0.794
0.110	0.202	46.2	0.812
0.153	0.280	48.0	0.845

TABLE I (continued)

$\Theta = 210$, r = 15, T = 64

y (inch)	y/δ	u (ft./sec.)	u/U
0.164	0.300	48.3	0.850
0.207	0.380	49.7	0.875
0.246	0.45	50.8	0.894
0.300	0.55	52.6	0.926
0.400	0.735	45.4	0.959
0.540	0.990	56.6	0.996
0.545	1.000	56.8	1.000

$\Theta = 210$, r = 17, T = 64

y (inch)	y/δ	u (ft./sec.)	u/U
0.011	0.0136	30.3	0.469
0.060	0.074	45.3	0.072
0.11	0.136	50.7	0.786
0.121	0.150	51.6	0.789
0.160	0.197	53.0	0.821
0.243	0.300	55.1	0.880
0.310	0.383	58.4	0.905
0.410	0.506	60.5	0.937
0.510	0.630	62.8	0.973
0.610	0.754	63.4	0.982
0.710	0.876	64.0	0.992
0.810	1.000	64.5	1.000

$\Theta = 210$, r = 18, T = 64

y (inch)	y/δ	u (ft./sec.)	u/U
0.011	0.0175	40.6	0.725
0.030	0.0476	44.5	0.796
0.130	0.206	49.3	0.880
0.158	0.250	50.2	0.896
0.230	0.365	52.8	0.942
0.330	0.534	54.4	0.964
0.430	0.682	54.5	0.973
0.630	1.000	56.0	1.000

TABLE I (continued)

$\Theta = 270$, r = 10, T =64

y (inch)	y/δ	u (ft./sec.)	u/U
0.011	0.0319	13.0	0.386
0.030	0.087	23.4	0.696
0.090	0.261	28.2	0.839
0.121	0.530	28.6	0.851
0.150	0.135	30.4	0.904
0.200	0.580	31.7	0.943
0.240	0.695	32.4	0.964
0.300	0.870	33.4	0.994
0.345	1.000	33.6	1.000

$\Theta = 270$, r = 13, T = 64

y (inch)	y/δ	u (ft./sec.)	u/U
0.011	0.018	20.8	0.423
0.025	0.041	32.7	0.665
0.050	0.082	36.2	0.739
0.090	0.1475	38.6	0.786
0.130	0.213	40.8	0.830
0.200	0.328	43.2	0.879
0.214	0.350	43.4	0.883
0.300	0.491	45.5	0.926
0.500	0.820	48.1	0.979
0.600	0.983	49.0	0.997
0.610	1.000	49.1	1.000

$\Theta = 270$, r = 15, T = 64

y (inch)	y/δ	u (ft./sec.)	u/U
0.011	0.0177	26.4	0.463
0.031	0.050	38.7	0.680
0.04	0.0646	40.7	0.715
0.07	0.113	43.0	0.755
0.093	0.150	45.0	0.790
0.11	0.177	46.0	0.808
0.118	0.190	46.6	0.818
0.140	0.226	47.7	0.838

TABLE I (continued)

y (inch)	y/δ	u (ft./sec.)	u/U
0.200	0.323	50.3	0.884
0.248	0.400	51.2	0.899
0.300	0.484	52.8	0.927
0.400	0.646	54.0	0.949
0.500	0.806	55.5	0.975
0.600	0.968	56.5	0.992
0.620	1.000	56.9	1.000

Θ = 270, r = 17, T =64

y (inch)	y/δ	u (ft./sec.)	u/U
0.02	0.0264	44.0	0.688
0.045	0.0591	48.0	0.751
0.07	0.092	50.2	0.785
0.114	0.150	52.2	0.816
0.170	0.224	54.9	0.859
0.270	0.356	57.9	0.906
0.370	0.486	59.4	0.929
0.470	0.617	61.1	0.956
0.570	0.750	62.4	0.976
0.67	0.881	63.0	0.985
0.760	1.000	63.9	1.000

Θ = 270, r = 18, T = 64

y (inch)	y/δ	u (ft./sec.)	u/U
0.02	0.116	40.6	0.678
0.04	0.0233	43.6	0.729
0.07	0.0406	47.0	0.785
0.150	0.0872	50.9	0.851
0.210	0.122	51.3	0.857
0.44	0.256	56.3	0.941
0.580	0.337	55.5	0.928
0.80	0.495	56.4	0.943
0.860	0.500	57.2	0.956
1.29	0.750	59.0	0.986
1.72	1.000	59.8	1.000

TABLE I (continued)

Θ = 290, r = 10, T= 64

y (inch)	y/δ	u (ft./sec.)	u/U
0.011	0.0314	8.55	0.263
0.03	0.0856	17.9	0.550
0.05	0.143	19.9	0.612
0.10	0.286	22.6	0.695
0.125	0.357	27.4	0.843
0.170	0.485	30.1	0.926
0.22	0.727	31.7	0.975
0.30	0.856	32.2	0.990
0.350	1.000	32.5	1.000

Θ = 290, r = 13, T = 64

y (inch)	y/δ	u (ft./sec.)	u/U
0.016	0.02	28.9	0.589
0.05	0.0625	35.0	0.713
0.12	0.15	40.8	0.831
0.23	0.277	43.6	0.888
0.34	0.425	45.4	0.925
0.480	0.600	47.1	0.960
0.580	0.725	47.9	0.976
0.720	0.900	48.5	0.988
0.780	0.975	48.9	0.996
0.80	1.000	49.05	1.000

Θ = 290, r = 15,T 64

y (inch)	y/δ	u (ft./sec.)	u/U
0.08	0.118	41.2	0.716
0.12	0.1765	46.1	0.801
0.20	0.294	50.0	0.869
0.310	0.456	53.0	0.921
0.45	0.661	54.5	0.947
0.530	0.779	56.0	0.973
0.61	0.897	56.7	0.986
0.65	0.955	57.2	0.994
0.68	1.000	57.5	1.000

TABLE I (continued)

$\Theta = 290$, r = 17, T = 64

y (inch)	y/δ	u (ft./sec.)	u/U
0.021	0.021	28.4	0.439
0.08	0.08	49.4	0.763
0.10	0.10	51.4	0.794
0.20	0.20	56.2	0.868
0.31	0.31	59.4	0.918
0.40	0.40	60.9	0.941
0.52	0.52	62.5	0.965
0.62	0.62	63.2	0.976
0.71	0.71	63.9	0.987
0.82	0.82	64.1	0.99
0.90	0.90	64.5	0.996
0.98	0.98	64.6	0.998
1.00	1.00	64.7	1.000

The units of Θ and r are in degrees and inches respectively.

TABLE II

Radial-Flow Velocity Profiles

$\Theta = 210$, $r = 11$, $\varepsilon_o = 0.158$

y	y/δ	u/U	ε_1 (1st. app.)	ε_2 (2nd. app.)	$\varepsilon_2/\varepsilon_o$	w/U
0.02	0.0374	0.74	0.263	0.225	1.42	0.167
0.06	0.112	0.819	0.199	0.194	1.23	0.159
0.10	0.187	0.85	0.158	0.153	0.97	0.130
0.15	0.281	0.88	0.092	0.092	0.58	0.081
0.25	0.467	0.929	0.0875	0.0875	0.55	0.081
0.35	0.655	0.96	0.0697	0.0697	0.44	0.067
0.45	0.84	0.98	0.0068	0.0068	0.054	0.067
0.535	1.00	1.00	0.0	0.0	0.0	0.0

$\Theta = 210$, $r = 13$, $\varepsilon_o = 0.142$

y	y/δ	u/U	ε_1 (1st. app.)	ε_2 (2nd. app.)	$\varepsilon_2/\varepsilon_o$	w/U
0.02	0.0388	0.665	0.383	0.373	2.63	0.248
0.05	0.0944	0.785	0.281	0.277	1.95	0.218
0.10	0.189	0.835	0.23	0.23	1.62	0.192
0.15	0.283	0.86	0.167	0.167	1.18	0.144
0.20	0.378	0.88	0.105	0.105	0.74	0.924
0.30	0.655	0.926	0.0874	0.0874	0.615	0.0801
0.4	0.755	0.960	0.00873	0.00873	0.615	0.0083
0.53	1.00	1.00	0.0	0.0	0.0	0.0

$\Theta = 210$, $r = 15$, $\varepsilon_o = 0.161$

y	y/δ	u/U	ε_1 (1st. app.)	ε_2 (2nd. app.)	$\varepsilon_2/\varepsilon_o$	w/U
0.02	0.0368	0.665	0.262	0.235	1.46	0.158
0.05	0.0915	0.78	0.227	0.217	1.34	0.168
0.10	0.183	0.81	0.185	0.185	1.15	0.15
0.15	0.276	0.85	0.144	0.144	0.89	0.122
0.20	0.368	0.88	0.122	0.122	0.76	0.107
0.3	0.55	0.928	0.0436	0.0436	0.271	0.0405
0.4	0.735	0.96	0.0261	0.0261	0.162	0.025
0.545	1.00	1.00	0.0	0.0	0.0	0.0

TABLE II (continued)

$\Theta = 210$, $r = 17$, $\varepsilon_o = 0.161$

y	y/δ	u/U	ε_1 (1st. app.)	ε_2 (2nd. app.)	$\varepsilon_2/\varepsilon_1$	w/U
0.02	0.0247	0.51	0.354	0.32	1.99	0.163
0.05	0.617	0.69	0.277	0.263	1.63	0.181
0.10	0.124	0.78	0.199	0.190	1.18	0.148
0.2	0.247	0.87	0.136	0.136	0.845	0.119
0.30	0.371	0.90	0.0655	0.0655	0.407	0.059
0.4	0.495	0.94	0.0261	0.0261	0.162	0.0246
0.60	0.74	0.985	0.0174	0.0174	0.108	0.0171
0.81	1.00	1.00	0.0	0.0	0.0	0.0

$\Theta = 150$, $r = 11$, $\varepsilon_o = 0.169$

y	y/δ	u/U	ε_1 (1st. app.)	ε_2 (2nd. app.)	$\varepsilon_2/\varepsilon_o$	w/U
0.02	0.0417	0.650	0.386	0.359	2.12	0.233
0.03	0.063	0.7	0.3	0.291	1.72	0.204
0.06	0.125	0.75	0.218	0.217	1.28	0.168
0.13	0.27	0.834	0.105	0.105	0.62	0.0876
0.20	0.416	0.872	0.083	0.083	0.49	0.0723
0.025	0.0522	0.92	0.074	0.074	0.437	0.0681
0.40	0.835	0.985	0.048	0.048	0.274	0.0473
0.48	1.00	1.00	0.03	0.03	0.177	0.03

$\Theta = 150$, $r = 13$, $\varepsilon_o = 0.169$

y	y/δ	u/U	ε_1 (1st. app.)	ε_2 (2nd. app.)	$\varepsilon_2/\varepsilon_o$	w/U
0.02	0.0455	0.721	0.241	0.235	1.39	0.170
0.05	0.114	0.784	0.217	0.20	1.18	0.157
0.105	0.238	0.83	0.16	0.16	0.945	0.133
0.21	0.48	0.897	0.019	0.019	0.645	0.098
0.28	0.636	0.94	0.048	0.048	0.284	0.045
0.44	1.00	1.00	0.00873	0.00873	0.0515	0.0087

TABLE II (continued)

$\Theta = 150$, r = 15, $\varepsilon_o = 0.169$

y	y/δ	u/U	ε_1 (1st. app.)	ε_2 (2nd. app.)	$\varepsilon_2/\varepsilon_o$	w/U
0.02	0.0385	0.632	0.336	0.3096	1.83	0.195
0.05	0.096	0.745	0.244	0.235	1.39	0.175
0.10	0.192	0.808	0.217	0.217	1.28	0.175
0.15	0.288	0.84	0.145	0.145	0.86	0.122
0.25	0.48	0.90	0.1139	0.1139	0.672	0.1015
0.3	0.576	0.93	0.0927	0.0927	0.547	0.0892
0.35	0.673	0.948	0.0857	0.0857	0.508	0.0811
0.45	0.865	0.98	0.0289	0.0289	0.171	0.0283
0.52	1.00	1.00	-0.0087	-0.0087	-0.051	-0.0087

$\Theta = 150$, r = 17, $\varepsilon_o = 0.179$

y	y/δ	u/U	ε_1 (1st. app.)	ε_2 (2nd. app.)	$\varepsilon_2/\varepsilon_o$	w/U
0.02	0.0246	0.572	0.404	0.354	1.98	0.202
0.04	0.0493	0.68	0.336	0.324	1.81	0.22
0.08	0.0986	0.745	0.286	0.267	1.49	0.111
0.12	0.148	0.779	0.19	0.187	1.04	0.081
0.2	0.247	0.83	0.114	0.114	0.635	0.0946
0.3	0.37	0.885	0.0655	0.0655	0.366	0.056
0.4	0.494	0.922	0.0524	0.0524	0.292	0.0483
0.5	0.616	0.945	0.0436	0.0436	0.244	0.0412
0.6	0.74	0.975	0.0131	0.0131	0.073	0.0128
0.7	0.865	0.99	0.0131	0.0131	0.073	0.013
0.811	1.00	1.00	0.0	0.0	0.0	0.0

$\Theta = 150$, r = 18, $\varepsilon_o = 0.140$

y	y/δ	u/U	ε_1 (1st. app.)	ε_2 (2nd. app.)	$\varepsilon_2/\varepsilon_o$	w/U
0.02	0.0161	0.73	0.34	0.322	2.28	0.235
0.035	0.0289	0.741	0.313	0.272	1.94	0.202
0.1035	0.0855	0.785	0.201	0.20	1.42	0.157
0.2035	0.168	0.83	0.0742	0.0742	0.53	0.0616
0.3035	0.242	0.87	0.0786	0.0786	0.56	0.0684
0.4035	0.333	0.902	0.0436	0.043	0.312	0.0394
0.5035	0.416	0.928	0.0306	0.0306	0.218	0.0283

TABLE II (continued)

$\Theta = 150$, r = 18, $\varepsilon_o = 0.140$

y	y/δ	u/U	ε_1 (1st. app.)	ε_2 (2nd. app.)	$\varepsilon_2/\varepsilon_o$	w/U
0.7035	0.581	0.956	0.0227	0.0227	0.162	0.0217
0.9035	0.746	0.978	0.0393	0.0393	0.0281	-
1.21	1.00	1.00	-.00695	-0.00695	-0.049	-0.0

$\Theta = 30$, r = 10, $\varepsilon_o = 0.176$

y	y/δ	u/U	ε_1 (1st. app.)	ε_2 (2nd. app.)	$\varepsilon_1/\varepsilon_o$	w/U
0.02	0.16	0.73	0.131	-	0.75	0.096
0.05	0.40	0.926	0.0506	-	0.288	0.047
0.1	0.72	0.995	0.0	-	0.0	0.0
0.125	1.00	1.00	0.0	-	0.0	0.0

$\Theta = 150$, r = 13, $\varepsilon_o = 0.367$

y	y/δ	u/U	ε_1 (1st. app.)	ε_2 (2nd. app.)	$\varepsilon_2/\varepsilon_o$	w/U
0.02	0.244	0.51	0.487	0.383	1.04	0.195
0.04	0.488	0.826	0.189	0.181	0.494	0.15
0.06	0.733	0.952	0.158	0.158	0.431	0.15
0.082	1.00	1.00	0.161	0.161	0.44	0.161

The units of Θ and r are in degrees and inches respectively.

TABLE III

Values of δ^*, δ_1, and H

$\Theta = 30^o$

r (inch)	δ^* (inch)	δ_1 (inch)	H
10	0.978×10^{-2}	1.948×10^{-2}	1.991
11	1.023	2.301	2.248
13	1.092	2.362	2.162
15	1.126	2.328	2.069
17	1.810	2.667	1.429
18	5.375	6.802	1.265

$\Theta = 90^o$

r (inch)	δ^* (inch)	δ_1 (inch)	H
10	3.828×10^{-2}	5.590×10^{-2}	1.462
11	3.434	4.797	1.396
13	3.238	4.520	1.398
15	3.613	4.809	1.33
17	4.055	5.501	1.356
18	4.543	5.770	1.272

$\Theta = 150^o$

r (inch)	δ^* (inch)	δ_1 (inch)	H
11	4.380×10^{-2}	6.011×10^{-2}	1.372
13	4.164	5.592	1.342
15	4.836	6.462	1.336
17	6.82	9.075	1.329
18	9.680	12.58	1.298

TABLE III (continued)

$\Theta = 210^{o}$

r (inch)	δ^* (inch)	δ_1 (inch)	H
10	3.45×10^{-2}	4.63×10^{-2}	1.343
11	4.013	5.148	1.282
13	4.62	6.465	1.399
15	4.943	6.430	1.300
17	6.318	8.674	1.372
18	3.727	4.516	1.211

$\Theta = 270$

y (inch)	δ^* (inch)	δ_1 (inch)	H
10	3.09×10^{-2}	4.73×10^{-2}	1.53
13	5.15	7.018	1.361
15	5.23	7.036	1.345
17	5.733	7.554	1.308
18	9.36	11.4	1.21

TABLE IV

Skin Friction and Reynolds Numbers

$\Theta = 60$

r (inch)	RPM	C_f	R_r
11.5	200	7.66×10^{-3}	0.114×10^{6}
11.5	300	7.07	0.171
11.0	400	6.39	0.228
11.5	450	6.36	0.256
11.5	600	5.95	0.342
11.5	700	7.73	0.399
13.9	200	6.97	0.166
13.9	300	6.50	0.249
13.9	400	6.29	0.332
13.9	450	6.10	0.374
13.9	600	5.71	0.499
13.9	700	5.41	0.582
17.0	200	6.97	0.249
17.0	300	6.39	0.373
17.0	450	5.42	0.560
17.0	600	5.05	0.745

$\Theta = 90$

r (inch)	RPM	C_f	R_r
11.2	700	6.09×10^{-3}	0.379×10^{6}
11.2	600	6.28	0.325
11.2	450	6.70	0.244
11.2	400	6.84	0.217
11.2	300	7.16	0.162
11.2	200	7.66	0.108
14.1	700	5.66	0.601
14.1	600	5.76	0.515
14.1	450	5.86	0.386
14.1	400	6.16	0.343
14.1	300	6.70	0.258
14.1	200	7.18	0.171
16.95	700	4.78	0.866
16.95	600	4.91	0.743
16.95	450	5.28	0.557
16.95	400	5.47	0.495
16.95	300	5.90	0.372
16.95	200	6.49	0.248

TABLE IV (continued)

Θ = 150

r (inch)	RPM	C_f	R_r
11.85	200	7.06×10^{-3}	0.121×10^{6}
11.85	300	6.80	0.183
11.85	400	6.36	0.242
11.85	450	5.94	0.273
11.85	600	5.65	0.363
11.85	700	5.58	0.424
14.17	200	6.93	0.176
14.17	300	6.52	0.260
14.17	400	6.02	0.346
14.17	450	5.74	0.390
14.17	600	5.34	0.520
14.17	700	5.14	0.606
17.0	200	6.60	0.249
17.0	300	5.88	0.374
17.0	400	5.50	0.498
17.0	450	5.37	0.560
17.0	600	5.03	0.798
17.0	700	4.81	0.873

Θ = 180

r (inch)	RPM	C_f	R_r
12.05	200	7.05×10^{-3}	0.125×10^{6}
12.05	300	6.79	0.188
12.05	400	6.27	0.250
12.05	450	6.14	0.281
12.05	600	5.75	0.375
12.05	700	5.53	0.438
14.35	200	6.99	0.177
14.35	300	6.43	0.266
14.35	400	6.02	0.355
14.35	450	5.76	0.399
14.35	600	5.36	0.533
14.35	700	5.21	0.621
16.65	200	6.83	0.239
16.65	300	6.29	0.358
16.65	400	5.83	0.477
16.65	450	5.59	0.537
16.65	600	5.10	0.716
16.65	700	4.99	0.836

TABLE IV (continued)

$\Theta = 270$

r (inch)	RPM	C_f	R_r
11.85	200	6.74×10^{-3}	0.121×10^{6}
11.85	300	6.55	0.182
11.85	400	6.14	0.242
11.85	450	6.02	0.273
11.85	600	5.68	0.364
11.85	700	5.50	0.424
14.22	200	7.01	0.174
14.22	300	7.03	0.262
14.22	400	6.51	0.349
14.22	450	6.34	0.393
14.22	600	5.95	0.523
17.05	200	6.80	0.251
17.05	300	6.23	0.376
17.05	400	5.77	0.502
17.05	450	5.60	0.564
17.05	600	5.28	0.752
17.05	700	5.09	0.877